REVISITING CONTROL ESTABLISHMENTS FOR EMERGING ENERGY HUBS

by

VAHIDREZA NASIRIAN

Presented to the Faculty of the Graduate School of

The University of Texas at Arlington in Partial Fulfillment

of the Requirements

for the Degree of

DOCTOR OF PHILOSOPHY

THE UNIVERSITY OF TEXAS AT ARLINGTON

August 2015

To the eternity of those spirits

that lit up the route to

True Freedom

and,

to the most precious gift I ever received, *Zoha*,

who enabled an ultimate happiness era in my life

Acknowledgements

I would like to give my special thank to my graduate advisors, Dr. Ali Davoudi and Dr. Frank L. Lewis, who deeply envisioned this research and generously supported me through all difficult moments. I also would like to thank Dr. Wei Jen Lee, Dr. Dan Popa, and Dr. Rasool Kenarangui for their interest in this research providing their insightful comments that help to the superb quality of this work. I would also specially thank Dr. Rasool Kenarangui, Dr. Jonathan Bredow and Dr. Kambiz Alavi for their friendly patience in mentoring and developing my teaching skills.

I must thank my valuable colleage Seyedali Moayedi for his technical and moral supports during this course of my educations.

I also thank the funding agencies for supporting this research. Particularly, this work was supported in part by the National Science Foundation under grants ECCS-1405173, ECCS-1137354, and ECCS-1128050 and in part by the U.S. Office of Naval Research under grants N00014-14-1-0718 and N00014-13-1-0562 and in part by the UT-Transform program.

June 30, 2015

Abstract

REVISITING CONTROL ESTABLISHMENTS FOR

EMERGING ENERGY HUBS

Vahidreza Nasirian, PhD

The University of Texas at Arlington, 2015

Supervising Professors: Ali Davoudi, Frank L. Lewis

Emerging small-scale energy systems, i.e., microgrids and smartgrids, rely on centralized controllers for voltage regulation, load sharing, and economic dispatch. However, the central controller is a single-point-of-failure in such a design as either the controller or attached communication links failure can render the entire system inoperable. This work seeks for alternative distributed control structures to improve system reliability and help to the scalability of the system. A cooperative distributed controller is proposed that uses a noise-resilient voltage estimator and handles global voltage regulation and load sharing across a DC microgrid. Distributed adaptive droop control is also investigated as an alternative solution. A droop-free distributed control is offered to handle voltage/frequency regulation and load sharing in AC systems. This solution does not require frequency measurement and, thus, features a fast frequency regulation. Distributed economic dispatch is also studied, where a distributed protocol is designed that controls generation units to merge their incremental costs into a consensus and, thus, push the entire system to generate with the minimum cost. Experimental verifications and Hardware-in-the-Loop (HIL) simulations are used to study efficacy of the proposed control protocols.

Table of Contents

List of Illustrations

List of Tables

Chapter 1

Introduction

Active distribution systems are moving toward a distributed structure [1]–[3]. Compared to the centralized generation, distributed generation offers improved efficiency [4], [5], reliability [6]–[9], expandability [10], and stability [11], [12]. Microgrids, as small-scale power systems where generation, consumption, and storage happen in a close physical vicinity, are becoming popular in distribution systems [13]–[15].

DC energy resources, e.g., photovoltaic arrays, storage elements, and fuel cells, are commonly connected to the AC microgrid distribution network via voltage-source inverters [127], [128]. Although inverter-based AC microgrids have been prevalent, DC microgrids are currently emerging at distribution levels. The DC nature of emerging renewable energy sources (e.g., solar) or storage units (e.g., batteries and ultra-capacitors) efficiently lends itself to a DC microgrid paradigm that avoids redundant conversion stages [5], [16]. Many of new loads are electronic DC loads (e.g., in data centers). Even some traditional AC loads, e.g., induction machines, can appear as DC loads when controlled by inverter-fed drive systems [17]. DC microgrids are also shown to have about two orders-of-magnitude more availability compared to their AC counterparts, thus making them ideal candidates for mission-critical applications [7], [18]. Moreover, DC microgrids can overcome some disadvantages of AC systems, e.g., transformer inrush current, frequency synchronization, reactive power flow, power quality issues, etc. [19].

Resembling the control hierarchy of the legacy grid, a hierarchical control structure is conventionally adopted for microgrid operation [70]–[73]. The highest level in the hierarchy (tertiary) is in charge of economical dispatch and coordination with the distribution system operator. It assigns the microgrid voltage to carry out a prescheduled

power exchange between the microgrid and the main grid [74]–[76]. To satisfy the voltage demand of the tertiary control, the secondary control measures voltages across the microgrid and, accordingly, updates the voltage set points for the primary controllers. The primary control, typically implemented locally on individual converters with a droop mechanism handles load sharing among sources.

The secondary and tertiary controls are typically implemented in a centralized fashion [25], [26], which communicates with converters through communication links with high connectivity. Loss of any link in such a topology can lead to the failure of the corresponding unit and, thus, overstressing other units, leading to system-level instability and cascaded failures [27]. Since future extensions add to the complexity of the controller, scalability of central controllers is not straightforward.

Distributed control has emerged as an attractive alternative as it offers improved reliability, simpler communication network, and easier scalability [79]. For example, distributed tertiary control via DC bus signaling is studied in [80], [81]. Structurally, it is desirable to extend the distributed control paradigm to the secondary/primary levels. Categorically, such a controller shall satisfy the two main control objectives of DC microgrids, namely voltage regulation [82] and proportional load sharing [83] or the four objectives of AC microgrids, namely voltage regulation, frequency regulation, and active and reactive load sharing. The proportional load sharing suggests sharing the total load demand among sources in proportion to their power ratings and is commonly practiced to avoid overstressing and aging of the sources [127]–[129].

This research endeavor focuses on developing distributed control alternatives for managing sources and loads in microgrids. Follwoings categorise the research outcomes:

- Chapter 1 introduces a cooperative distributed control policy that handles global voltage regulation and proportional load sharing in DC microgrids. The controller serves as the primary/secondary controller.
- Chapter 2 offers distributed adaptive droop control as an alternative solution for distributed primary/secondary control for DC microgrids. This method adjusts the droop gains in each operating condition to achieve accurate load sharing.
- Chapter 3 focuses on AC microgrids and offers a droop-free distributed control methodology to secure primary/secondary control requirements. It features a novel approach that handles frequency regulation without using any frequency measurement and, thus, provides a faster frequency regulation.
- Chapter 4 focuses on managing loads in DC microgrids. It enhances loads into active loads by adding power buffers. A distributed controller is used to manage transient energy profile of the buffers and, accordingly, shape the transient power demanded from the distribution network.
- Chapter 5 studies the distributed tertiary controller to manage economic dispatch. A distributed protocol is proposed that regulates the incremental costs for all sources across the microgrid and, thus, provides the economic distapch.

The resulting publications are listed below:

Patent

[P1] V. Nasirian, A. Davoudi, and F. L. Lewis, “System and method for distributed control of microgrids,” U.S. provisional patent application serial No. 62/133,974 filed on March 16, 2015, patent pending (UT-Arlington ref. number: 15-17).

Journal Articles

[J1] V. Nasirian, Q. Shafiee, J. M. Guerrero, F. L. Lewis, and A. Davoudi, "Droop-free distributed control for AC microgrids," *IEEE Trans. Power Electron.*, to be published, DOI: 10.1109/TPEL.2015.2414457.

[J2] V. Nasirian, S. Moayedi, A. Davoudi, and F. L. Lewis, "Distributed cooperative control of DC microgrids," *IEEE Trans. Power Electron.*, vol. 30, no. 4, pp. 2288–2303, Apr. 2015.

[J3] V. Nasirian, A. Davoudi, F. L. Lewis, and J. M. Guerrero, "Distributed adaptive droop control for DC distribution systems," *IEEE Trans. Energy Convers.*, vol. 29, no. 4, pp. 944–956, Dec. 2014.

Confrence Papers

[C1] V. Nasirian, H. Modares, F. L. Lewis, and A. Davoudi, "Active loads of a microgrid as players in a differential game," 8th *Int'l Symp. Resilient Control Syst.*, 2015, accepted, Manuscript No: ID-000388.

[C2] V. Nasirian, F. L. Lewis, and A. Davoudi, "Distributed optimal dispatch for DC distribution networks," *IEEE 1st Int'l. Conf. DC Microgrids*, 2015, pp. 97–101 (invited paper).

[C3] V. Nasirian, Q. Shafiee, J. M. Guerrero, F. L. Lewis, and A. Davoudi, "Droop-free team-oriented control for AC distribution systems," in *Proc. 30th IEEE Appl. Power Electron. Conf. Expo.*, 2015, pp. 2911–2918.

[C4] V. Nasirian, A. Davoudi, and F. L. Lewis, "Distributed adaptive droop control for DC microgrids," in *Proc. 29th IEEE Appl. Power Electron. Conf. Expo. (APEC)*, 2014, pp. 1147–1152.

Chapter 2

Distributed Cooperative Control of DC Microgrids

Primary and secondary controls of a microgrid deal with voltage regulation and load sharing across the entire microgrid. Proper load sharing assigns the load among participating converters in proportion to their rated power. This equalizes the per-unit currents of all sources, and prevents circulating currents [32] and overstressing of any source [10], [33]–[35]. The droop control is widely adopted for load sharing by imposing virtual output impedance on each converter [35]–[37]. Static/dynamic performance and stability assessment of droop controllers are investigated in [38]–[42]. Despite simplicity and ease of implementation, the conventional droop method suffers from poor voltage regulation and load sharing, particularly when the line impedances are not negligible [43]–[46]. The primary reason for this poor voltage regulation is the voltage drop caused by the virtual impedance. Another factor is the output voltage mismatch among different converters, which is crucial for the natural power flow in DC systems but further exacerbates the voltage regulation issue.

Possible solutions to the aforementioned issues have been reviewed in [26]. These solutions are either centralized [1] or require establishment of a fully-connected communication network throughout the microgrid, where any two nodes are directly connected [36], [47]–[49]. For example a centralized secondary control in [1] measures the microgrid voltage, calculates a voltage restoration term, and sends the restoration term to all sources. It assumes equal voltages for all converters across the microgrid, which is not a viable assumption for DC microgrids. Adaptive droop control in [50] and [51] further improves performance, but the line impedance is neglected. High droop gains in [26] mitigate power-sharing discrepancy caused by the line impedances. In [52], a communication network is spread all over the microgrid and the functionality of the

centralized secondary controller is embedded in each converter. Point-to-point communication links are required for all sources and any link failure renders the whole microgrid inoperable. The line impedance effect is taken into account in [43], with a fully-connected communication network. Despite improved accuracy, systems with a fully-connected communication network are susceptible to failure as any link failure impairs the whole control functionality. Future extension is another challenge; after any structural/electrical upgrade, some control settings, e.g., the number of sources, need to be updated and embedded in all converters. The voltage regulation requirement is redefined to incorporate the line impedance effect in [43], [53]. Accordingly, it is required that the average voltage across the microgrid (and only not a specific bus voltage) is regulated at the global voltage set point determined by the tertiary control. This is called the *global voltage regulation*, and is considered here.

This chapter focuses on the secondary/primary control of the DC microgrids. The salient features of the proposed distributed cooperative control are:

- Cooperation among converters on a communication graph is used to provide additional correction terms and fine tune the local voltage set point for each converter.
- Each converter is augmented with a voltage regulator. This regulator uses the estimation made by the voltage observer to adjust the local voltage set point and provide global voltage regulation.
- A current regulator is also added that compares the actual per-unit current of a converter with a weighted average of its neighbors' and, accordingly, generates a voltage correction term to provide proportional load sharing.

- Cooperation of the voltage and current regulators is shown to effectively carry out both global voltage regulation and proportional load sharing, particularly, when the line impedances are not negligible.
- A noise-resilient voltage observer is introduced that processes both local and neighbors' voltage approximation to estimate the global average voltage across the microgrid.
- The control scheme does not require a priori knowledge of the global parameters such as the number of sources. Thus, it is scalable and features the plug-and-play capability.
- A sparse communication network is spanned across the microgrid that enables limited message passing among converters; each converter only exchanges data with its neighbors. This is in direct contrast to the centralized control approaches which require communication networks with high-bandwidth communication links and a high level of connectivity.

2.1. Preliminary Review of Graph Theory

Figure 2-1 shows the mapping of a cyber network to a physical microgrid. The nodes represent converters and edges represent communication links for data exchange. The communication graph does not need to have the same topology as the underlying physical microgrid. This cyber connection lays the ground work for the cooperative control paradigm, where neighbors' interactions can lead to a global consensus. Accordingly, not all agents (converters) in a large-scale dynamic system need to be in a direct contact. Instead, each agent only exchanges control variables with its neighbors. Then, using the neighbors' data and its local measurements, the agent updates its control variables.

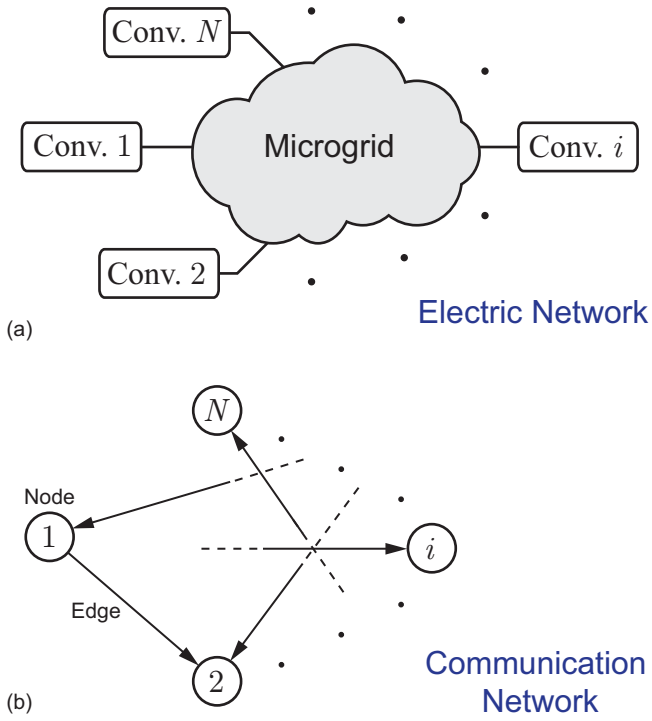

Figure 2-1 General layout of a DC microgrid: (a) converters supplying the grid, (b) communication network spanned among sources for data exchange.

The cooperative control offers global consensus of the desired variables, provided that the communication graph is properly designed.

Figure 2-1(b) shows a directed graph (digraph) associated with the cyber layer connecting the microgrid converters in Fig. 2-1(a). Such a graph is usually represented as a set of nodes $\mathbf{V}_\mathbf{G} = \{v_1^g, v_2^g, ..., v_N^g\}$ connected through a set of edges $\mathbf{E}_\mathbf{G} \subset \mathbf{V}_\mathbf{G} \times \mathbf{V}_\mathbf{G}$, and an associated adjacency matrix $\mathbf{A}_\mathbf{G} = [a_{ij}] \in \mathbb{R}^{N \times N}$. N is the number of nodes. The Adjacency matrix $\mathbf{A}_\mathbf{G}$ contains the communication weights, where $a_{ij} > 0$ if $(v_j^g, v_i^g) \in \mathbf{E}_\mathbf{G}$ and $a_{ij} = 0$, otherwise. a_{ij} is the communication weight for data transfer from node j to

node i. Here, the adjacency matrix is assumed to be time-invariant. $N_i = \{j \mid (v_j^{\mathrm{g}}, v_i^{\mathrm{g}}) \in \mathbf{E}_{\mathbf{G}}\}$ denotes the set of all neighbors of node i, i.e., if $j \in N_i$, then v_i^{g} receives information from v_j^{g}. However, in a digraph, the link is not necessarily reciprocal, i.e., v_j^{g} might not receive information from v_i^{g}. The in-degree matrix $\mathbf{D}_{\mathbf{G}}^{\mathrm{in}} = \mathrm{diag}\{d_i^{\mathrm{in}}\}$ is a diagonal matrix with $d_i^{\mathrm{in}} = \sum_{j \in N_i} a_{ij}$. Similarly, the out-degree matrix is $\mathbf{D}_{\mathbf{G}}^{\mathrm{out}} = \mathrm{diag}\{d_i^{\mathrm{out}}\}$, where $d_i^{\mathrm{out}} = \sum_{i \in N_j} a_{ji}$. The Laplacian matrix is defined as $\mathbf{L} = \mathbf{D}_{\mathbf{G}}^{\mathrm{in}} - \mathbf{A}_{\mathbf{G}}$, whose eigenvalues determine the global dynamics [54]. The Laplacian matrix is balanced if the in-degree of each node matches its out-degree, i.e., $\mathbf{D}_{\mathbf{G}}^{\mathrm{in}} = \mathbf{D}_{\mathbf{G}}^{\mathrm{out}}$. In particular, if the graph is undirected, i.e., all links are bidirectional then, the Laplacian matrix is balanced. A direct path from v_i^{g} to v_j^{g} is a sequence of edges that connects the two nodes. A digraph is said to have a spanning tree if it contains a root node, from which there exists at least a direct path to every other node.

2.2. Cooperative Primary/Secondary Control

Figure 2-2 shows the layout of a typical DC microgrid, where the physical, cyber, and control layers are illustrated. The physical layer consists of the dispatchable sources (including the power electronics converters), transmission lines, and loads. A cyber layer, comprised of all communication links, is spanned among the sources to facilitate data exchange. This is a sparse communication network with at least a spanning tree and is also chosen such that in case of any link failure the remaining network still contains a spanning tree. Although the graph illustrated in Fig. 2-2 is undirected (bidirectional), directed graphs can be used in a general case. Each converter transmits a set of data, $\Psi_i = \left[\overline{v}_i, v_i, i_i^{\mathrm{pu}}\right]$, to its neighbors.

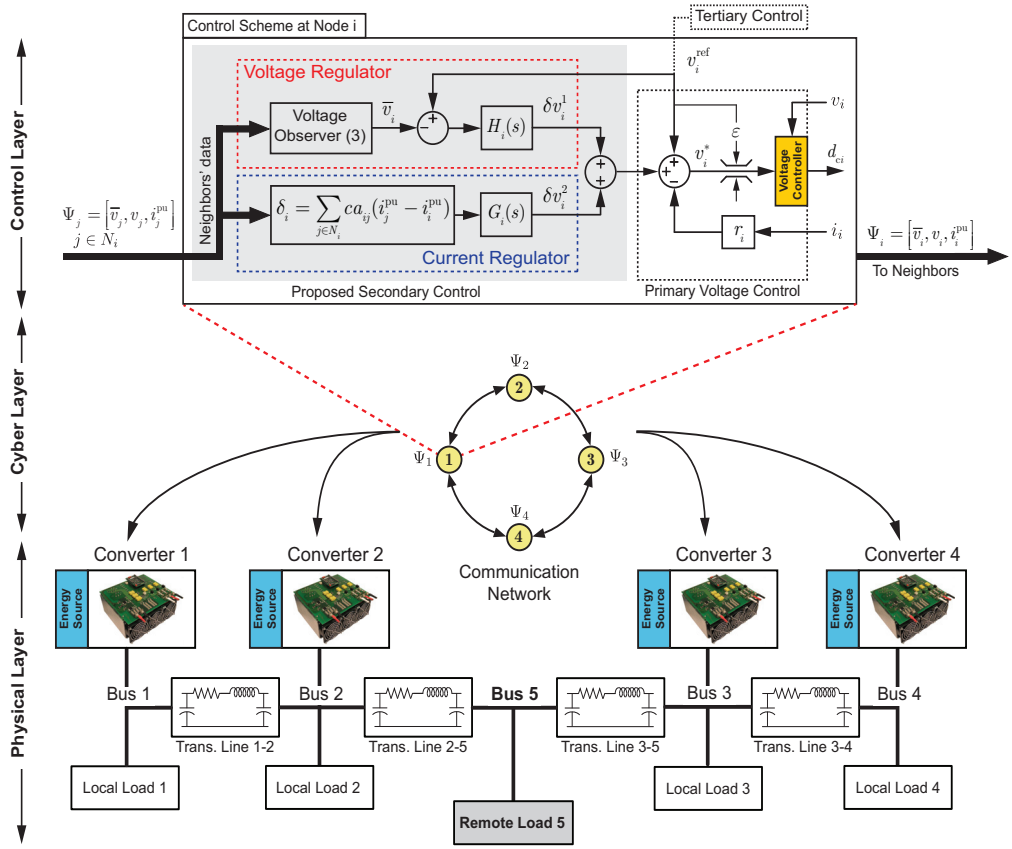

Figure 2-2 Proposed distributed cooperative control for DC microgrids.

The data set transmitted by node i, Ψ_i, consists of three elements; its estimate of the average voltage across the microgrid, $\overline{v}_i$, the measured local voltage, v_i, and the measured per-unit current, i_i^{pu}. The per-unit term here refers to the current provided by the converter divided by its rated current, i.e., $i_i^{\mathrm{pu}} \triangleq i_i / I_i^{\mathrm{rated}}$, where I_i^{rated} is the rated current of the i–th converter. Thus, individual converters may use different values as their base currents (i.e., their rated currents), unlike the conventional per-unit terminology, where converters in the same voltage zone share identical values for base currents. This terminology of the per-unit current is used here to represent loading

percentage of each converter. At the other end of the communication links, each converter j receives data from all its neighbors, Ψ_k, $k \in N_j$, with communication weights, a_{jk}. These communication weights are design parameters and can be considered as data transfer gains.

The global voltage regulation and proportional load sharing are the two objectives of the secondary/primary control, which require proper voltage set point assignment for the individual converters. The proposed secondary controller is highlighted in Fig. 2-2, where local and neighbors' information are processed to adjust the local voltage set point, v_i^*. The starting point is the conventional droop mechanism that characterizes the converter output impedance using a virtual impedance r_i. The droop controller, at a primary control level, acts on local information. When operating conditions vary, the droop mechanism promptly initiates the voltage adjustment. However, this local control has a limited performance. Cooperation among converters, at the secondary control level, can help properly fine-tune the voltage set points, v_i^*, and mitigate the current and voltage residuals.

The voltage set point for the droop control is augmented with two correction terms. These correction terms are provided through cooperation among converters. They are resulted from voltage and current regulators that help fine adjustment of the local voltage set points, i.e., v_i^*s, to provide global voltage regulation and proportional load sharing. Based on Fig. 2-2, the local voltage set point for an individual converter can be expressed as,

$$v_i^* = v_i^{\text{ref}} - r_i i_i + \delta v_i^1 + \delta v_i^2. \tag{2.1}$$

This set point is further adjusted by a voltage limiter (see Fig. 2-2) to maintain the bus voltages within an acceptable range.

The voltage regulator consists of a voltage observer and a PI controller, H_i. The voltage observer at each node estimates the averaged voltage across the microgrid, where $\overline{v_i}$ is the estimation at node i. This estimation is then compared with the global reference voltage, v_i^{ref}, to generate the first voltage correction term, δv_i^1. In case of any mismatch between $\overline{v_i}$ and v_i^{ref}, the controller adjusts δv_i^1 to eliminate the discrepancy. In the islanded mode of operation, the global reference voltage, v_i^{ref}, are typically all equal to the rated voltage of the microgrid. However, in the grid-connected mode, where the microgrid exchanges power with the main grid, the tertiary control sets a new voltage level for the microgrid and relays the new reference value to individual converters. A cooperative observer will process the local voltage measurement and the neighbors' estimates to evaluate the average voltage across the microgrid. Functionality of the observer is discussed in detail in Section 2.3. The line impedances might incapacitate the droop mechanism to proportionally share the load. Herein, a cooperative current regulator generates the second voltage correction term, δv_i^2. The regulator at node i compares the local per-unit current, i_i^{pu}, with a weighted averaged of the neighbors' per-unit currents to find the current mismatch, δ_i,

$$\delta_i = \sum_{j \in N_i} c a_{ij} (i_j^{\text{pu}} - i_i^{\text{pu}}), \tag{2.2}$$

where c is the coupling gain between the voltage and current regulators. The current mismatch, δ_i, is, fed to a PI controller, G_i, which calculates the second voltage correction term, δv_i^2. If the per-unit currents of any two neighbors' differ, the current regulators of the corresponding converters respond and adjust their second voltage correction terms to gain balance.

The current regulator itself (without the droop mechanism shown in Fig. 2-2) can accurately carry out the proportional load sharing. The droop mechanism, however, is typically a part of the primary controller and might be already embedded with the power electronic converter without any deactivation flexibility. Therefore, it is included in the primary controller of Fig. 2-2 to show that the current regulator can handle the load sharing even in the presence of the droop mechanism.

The primary voltage controller typically includes a voltage limiter (see Fig. 2-2). These limiters carry out two tasks: they limit voltage variations at the source terminals and also limit transmission line loading. According to Fig. 2-2, each output voltage is limited to $v_i^{\text{ref}} - \varepsilon \le v_i \le v_i^{\text{ref}} + \varepsilon$. With no loss of generality, one can assume that all converters use identical reference voltages, i.e., $v_i^{\text{ref}} = v_{\text{ref}}$ for all $1 \le i \le N$. Accordingly, voltage difference between every two nodes does not exceed the voltage limit band, i.e., $\left|v_i - v_j\right| \le 2\varepsilon$. Equivalently, the transmission line current will be limited to $i_{ij} \le 2\varepsilon / r_{ij}$, where r_{ij} is the series resistance of the transmission line between nodes i and j.

2.3. Voltage Observer

The observer module is a part of the voltage regulator module, as shown in Fig. 2-2. It uses a dynamic cooperative framework to process neighbors' information and estimate the average voltage across the microgrid.

2.3.1. Dynamic Consensus

Figure 2-3(a) shows the cooperative distributed approach for the global averaging. The observer at node i receives its neighbors' estimates, $\overline{v}_j$ s ($j \in N_i$). Then, the observer updates its own estimate, $\overline{v}_i$, by processing the neighbors' estimates and the local voltage measurement, v_i,

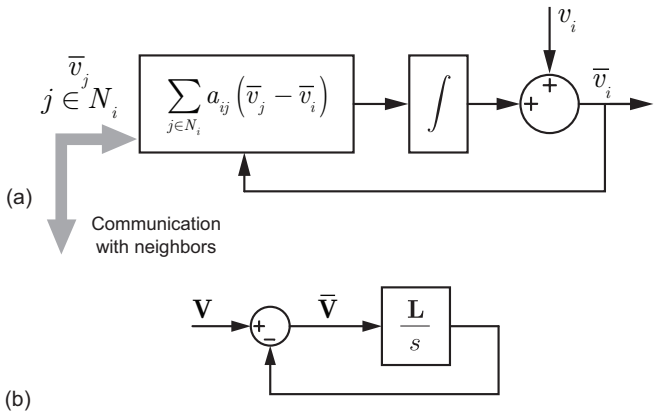

Figure 2-3 Dynamic consensus protocol: (a) averaging policy at each node, (b) global model of the averaging technique in the frequency domain.

Then, the observer updates its own estimate, $\overline{v}_i$, by processing the neighbors' estimates and the local voltage measurement, v_i,

$$\overline{v}_i(t) = v_i(t) + \int_0^t \sum_{j\in N_i} a_{ij}\left(\overline{v}_j(\tau) - \overline{v}_i(\tau)\right)\mathrm{d}\tau. \tag{2.3}$$

This updating protocol is commonly referred to as *dynamic consensus* in literature [55]. As seen in (2.3), the local measurement, e.g., v_i, is directly fed into the estimation protocol. Thus, in case of any voltage variation at node i, the local estimate, $\overline{v}_i$, immediately responds. Then, the change in $\overline{v}_i$ propagates through the communication network and affects all other estimations. By differentiating (2.3),

$$\dot{\overline{v}}_i = \dot{v}_i + \sum_{j\in N_i} a_{ij}\left(\overline{v}_j - \overline{v}_i\right) = \dot{v}_i + \sum_{j\in N_i} a_{ij}\overline{v}_j - d_i^{\text{in}}\overline{v}_i. \tag{2.4}$$

Accordingly, one can formulate the global observer dynamic as,

$$\dot{\overline{\mathbf{v}}} = \dot{\mathbf{v}} + \mathbf{A}_{\mathbf{G}}\overline{\mathbf{v}} - \mathbf{D}_{\mathbf{G}}^{\text{in}}\overline{\mathbf{v}} = \dot{\mathbf{v}} - \left(\mathbf{D}_{\mathbf{G}}^{\text{in}} - \mathbf{A}_{\mathbf{G}}\right)\overline{\mathbf{v}} = \dot{\mathbf{v}} - \mathbf{L}\overline{\mathbf{v}}, \tag{2.5}$$

where $\mathbf{v} = [v_1, v_2, ..., v_N]^{\mathrm{T}}$ is the voltage measurement vector, which carries measured voltage of all nodes. Also, $\overline{\mathbf{v}} = [\overline{v}_1, \overline{v}_2, ..., \overline{v}_N]^{\mathrm{T}}$ denotes the voltage estimation vector, which contains the global average voltage estimated by all nodes. Equivalently, in the frequency domain,

$$\dot{\overline{\mathbf{v}}} = \dot{\mathbf{v}} + \mathbf{A}_{\mathrm{G}}\overline{\mathbf{v}} - \mathbf{D}_{\mathrm{G}}^{\mathrm{in}}\overline{\mathbf{v}} = \dot{\mathbf{v}} - \left(\mathbf{D}_{\mathrm{G}}^{\mathrm{in}} - \mathbf{A}_{\mathrm{G}}\right)\overline{\mathbf{v}} = \dot{\mathbf{v}} - \mathbf{L}\overline{\mathbf{v}}, \tag{2.6}$$

where $\mathbf{V}$ and $\overline{\mathbf{V}}$ are the Laplace transforms of $\mathbf{v}$ and $\overline{\mathbf{v}}$, respectively. Equation (2.3) implies that $\mathbf{v}(0) = \overline{\mathbf{v}}(0)$. Therefore,

$$\overline{\mathbf{V}} = s(s\mathbf{I}_N + \mathbf{L})^{-1}\mathbf{V} = \mathbf{H}_{\mathrm{obs}}\mathbf{V}, \tag{2.7}$$

where $\mathbf{I}_N \in \mathbb{R}^{N\times N}$ and $\mathbf{H}_{\mathrm{obs}}$ are the identity matrix and the observer transfer function, respectively. Equation (2.7) expresses the global dynamics of the voltage observers, whose block diagram is represented in Fig. 2-3(b). It is shown in the Appendix A that if $\mathbf{L}$ is balanced, then all elements of $\overline{\mathbf{v}}$ converge to a consensus value, which is the true average voltage, i.e., the average of all elements in $\mathbf{v}$. In other words,

$$\overline{\mathbf{v}}^{\mathrm{ss}} = \lim_{t\to\infty}\overline{\mathbf{v}}(t) = \mathbf{Q}\times\lim_{t\to\infty}\mathbf{v}(t) = \mathbf{Q}\mathbf{v}^{\mathrm{ss}} = \left\langle \mathbf{v}^{\mathrm{ss}} \right\rangle \underline{\mathbf{1}}, \tag{2.8}$$

where $\mathbf{Q} \in \mathbb{R}^{N\times N}$ is the averaging matrix, whose elements are all equal to $1/N$. $\mathbf{x}^{\mathrm{ss}}$ expresses the steady-state value of the vector $\mathbf{x} \in \mathbb{R}^{N\times 1}$. $\langle \mathbf{x} \rangle$ represents the average of all elements in the vector $\mathbf{x}$. $\underline{\mathbf{1}} \in \mathbb{R}^{N\times 1}$ is a vector whose elements are all equal to one.

2.3.2. Noise Cancellation Module

Disturbances may degrade the efficacy and accuracy of the voltage observers. Non-zero initial value of the integrator in Fig. 2-3(a) or read/write errors in digital storage devices are common disturbance sources in digital processing [56], [57]. For example, a non-zero initial value of any observer's integrator yields to an identical DC error in all estimations.

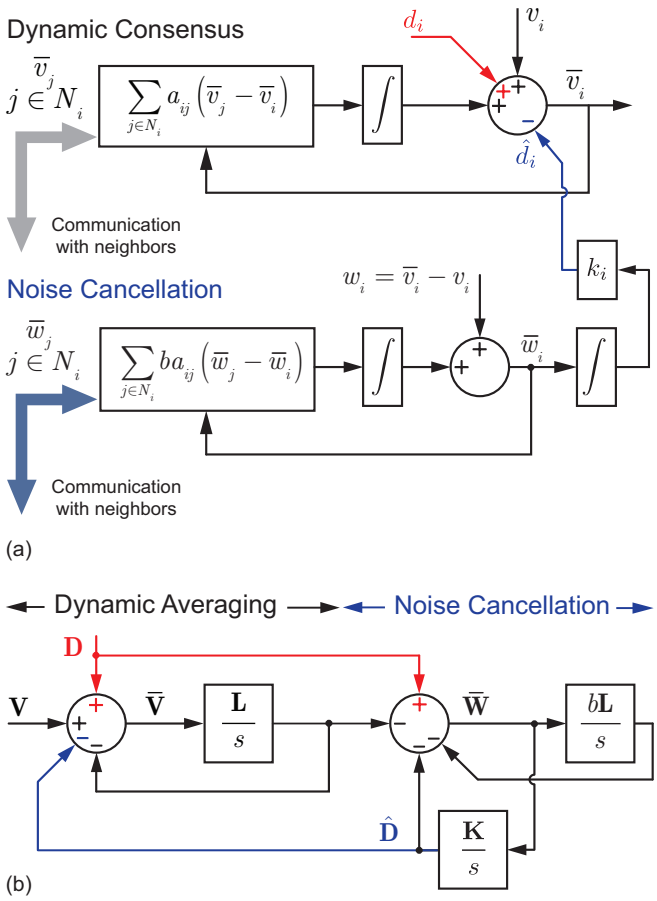

Figure 2-4 Proposed dynamic consensus protocol with noise cancellation: (a) averaging and noise cancellation policies at each node, (b) global model of the averaging technique in the frequency domain.

Therefore, a noise cancellation module is essential to identify and cancel such disturbance/noises. Figure 2-4(a) shows the proposed Noise Cancellation (NC) module incorporated in the voltage observer. A disturbance source, d_i, highlighted in red, is assumed for the observer at node i. This source represents the aggregated effect of all possible disturbance/noises. The primary stage of the NC module is an observer, similar

to that of Fig. 2-3(a), that estimates average of the voltage deviations, w_is, where $w_i = \overline{v}_i - v_i$. This stage is followed by an integrator to ensure disturbance tracking for DC and exponentially damping disturbances, e.g., a non-zero initial value for any integrator.

At each node, the NC module estimates $\langle \mathbf{w} \rangle$ as a noise indicator, where $\mathbf{w} = \left[w_1, w_2, ..., w_N\right]^{\mathrm{T}}$ is the voltage deviation vector. If the noise cancellation term, $\hat{d}_i$, is disabled for all nodes, with no noise corrupting the signals, i.e., $d_i = 0$ for all nodes, the voltage observers converge to the true average voltage. Thus,

$$\mathbf{w} = \overline{\mathbf{v}} - \mathbf{v} \Rightarrow \langle \mathbf{w}^{\mathrm{ss}} \rangle = \langle \overline{\mathbf{v}}^{\mathrm{ss}} \rangle - \langle \mathbf{v}^{\mathrm{ss}} \rangle = \mathbf{0}. \tag{2.9}$$

However, if any noise pollutes any observation, the voltage observations no longer converge to the global average, i.e., $\langle \overline{\mathbf{v}}^{\mathrm{ss}} \rangle \neq \langle \mathbf{v}^{\mathrm{ss}} \rangle$. Accordingly, $\langle \mathbf{w}^{\mathrm{ss}} \rangle \neq \mathbf{0}$. Thus, $\langle \mathbf{w} \rangle$ is a suitable noise indicator. Accordingly, with activated NC module, it estimates $\langle \mathbf{w} \rangle$ and feeds the result into the integrator. If $\langle \mathbf{w} \rangle \neq \mathbf{0}$, the integrator adjusts the noise cancellation term, $\hat{d}_i$, until it matches the noise, i.e., $\hat{d}_i = d_i$, and cancels its effect on the voltage estimations.

Similar to (2.5), the total voltage observer dynamics can be derived by analyzing the policy explained in Fig. 2-4(a). Herein, the total observer is referred to as the observer in Fig. 2-4(a), which incorporates the NC module. According to this figure,

$$\dot{\overline{\mathbf{v}}} = -\mathbf{L}\overline{\mathbf{v}} + \dot{\mathbf{v}} + \dot{\mathbf{d}} - \dot{\hat{\mathbf{d}}}, \tag{2.10}$$

$$\dot{\hat{\mathbf{d}}} = \mathbf{K}\,\overline{\mathbf{w}}, \tag{2.11}$$

$$\dot{\overline{\mathbf{w}}} = -b\mathbf{L}\overline{\mathbf{w}} + \dot{\mathbf{w}} = -b\mathbf{L}\overline{\mathbf{w}} + \dot{\overline{\mathbf{v}}} - \dot{\mathbf{v}}, \tag{2.12}$$

where $\mathbf{d} = \left[d_1, d_2, ..., d_N\right]^{\mathrm{T}}$ and $\hat{\mathbf{d}} = \left[\hat{d}_1, \hat{d}_2, ..., \hat{d}_N\right]^{\mathrm{T}}$ are the actual and estimated disturbance vectors, respectively.

$\overline{\mathbf{w}} = \left[\overline{w}_1, \overline{w}_2, ..., \overline{w}_N\right]^{\mathrm{T}}$ is the estimated voltage deviation vector. $\mathbf{K} = \mathrm{diag}\{k_i\}$ is the NC integrator gain matrix. b is the coupling gain between the main observer and the NC module. Equivalently, in the frequency domain,

$$\left(s\mathbf{I}_N + \mathbf{L}\right)\overline{\mathbf{V}} - \overline{\mathbf{v}}(0) = s\mathbf{V} - \mathbf{v}(0) + s\mathbf{D} - \mathbf{d}(0) - s\hat{\mathbf{D}} + \hat{\mathbf{d}}(0), \tag{2.13}$$

$$s\hat{\mathbf{D}} - \hat{\mathbf{d}}(0) = \mathbf{K}\overline{\mathbf{W}}, \tag{2.14}$$

$$\left(s\mathbf{I}_N + b\mathbf{L}\right)\overline{\mathbf{W}} - \overline{\mathbf{w}}(0) = s\overline{\mathbf{V}} - \overline{\mathbf{v}}(0) - s\mathbf{V} + \mathbf{v}(0), \tag{2.15}$$

where $\mathbf{D}$, $\hat{\mathbf{D}}$, and $\overline{\mathbf{W}}$ are the Laplace transforms of $\mathbf{d}$, $\hat{\mathbf{d}}$, and $\overline{\mathbf{w}}$, respectively. The initial conditions of the vectors involved in the total observer can be determined using Fig. 2-4(a). Accordingly,

$$\hat{\mathbf{d}}(0) = \mathbf{0}, \quad \overline{\mathbf{v}}(0) = \mathbf{v}(0) + \mathbf{d}(0), \tag{2.16}$$

$$\overline{\mathbf{w}}(0) = \overline{\mathbf{v}}(0) - \mathbf{v}(0) = \mathbf{d}(0). \tag{2.17}$$

Each disturbance source, d_i, represents the aggregated effect of all possible disturbances at the corresponding node. Thus, the initial conditions of all the integrators in Fig. 2-4(a) can be safely assumed zero. Based on (2.13)-(2.17), the global block diagram of the total observer is shown in Fig. 2-4(b). One can simplify (2.13)-(2.15) using (2.16)-(2.17),

$$\left(s\mathbf{I}_N + \mathbf{L}\right)\overline{\mathbf{V}} = s\mathbf{V} + s\mathbf{D} - \mathbf{K}\overline{\mathbf{W}}, \tag{2.18}$$

$$\left(s\mathbf{I}_N + b\mathbf{L}\right)\overline{\mathbf{W}} = s(\overline{\mathbf{V}} - \mathbf{V}). \tag{2.19}$$

Therefore,

$$\left(\left(s\mathbf{I}_N + \mathbf{L}\right) + s\mathbf{K}\left(s\mathbf{I}_N + b\mathbf{L}\right)^{-1}\right)\overline{\mathbf{V}} = \left(s\mathbf{I}_N + s\mathbf{K}\left(s\mathbf{I}_N + b\mathbf{L}\right)^{-1}\right)\mathbf{V} + s\mathbf{D}, \tag{2.20}$$

which can be written as,

$$\overline{\mathbf{V}} = \mathbf{H}_{\mathrm{obs}}^{\mathrm{F}}\mathbf{V} + \mathbf{H}_{\mathrm{NC}}\mathbf{D}, \tag{2.21}$$

$$\mathbf{H}_{\text{obs}}^{\text{F}} = \left(\left(s\mathbf{I}_N + \mathbf{L}\right) + s\mathbf{K}\left(s\mathbf{I}_N + b\mathbf{L}\right)^{-1}\right)^{-1} \times \left(s\mathbf{I}_N + s\mathbf{K}\left(s\mathbf{I}_N + b\mathbf{L}\right)^{-1}\right), \tag{2.22}$$

$$\mathbf{H}_{\text{NC}} = s\left(\left(s\mathbf{I}_N + \mathbf{L}\right) + s\mathbf{K}\left(s\mathbf{I}_N + b\mathbf{L}\right)^{-1}\right)^{-1}, \tag{2.23}$$

where $\mathbf{H}_{\text{obs}}^{\text{F}}$ and $\mathbf{H}_{\text{NC}}$ are the total observer and NC transfer functions, respectively. It should be noted that for $\mathbf{K} = \mathbf{0}$, (2.22) and (2.7) provide the same functions. Basically, (2.7) presents the observer transfer function with a disabled NC module, where (2.22) expresses the function with an activated NC module. Appendix B shows that $\lim_{s \to 0} \mathbf{H}_{\text{obs}}^{\text{F}} = \mathbf{Q}$, which guarantees convergence of all estimations to the global average voltage. It should also be noted that $\mathbf{H}_{\text{NC}}$ has a zero at the origin and, thus, for DC and exponentially damping disturbances, the second term in (2.21) decays to zero. Accordingly, the noise cancellation module successfully cancels any DC disturbance and attenuates any other disturbance according to its fundamental frequency. This is a satisfactory performance since most common disturbance sources in digital signal processing, such as non-zero integrator initial condition and read/write errors, have a DC or very-low-frequency nature [57].

2.4. Global Model Development

2.4.1. Global Dynamic Model

Let $\mathbf{v}_{\text{ref}} = [v_1^{\text{ref}}, v_2^{\text{ref}}, \ldots, v_N^{\text{ref}}]^{\text{T}}$ and $\mathbf{i} = [i_1, i_2, \ldots, i_N]^{\text{T}}$ be the global reference voltage and the actual supplied current vectors, respectively. $\mathbf{V}_{\text{ref}}$ and $\mathbf{I}$ are the Laplace transforms of $\mathbf{v}_{\text{ref}}$ and $\mathbf{i}$, respectively. Systematically, $\mathbf{V}_{\text{ref}}$ is the input to the entire microgrid, where $\mathbf{V}$ and $\mathbf{I}$ are the outputs. A global dynamic model formulates the transfer functions from the input, $\mathbf{V}_{\text{ref}}$, to any outputs $\mathbf{V}$ and $\mathbf{I}$.

The cooperative distributed control of Fig. 2-2 introduces two voltage correction terms at each node, δv_i^1 and δv_i^2. Accordingly,

$$\Delta \mathbf{V}^1 = \mathbf{H}\left(\mathbf{V}_{\text{ref}} - \bar{\mathbf{V}}\right), \tag{2.24}$$

$$\Delta \mathbf{V}^2 = -c\mathbf{G}\mathbf{L}\mathbf{I}^{\text{pu}}. \tag{2.25}$$

$\Delta \mathbf{v}^1 = [\delta v_1^1, \delta v_2^1, \ldots, \delta v_N^1]^{\text{T}}$ and $\Delta \mathbf{v}^2 = [\delta v_1^2, \delta v_2^2, \ldots, \delta v_N^2]^{\text{T}}$ are the first and the second voltage correction vectors, respectively. $\Delta \mathbf{V}^1$ and $\Delta \mathbf{V}^2$ are the Laplace transforms of $\Delta \mathbf{v}^1$ and $\Delta \mathbf{v}^2$, respectively. $\mathbf{H} = \text{diag}\{H_i\}$ and $\mathbf{G} = \text{diag}\{G_i\}$ are the voltage and current controller matrices, respectively. $\mathbf{i}^{\text{pu}} = [i_1^{\text{pu}}, i_2^{\text{pu}}, \ldots, i_N^{\text{pu}}]^{\text{T}}$ is the per-unit current vector with the Laplace transform of $\mathbf{I}^{\text{pu}}$. One can write,

$$\mathbf{I}^{\text{pu}} = \mathbf{I}_{\text{rated}}^{-1}\mathbf{I}, \tag{2.26}$$

where $\mathbf{I}_{\text{rated}} = \text{diag}\{I_i^{\text{rated}}\}$ and I_i^{rated} are the current rating matrix and the current rating of the converter at node i, respectively. Thus, by substituting (2.26) in (2.25),

$$\Delta \mathbf{V}^2 = -c\mathbf{G}\mathbf{L}\mathbf{I}_{\text{rated}}^{-1}\mathbf{I}. \tag{2.27}$$

Let $\mathbf{v}^* = [v_1^*, v_2^*, \ldots, v_N^*]^{\text{T}}$ be the vector of local voltage set points with the Laplace transform of $\mathbf{V}^*$. The proposed controller finds the local voltage set points according to,

$$\mathbf{V}^* = \mathbf{V}_{\text{ref}} + \Delta \mathbf{V}^1 + \Delta \mathbf{V}^2 - \mathbf{r}\mathbf{I}, \tag{2.28}$$

where $\mathbf{r} = \text{diag}\{r_i\}$ is the virtual impedance matrix. By substituting (2.24) and (2.27) in (2.28),

$$\mathbf{V}^* = \left(\mathbf{I}_N + \mathbf{H}\right)\mathbf{V}_{\text{ref}} - \mathbf{H}\bar{\mathbf{V}} - \left(c\mathbf{G}\mathbf{L}\mathbf{I}_{\text{rated}}^{-1} + \mathbf{r}\right)\mathbf{I}. \tag{2.29}$$

On the other hand, dynamic behavior of any converter with a closed-loop voltage regulator can be modeled as

$$V_i = G_i^{\text{c}}(s)V_i^*, \tag{2.30}$$

where V_i and V_i^* are the Laplace transforms of v_i and v_i^*, respectively. G_i^c is the closed-loop transfer function of the converter at node i. The closed-loop transfer functions are formulated in [58] and [59] for a wide variety of converters. Global dynamic of the converters can be found as,

$$\mathbf{V} = \mathbf{G}_c \mathbf{V}^*, \tag{2.31}$$

where $\mathbf{G}_c = \mathrm{diag}\{G_i^c\}$ is the transfer-function matrix. Substituting (2.29) in (2.31) yields,

$$\mathbf{V} = \mathbf{G}_c \left((\mathbf{I}_N + \mathbf{H})\mathbf{V}_{\mathrm{ref}} - \mathbf{H}\bar{\mathbf{V}} - \left(c\mathbf{G}\mathbf{L}\mathbf{I}_{\mathrm{rated}}^{-1} + \mathbf{r} \right)\mathbf{I} \right). \tag{2.32}$$

The voltage observer dynamics are formulated in (2.21)-(2.23). By neglecting the disturbance in the observers, one can write $\bar{\mathbf{V}} = \mathbf{H}_{\mathrm{obs}}^{\mathrm{F}} \mathbf{V}$. The microgrid admittance matrix, $\mathbf{Y}_{\mathrm{bus}}$, relates the supplied currents to the bus voltages as,

$$\mathbf{I} = \mathbf{Y}_{\mathrm{bus}} \mathbf{V}. \tag{2.33}$$

The admittance matrix carries all the details of the distribution grid. For example, π-circuit model of any line can be considered by including the line series resistance, series inductance and parallel capacitance in the admittance matrix, $\mathbf{Y}_{\mathrm{bus}}$. Therefore, (2.32) can be written as,

$$\begin{cases} \mathbf{V} = \left(\mathbf{G}_c^{-1} + \mathbf{H}\mathbf{H}_{\mathrm{obs}}^{\mathrm{F}} + \left(c\mathbf{G}\mathbf{L}\mathbf{I}_{\mathrm{rated}}^{-1} + \mathbf{r} \right)\mathbf{Y}_{\mathrm{bus}} \right)^{-1} (\mathbf{I}_N + \mathbf{H})\mathbf{V}_{\mathrm{ref}} \\ \mathbf{I} = \left(\left(\mathbf{Y}_{\mathrm{bus}}\mathbf{G}_c \right)^{-1} + \mathbf{H}\mathbf{H}_{\mathrm{obs}}^{\mathrm{F}}\mathbf{Y}_{\mathrm{bus}}^{-1} + c\mathbf{G}\mathbf{L}\mathbf{I}_{\mathrm{rated}}^{-1} + \mathbf{r} \right)^{-1} (\mathbf{I}_N + \mathbf{H})\mathbf{V}_{\mathrm{ref}} \end{cases}. \tag{2.34}$$

Equation (2.34) represents the global microgrid dynamics with the proposed controller in effect.

2.4.2. Controller Design Guidelines

For a given microgrid, the matrix of converters' closed-loop transfer functions, $\mathbf{G}_c$, the current rating matrix, $\mathbf{I}_{\mathrm{rated}}$, and the admittance matrix, $\mathbf{Y}_{\mathrm{bus}}$, are known. The communication graph needs to contain at least a spanning tree. Weights of the

communication links, a_{ij}, and, thus, the Laplacian matrix, $\mathbf{L}$, may, then, be chosen to provide the desired dynamic for the voltage observers by evaluating (2.7). It should be noted that the selection of the communication weights must satisfy a balanced Laplacian matrix. Equation (2.23) helps to design the coupling gain, b, and the integrator gain matrix, $\mathbf{K}$, to achieve a satisfactory noise cancellation dynamic. Given the Laplacian matrix, $\mathbf{L}$, and the total observer transfer function, $\mathbf{H}_{\text{obs}}^{\text{F}}$ (or the reduced-order function $\mathbf{H}_{\text{obs}}$), one can use (2.34) to design the voltage and current controller matrices ($\mathbf{H}$ and $\mathbf{G}$, respectively), the virtual impedance matrix, $\mathbf{r}$, and the coupling gain, c, to provide any desired asymptotically stable dynamic response, where all poles of (2.34) lie in the Open Left Hand Plane (OLHP). The current regulator surpasses the droop mechanism in providing the proportional load sharing and, thus, the virtual impedance matrix, $\mathbf{r}$, can be freely designed. However, the designer may still use the traditional approach to tune the virtual impedances as,

$$\mathbf{r} = m\mathbf{I}_{\text{rated}}^{-1}, \tag{2.35}$$

where m is a positive scalar design parameter.

2.4.3. Steady-state Analysis

Steady-state analysis is essential to ensure that the proposed controller satisfies both operational requirements; the global voltage regulation and the proportional load sharing. With no loss of generality, one can assume,

$$\mathbf{V}_{\text{ref}} = \frac{v_{\text{ref}}}{s}\underline{\mathbf{1}}, \tag{2.36}$$

where v_{ref} is the reference voltage for the entire microgrid. voltage stabilization, throughout the microgrid, is also assumed. Accordingly, the voltage vector, $\mathbf{V}$, is a type 1 vector, i.e., it has a single pole at the origin and all other poles lie in the OLHP. Thus, one may safely use the final value theorem to find the steady-state voltage vector, $\mathbf{v}^{\text{ss}}$,

$$\begin{aligned}\mathbf{v}^{\text{ss}} &= \lim_{t\to\infty}\mathbf{v}(t) = \lim_{s\to 0} s\mathbf{V}(s)\\ &= \lim_{s\to 0}\left(s\mathbf{G}_{\text{c}}^{-1} + s\mathbf{H}\mathbf{H}_{\text{obs}}^{\text{F}} + s\left(c\mathbf{G}\mathbf{L}\mathbf{I}_{\text{rated}}^{-1} + \mathbf{r}\right)\mathbf{Y}_{\text{bus}}\right)^{-1} \times s v_{\text{ref}}(\mathbf{I}_N + \mathbf{H})\underline{\mathbf{1}}.\end{aligned} \tag{2.37}$$

The voltage and current controllers (H_is and G_is, respectively) are PI controllers and, thus, one can write $\mathbf{H} = \mathbf{H}_{\text{P}} + \mathbf{H}_{\text{I}}/s$, where $\mathbf{H}_{\text{P}}$ and $\mathbf{H}_{\text{I}}$ are diagonal matrices carrying proportional and integral gains of the voltage controllers. Similarly, $\mathbf{G} = \mathbf{G}_{\text{P}} + \mathbf{G}_{\text{I}}/s$, where $\mathbf{G}_{\text{P}}$ and $\mathbf{G}_{\text{I}}$ are diagonal matrices that contain proportional and integral gains of the current controllers. It is also known that the DC gain of the closed-loop converters are equal to one, i.e., $\mathbf{G}_{\text{c}}(0) = \mathbf{I}_N = \mathbf{G}_{\text{c}}^{-1}(0)$ [58]. In addition, based on Theorem B.1 (see Appendix B), $\lim_{s\to 0}\mathbf{H}_{\text{obs}}^{\text{F}} = \mathbf{Q}$. Thus, (2.37) can be written as,

$$\mathbf{v}^{\text{ss}} = v_{\text{ref}}\left(\mathbf{H}_{\text{I}}\mathbf{Q} + c\mathbf{G}_{\text{I}}\mathbf{L}\mathbf{I}_{\text{rated}}^{-1}\mathbf{Y}_{\text{dc}}\right)^{-1}\mathbf{H}_{\text{I}}\underline{\mathbf{1}}, \tag{2.38}$$

or, equivalently,

$$\left(\mathbf{U}\mathbf{Q} + c\mathbf{L}\mathbf{I}_{\text{rated}}^{-1}\mathbf{Y}_{\text{dc}}\right)\mathbf{v}^{\text{ss}} = v_{\text{ref}}\mathbf{U}\underline{\mathbf{1}}, \tag{2.39}$$

where $\mathbf{Y}_{\text{dc}} = \mathbf{Y}_{\text{bus}}(0)$ is the DC admittance matrix and $\mathbf{U} = \mathbf{G}_{\text{I}}^{-1}\mathbf{H}_{\text{I}} = \text{diag}\{u_i\}$ is a diagonal matrix with $u_i = \mathbf{H}_{\text{I}}(i,i)/\mathbf{G}_{\text{I}}(i,i)$. All the integrator gains for the current controllers are assumed to be positive and, thus, $\mathbf{G}_{\text{I}}^{-1}$ exists. Since the Laplacian matrix is designed to be balanced (see Subsection 2.4.2), one can write $\mathbf{Q}\mathbf{L} = \mathbf{0}$. Therefore, by multiplying both sides of (2.39) by the averaging matrix, $\mathbf{Q}$,

$$\mathbf{Q}\left(\mathbf{U}\left(\mathbf{Q}\mathbf{v}^{\text{ss}}\right)\right) = v_{\text{ref}}\mathbf{Q}\left(\mathbf{U}\underline{\mathbf{1}}\right). \tag{2.40}$$

Based on the definition of the averaging matrix, $\mathbf{Q}$, $\mathbf{Q}\mathbf{x} = \langle\mathbf{x}\rangle\underline{\mathbf{1}}$, for any vector $\mathbf{x} \in \mathbb{R}^{N\times 1}$. Accordingly, (2.40) is equivalent to,

$$\langle\mathbf{v}^{\text{ss}}\rangle\langle\mathbf{U}\underline{\mathbf{1}}\rangle\underline{\mathbf{1}} = v_{\text{ref}}\langle\mathbf{U}\underline{\mathbf{1}}\rangle\underline{\mathbf{1}}, \tag{2.41}$$

or, equivalently, $\left\langle \mathbf{v}^{ss} \right\rangle = v_{ref}$. This analysis shows that the proposed controller provides global voltage regulation, i.e., it successfully regulates the average voltage at the desired value. On the other hand, (2.39) can be written as,

$$\mathbf{U}\left(\mathbf{Q}\mathbf{v}^{ss}\right) + c\mathbf{L}\mathbf{I}_{rated}^{-1}\mathbf{i}^{ss} = v_{ref}\mathbf{U}\underline{\mathbf{1}}, \tag{2.42}$$

or, equivalently,

$$\mathbf{L}\left(\mathbf{I}_{rated}^{-1}\mathbf{i}^{ss}\right) = c^{-1}\left(v_{ref} - \left\langle \mathbf{v}^{ss} \right\rangle\right)\mathbf{U}\underline{\mathbf{1}} = \mathbf{0}. \tag{2.43}$$

The Lemma A.1 (see Appendix A) ensures that the Laplacian matrix $\mathbf{L}$ has a simple eigenvalue at the origin, i.e., $\lambda_1 = 0$. Thus, based on (2.43), $\mathbf{I}_{rated}^{-1}\mathbf{i}^{ss}$ is the right eigenvector of $\mathbf{L}$ associated with $\lambda_1 = 0$. It is mentioned in the Proof of Lemma A.2 (see Appendix A) that $w_r = \underline{\mathbf{1}}$ is the right eigenvector of the Laplacian matrix, $\mathbf{L}$, associated with $\lambda_1 = 0$. Thus,

$$\mathbf{I}_{rated}^{-1}\mathbf{i}^{ss} = n\underline{\mathbf{1}}, \tag{2.44}$$

where n is a positive scalar. Equation (2.44) concludes the proportional load sharing. Equations (2.41) and (2.44) show that the proposed controller successfully carries out both global voltage regulation and proportional load sharing.

2.5. Case Study

A low-voltage DC microgrid, with a structure shown in Fig. 2-2, is prototyped to study the proposed control methodology. Figure 2-5 shows the experimental setup. Four adjustable isolated AC sources are used as the energy sources. Each source is driven by a buck converter augmented with an input rectifier.

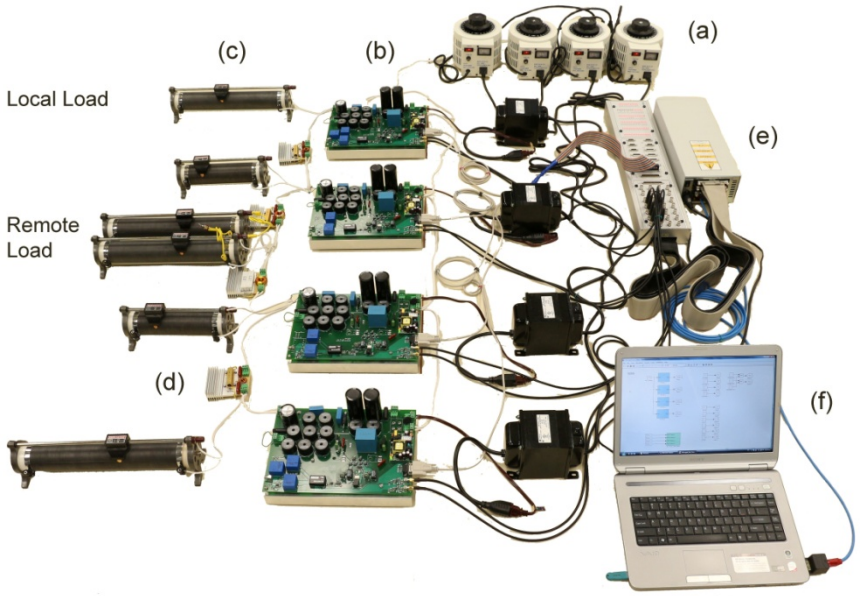

Figure 2-5 DC microgrid Prototype: (a) input AC sources, (b) buck converters driving each source, (c) local and remote loads, (d) transmission lines, (e) dSAPCE controller board (DS1103), (f) programming and monitoring PC.

The converters have similar topologies but different ratings, i.e., the rated currents of the first and the fourth converters are twice those for the other two converters. A π - circuit model is used for each transmission line. There are four local and one remote loads, as seen in Fig. 2-2.

Alternative graphical connections are shown in Fig. 2-6. Communication links are assumed bidirectional to feature a balanced Laplacian matrix and help with the sparsity of the resulting communication graph. Although all alternative graphs include spanning trees, some are susceptible to lose connectivity in the case of a single link failure. For example, if any of the links highlighted in red in Figs. 2-6(a) or 2-6(b) is lost, the corresponding graph losses its connectivity, which hinders the functionality of the control mechanism.

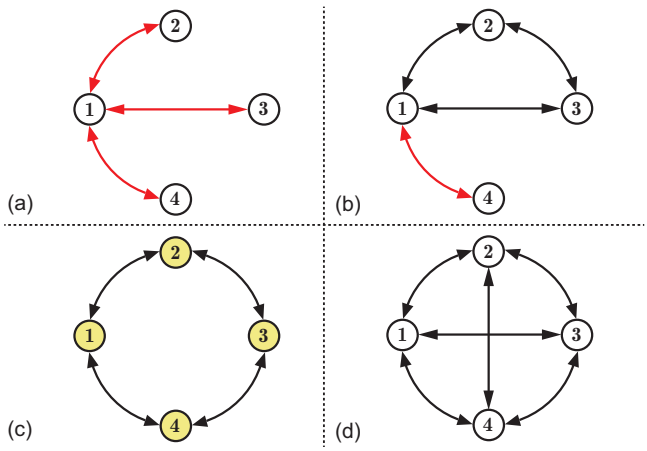

Figure 2-6 Alternative connections forming a connected graph with: (a) no redundant link, (b) suboptimal link redundancy, (c) optimal link redundancy, (d) full connection.

However, for the set of four agents, the circular communication flow in Fig. 2-6(c) is the sparsest network where the failure of a single link does not compromise the graphical connectivity. Figure 2-6(d) is a fully connected graph, but it lacks sparsity. Therefore, the graphical structure in Fig. 2-6(c) is chosen for data exchange in the cyber layer.

A dSPACE control board (DS1103) implements the control routines. Electrical parameters of the microgrid are provided in the Appendix C. Although different voltage levels are possible [60], [61], a $48\ \mathrm{V}$ system is considered here. The typical acceptable voltage deviation is about 5% of the rated voltage [36] and, thus, the voltage limiters are set accordingly with $\varepsilon = 2.5\ \mathrm{V}$.

2.5.1. Design Procedure

Prior knowledge of converters' frequency response is essential to the design procedure in Subsection 2.4.2. Dynamic modeling of power electronics converters for microgrid applications is discussed in detail in the literature [62]. Analytical approaches do not consider practical limitations such as constraints on the duty cycles of switching

converters. Alternatively, the transfer functions of the underlying converters are extracted experimentally using perturbation injection and frequency sweep techniques. For a wide range of loading conditions and input voltages, the reference point of each converter is augmented with a sinusoidal signal with an adjustable frequency. For any given frequency point, the sinusoidal content of the converter's output voltage is then compared with the injected sinusoidal signal to extract the converter's frequency response for that given frequency. This procedure is repeated for the frequency range of interest. Output impedances are chosen in the study to cover light load ($R = 24\ \Omega$) to full load ($R = 12\ \Omega$) conditions. Measured transfer functions are shown in Fig. 2-7. Accordingly, the converter's transfer function can be formulated as a second-order function,

$$G_i^c = \frac{|p_1||p_2|}{(s - p_1)(s - p_2)}, \tag{2.45}$$

where p_1 and p_2 ($|p_2| > |p_1|$) can be found by curve-fitting techniques. Fitted frequency response is highlighted in red in Fig. 2-7, where an good agreement is reported between the empirical and fitted data. The transfer function in (2.45) is further used in the design procedure.

Following the guideline in Subsection 2.4.2, knowledge of the microgrid admittance matrix is also required. The underlying microgrid is a five-bus system (see Fig. 2-2) and has a five-by-five admittance matrix. However, the admittance matrix, $\mathbf{Y}_{\text{bus}}$, in (2.33) only represents the interaction between the voltages and currents of the generating buses and, thus, is a four-by-four matrix. This matrix can be found by reducing the original five-by-five admittance matrix though the Kron's reduction technique.

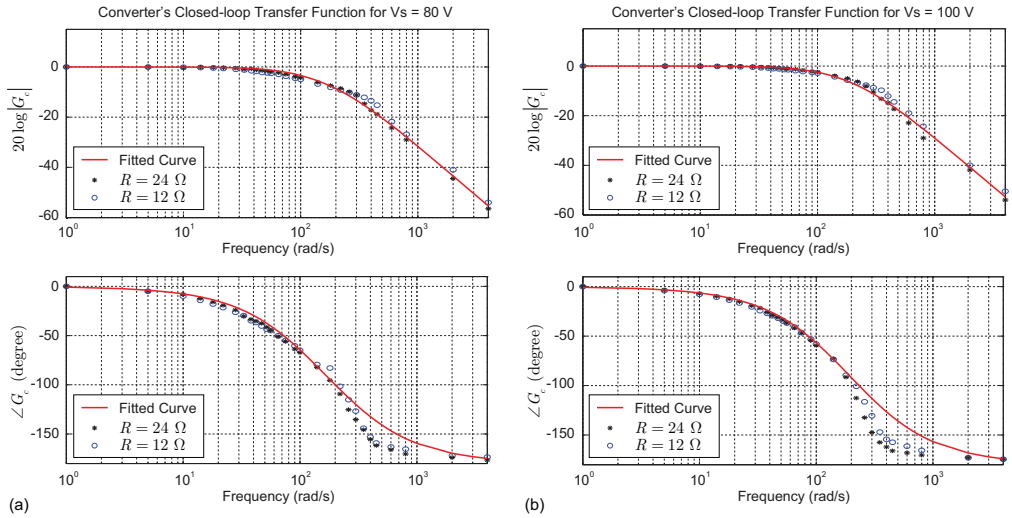

Figure 2-7 Measured frequency response of the buck converters for various operating conditions: a) $V_{\mathrm{s}} = 80\ \mathrm{V}$, b) $V_{\mathrm{s}} = 100\ \mathrm{V}$.

Design of the communication weights, a_{ij} s, which are stored in the adjacency matrix, $\mathbf{A}_{\mathrm{G}}$, (or, equivalently, the Laplacian matrix, $\mathbf{L}$) is tightly linked to the voltage observers' dynamic in (2.7). The weights can be designed to adjust the convergence speed of the estimated voltages. Proper functioning of the voltage regulator in Fig. 2-2 requires a fast estimation of the global average voltage, particularly, faster than the converters' dynamic. Here, it is desired that the eigenvalues of the adjacency matrix (or, equivalently, poles of $\mathbf{H}_{\mathrm{obs}}$) provide a dynamic estimation response at least twice as fast as that of the converters'. A scaling factor, a, is defined to scale the adjacency matrix as,

$$\mathbf{A}_{\mathrm{G}} = a \times \begin{bmatrix} 0 & 90 & 0 & 110 \\ 90 & 0 & 100 & 0 \\ 0 & 100 & 0 & 120 \\ 110 & 0 & 120 & 0 \end{bmatrix}. \tag{2.46}$$

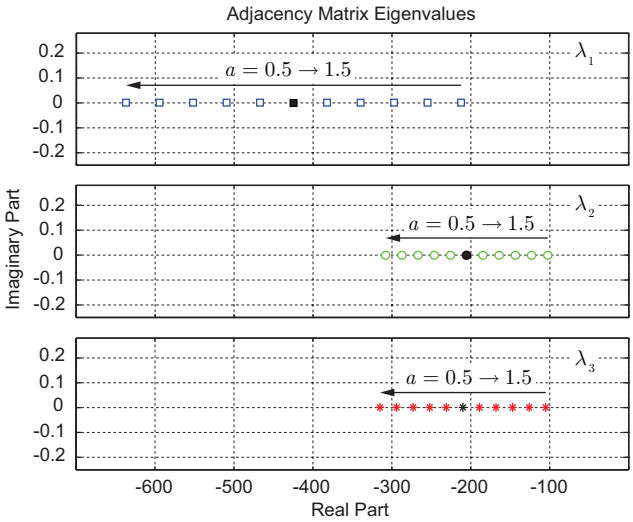

Figure 2-8 Movement of the eigenvalues of the adjacency matrix as the scaling coefficient changes.

Figure 2-8 shows how the eigenvalues of the adjacency matrix vary as the scaling coefficient, a, changes from 0.5 to 1.5. The dominant pole of the converters' transfer function is $p_1 = -106$. Eigenvalues of $\mathbf{A_G}$, λ_ks, are highlighted in Fig. 2-8 in black for $a = 1$, where $\forall k \leq 3,\ \left|\text{real}(\lambda_k)\right| > 2 \times \left|\text{real}(p_1)\right|$. Therefore, $a = 1$ provides an appropriate scaling coefficient for the adjacency matrix in (2.46). It should be noted that the non-zero matrix entries in (2.46) are arbitrarily chosen and other selections are viable; however, they might result in a different optimal scaling factor.

The performance of the noise-cancellation module is evaluated numerically using (2.23). The coupling gain, b, and the NC integrator gain matrix, $\mathbf{K}$, are chosen (see Appendix C) to provide higher than 65% attenuation for disturbances with $f_{\text{noise}} < 5\ \text{Hz}$. The noise-cancellation transfer function, $\mathbf{H}_{\text{NC}}$, is plotted in Fig. 2-9 for the first node.

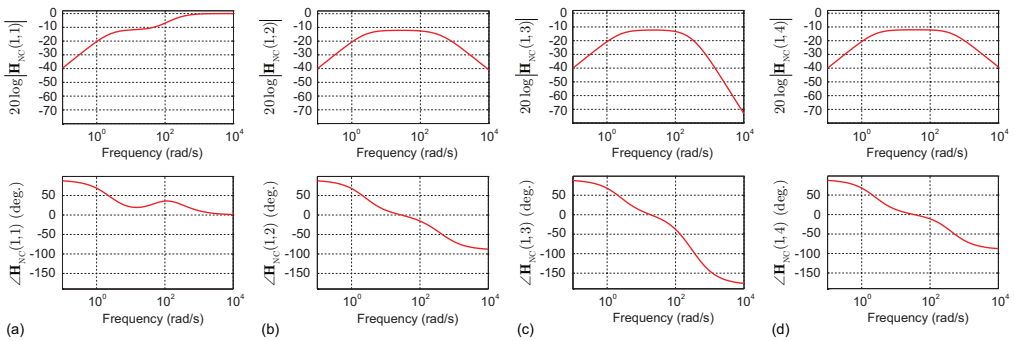

Figure 2-9 Frequency response of the noise-cancellation module at the first node: a) $\mathbf{H}_{\mathrm{NC}}(1,1)$, (b) $\mathbf{H}_{\mathrm{NC}}(1,2)$, (c) $\mathbf{H}_{\mathrm{NC}}(1,3)$, (d) $\mathbf{H}_{\mathrm{NC}}(1,4)$.

As seen, all terms of $\mathbf{H}_{\mathrm{NC}}$ are stable functions and exhibit satisfactory attenuations as demonstrated by the low gain at low frequencies. This implies successful noise rejection for DC and low-frequency disturbances. Similar performance is observed for the NC modules at other nodes.

Comparison between (2.7) and (2.22) shows that NC modules can affect the observers' transfer function. Proper selection of the coupling gain, b, and the matrix $\mathbf{K}$ can significantly suppress this impact. Figure 2-10 compares the first entry, $(1,1)$, of the total observers' transfer function, $\mathbf{H}_{\mathrm{obs}}^{\mathrm{F}}$, with the reduced-order function, $\mathbf{H}_{\mathrm{obs}}$, where it can be seen that the NC module has a negligible impact on observers' the frequency response. A similar match is observed between other entries of $\mathbf{H}_{\mathrm{obs}}^{\mathrm{F}}$ and corresponding entries of $\mathbf{H}_{\mathrm{obs}}$. Accordingly, one can safely assume $\mathbf{H}_{\mathrm{obs}}^{\mathrm{F}} = \mathbf{H}_{\mathrm{obs}}$.

The current regulator module carries out the load sharing regardless of the selection of the droop coefficients.

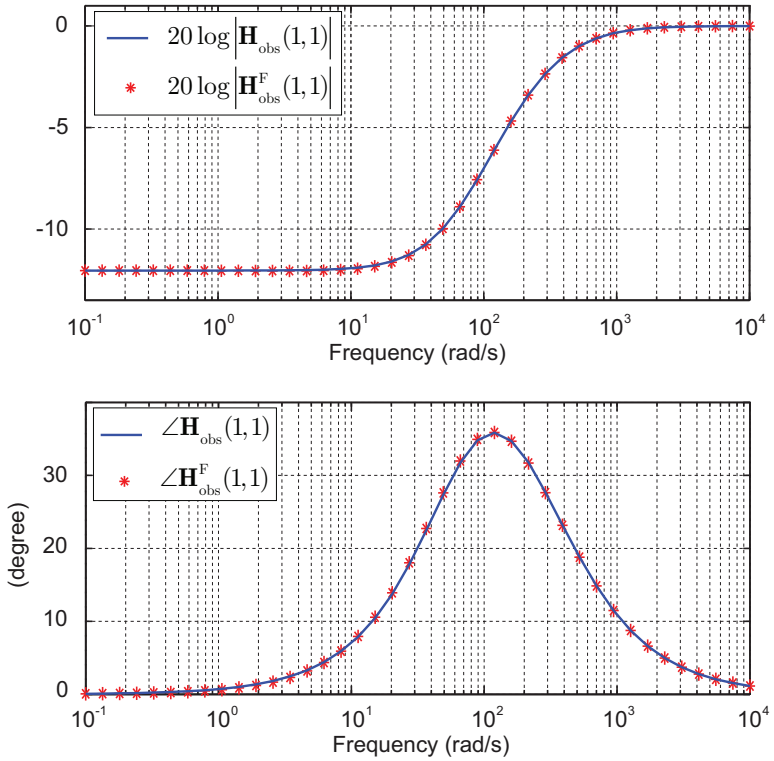

Figure 2-10 Comparison of the reduced-order observers' dynamic, $\mathbf{H}_{\text{obs}}(1,1)$, and the total observers' dynamic, $\mathbf{H}^{\text{F}}_{\text{obs}}(1,1)$.

However, the choice of the coefficients based on (2.35) improves the load sharing dynamics. Accordingly, $m=3$ is chosen here, which results in the virtual impedance matrix, $\mathbf{r}$, provided in the Appendix C.

The coupling gain between the current and the voltage regulator, c, determines load sharing dynamics. Figure 2-11 compares the measured dynamic response of the microgrid for two different values of c. Small coupling gain c can slow down the system while a large coupling gain can lead to resonance or even make the system unstable. A medium value is adopted here, i.e., $c = 0.075$. Satisfactory system performance is verified empirically.

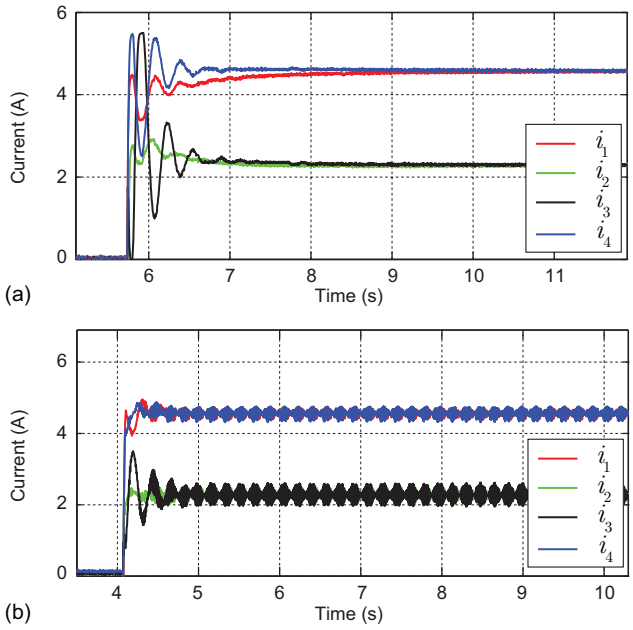

Figure 2-11 Current regulating performance for small and large coupling gains; measured output currents for: a) $c = 0.005$ stable and very slow, b) $c = 0.15$ fast and resonating.

Although (2.34) provides analytical evaluation of system dynamic, it does not consider limitations such as constraint on the duty cycle of the switching converters and, thus, empirical performance evaluation is preferred instead. Design parameters are summarized in the Appendix C. As seen, dissimilar control parameters are selected for different converters to verify controller performance in the case of heterogeneous agents (sources).

2.5.2. Droop Controller versus Proposed Controller

Figure 2-12 comparatively studies the performance of the proposed methodology. The microgrid is initially controlled using the conventional droop controller. It leads to voltages less than the desired value, i.e., $v_{\text{ref}} = 48\ \text{V}$.

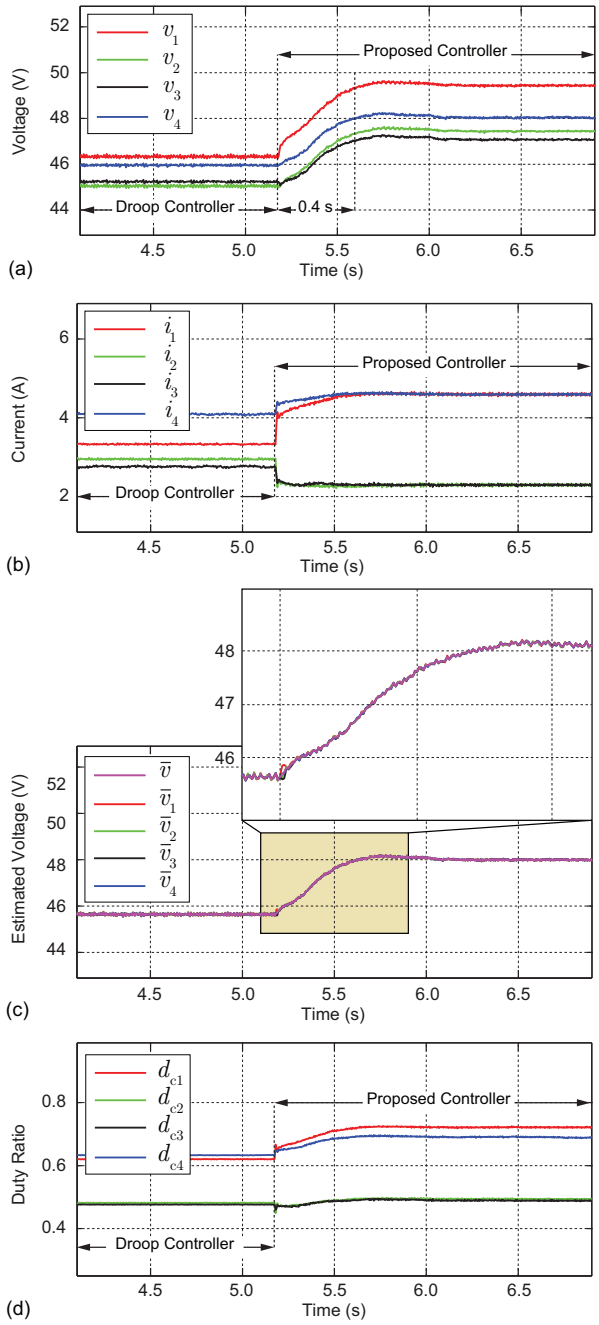

Figure 2-12 Comparative studies of the conventional droop control and the proposed controller: (a) terminal voltages, (b) supplied currents, (c) estimations of the average voltage, (d) converters' duty ratios.

In addition, although the droop gains are designed reciprocal to the converters' rated currents, the transmission line effects have clearly incapacitated the droop mechanism resulting in a poor load sharing. The proposed controller is engaged at $t = 5.18\ \mathrm{s}$. Consequently, the voltages are all boosted across the microgrid and the average voltage is finely regulated at the set point, i.e., $v_{\mathrm{ref}} = 48\ \mathrm{V}$. Figure 2-12(b) shows that the proportional load sharing is also carried out, where the first and the fourth converters carry twice the current as the other two converters. Performance of the voltage observers is studied in Fig. 2-12(c), where a good agreement is seen between the true average voltage, $\overline{v}$, and the individual estimated voltages, $\overline{v}_i$ s.

The efficacy of the noise cancellation module is studied in Fig. 2-13, where a step disturbance, i.e., $d_1(t) = 2u(t - 3.35\ \mathrm{s})$, is intentionally applied to the estimation at node one. It can be seen in Fig. 2-13(c) that the disturbance causes sudden increase in all estimations. Accordingly, the controller has slightly decreased the duty ratios. Simultaneously, the NC module has identified the noise and adjusted the cancellation term, $\hat{d}_1$, to neutralize the noise impact. Consequently, all estimations are recovered in less than $1\ \mathrm{s}$ and continue tracking the true average voltage, $\overline{v}$. Figures 2-13(a) and 2-13(b) show that the NC module has effectively eliminated the noise impact on the voltage regulation and the load sharing.

2.5.3. Load Change Performance Assessment

The controller performance in case of load change is studied in Fig. 2-14, where the remote load at bus five, R_5, is changed in step between $10\ \Omega$ and $20\ \Omega$. Tight voltage regulation and load sharing can be observed in this figure. Excellent transient load sharing is also noticeable in Fig. 2-14(b).

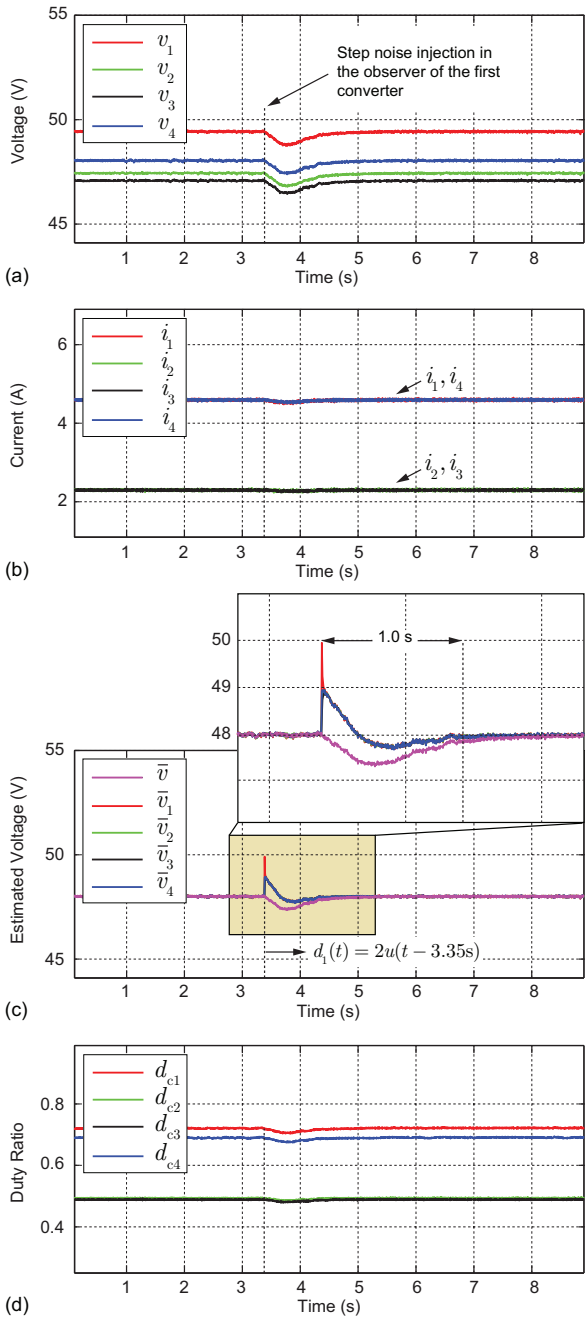

Figure 2-13 Performance of the noise cancellation mechanism: (a) terminal voltages, (b) supplied currents, (c) estimations of the average voltage, (d) converters' duty ratios.

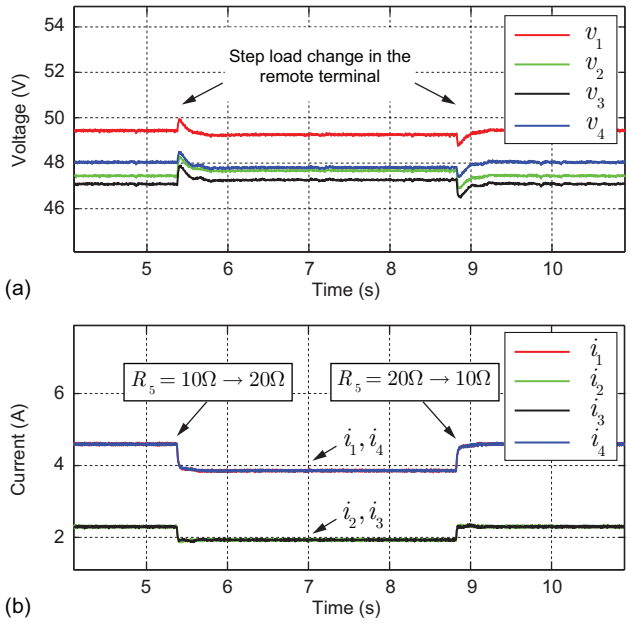

Figure 2-14 Performance of the cooperative distributed controller in a case of load change: (a) terminal voltages, (b) supplied currents.

2.5.4. Plug-and-Play Capability

Figure 2-15 studies plug-and-play capability of the proposed method and its performance in case of a converter failure. As seen, when the second converter fails, the controller readjusts the voltages to satisfy the global voltage regulation. It also readjusts the load sharing among the remaining converters. It should be noted that a converter failure also implies loss of all communication links connected to that particular converter. Accordingly, when the second converter fails, it automatically renders the links 1-2 (between nodes 1 and 2) and 2-3 inoperable. However, the remaining links still form a connected graph with balanced Laplacian matrix (see Fig. 2-6(c)). Then, the second converter is plugged back in at $t = 12.1$ s. As seen, the controller has properly updated the load sharing, and global voltage regulation, after the second converter is plugged in.

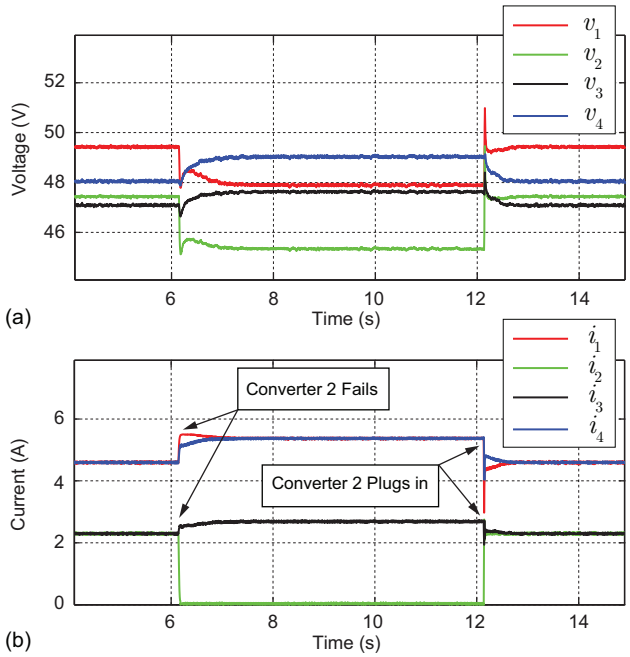

Figure 2-15 Converter failure and plug-and-play studies: (a) terminal voltages, (b) supplied currents.

2.5.5. Link-Failure Resiliency

Resiliency to a single link failure is studied next in Fig. 2-16. The original communication graph is designed to carry a minimum redundancy, so no single link failure can cause loss of graphical connectivity. Thus, the control system shall remain operational. As seen in Fig. 2-16, the link 1-2 has failed at $t = 11$ s, but it does not have any impact on voltage regulation or load sharing.

Response of the controller to the step load change in the remote load is also studied with the failed link, where a satisfactory performance can be seen. It should be noted that the reconfiguration caused by the link failure affects the Laplacian matrix and, thus, the whole system dynamic. Comparing Figs. 2-14(b) and 2-16(b), one can see that the link failure slightly slows the controller transient response.

2.6. Summary

A distributed secondary/primary controller is proposed for DC microgrids. The controller on each converter has two modules; the voltage regulator and the current regulator. The voltage regulator uses a noise-resilient voltage observer to estimate the global average voltage. This estimation is then further used to adjust the local voltage set point to provide global voltage regulation. The current regulator compares local per-unit current with its neighbors' per-unit currents and, accordingly, adjusts the voltage set point to carry out proportional load sharing. This control paradigm uses a sparse communication network for data exchange. Studies show that the proposed cooperative control provides precise global voltage regulation and proportional load sharing. Noise resiliency of the proposed voltage observer and link-failure resiliency of the overall control structure are also verified through experiments.

Chapter 3

Distributed Adaptive Droop Control for DC Distribution Systems

Proper load sharing assigns the load among participating converters in proportion to their rated powers (or, equivalently, rated currents). This approach equalizes the per-unit currents of all sources, and prevents circulating currents [83] and overstressing of any source [84]. The droop control is widely adopted for load sharing by imposing virtual output impedance on each converter [85], [86]. Static/dynamic performance and stability assessment of droop controllers are investigated in [64], [87], and [88]. Constant droop is commonly used for power reference tracking and load sharing in grid-connected and islanded modes, respectively [89], [90]. However, its load sharing performance is susceptible to transmission line impedances [91]. Generally, higher droop coefficients result in improved load sharing, however, at the cost of further degrading the voltage regulation. Thus, to achieve a desirable load sharing, the droop coefficients should vary to account for line impedances and load variations. Moreover, since some sources (e.g., PV-driven modules or storage devices) lack a constant rated power, dynamic adjustment of droop coefficients is required as their rated power changes [92].

A piece-wise linear droop mechanism in [92] and [93] uses two different droop gains for low and high powers. The idea is further developed in [94] and [95] where droop coefficients continuously vary in response to change in power. This approach improves voltage regulation; however, voltage drop across the microgrid is still noticeable. This method is developed for two-agent systems and extension to a multi-converter system is not straightforward. Moreover, improved voltage regulation has compromised accurate proportional load sharing. Adaptive-droop control for power flow control in grid-connected mode is studied in [96], [97]. Droop gains are adjusted in reciprocal to power demand in

[98] where communication of a synchronization signal is needed among all converters. This requirement, in turn, compromises the plug-and-play capability. Decentralized [84] and supervisory [99] adaptive-droop approaches formulate droop gains in terms of batteries' state of charges [100].

Existing droop mechanisms generally suffer from poor voltage regulation and load sharing, particularly when the distribution line impedances are not negligible [101]–[103]. Possible solutions to the aforementioned issues have been reviewed in [79]. These solutions are either structured centrally [70] or require development of a fully connected data exchange network across the microgrid, where any two nodes are in direct contact [85], [104]–[106]. Assuming equal voltages for all converters across the microgrid in [70] is not practical, particularly, in DC distribution systems. Point-to-point communication links are required for all sources in [107], where any link failure renders the whole microgrid inoperable. The line impedance is taken into account in [108], where the data exchange requires a fully connected communication graph. Proper operation of the controller demands information of all nodes and, thus, any link failure impairs the whole control functionality. Scalability is another challenge; after any structural/electrical upgrade, some control settings, e.g., the number of sources, need to be updated and embedded in all converters.

The voltage regulation requirement is redefined in [109] to incorporate the line impedance effect. The average voltage across the microgrid (and only not a specific bus voltage) should be regulated at the global voltage set point determined by the tertiary control. This is called the global voltage regulation, and is considered here. Tertiary control levels would involve distributed optimization techniques to implement economical dispatch and/or loss optimization, and is the subject of future work. This chapter focuses

on the secondary/primary control of the DC microgrids and offers the following contributions:

- Each converter is augmented with a current regulator that compares the actual per-unit current of that converter with a weighted average of its neighbors' and, accordingly, generates an impedance correction term to adjust droop coefficient and, thus, provide proportional load sharing.
- A voltage regulator is also added. This regulator uses the estimation made by a voltage observer to adjust the local voltage set point and provide global voltage regulation.
- The voltage observer processes neighbors' data and local voltage measurement through a so-called dynamic consensus protocol to estimate the global average voltage.
- Cooperation of the voltage and current regulators is shown to effectively carry out both global voltage regulation and proportional load sharing, particularly, when the line impedances are not negligible.
- A sparse communication network is spanned across the microgrid to enable limited message passing among converters; each converter only exchanges data with its neighbors. This is in direct contrast to the centralized control approaches that require communication networks with high-bandwidth communication links and a high level of connectivity.
- This adaptive droop approach expands the work of authors in [109] and achieves a faster load sharing dynamics.
- Compared to the existing techniques (e.g., [108]) the control scheme employs a truly distributed approach that does not require a priori knowledge of the global

parameters such as the number of sources. Thus, it is scalable and suitable for the plug-and-play operation.

- Unlike existing methods that require fully connected graphs and may fail in case of any communication link failure, the proposed method is not susceptible to any single link failure, which leads to a more reliable control framework.

3.1. Distributed Cooperative Control Framework

Microgrid sources are mapped to a cyber network as shown in Fig. 3-1, where each node represents an active source (or, converter) and each edge represents a communication link for data exchange. The communication graph might have a different topology than the underlying physical microgrid. This cyber connection sets the groundwork for the cooperative control paradigm, where neighbors' interactions can lead to a global consensus. Accordingly, not all agents (converters) in a large-scale dynamic system need to be in direct contact. Instead, each agent only communicates its control variables with its neighbors. Then, using the neighbors' data and its local measurements, the agent updates its control variables. The cooperative control offers global consensus of the desired variables, shall the communication graph be designed properly.

A directed graph (digraph), associated with the cyber layer in microgrid, is highlighted in Fig. 3-1. Such a graph is usually represented as a set of nodes $\mathbf{V}_{\mathbf{G}} = \{v_1^{\mathrm{g}}, v_2^{\mathrm{g}}, ..., v_N^{\mathrm{g}}\}$ connected via a set of edges $\mathbf{E}_{\mathbf{G}} \subset \mathbf{V}_{\mathbf{G}} \times \mathbf{V}_{\mathbf{G}}$, and an associated adjacency matrix $\mathbf{A}_{\mathbf{G}} = [a_{ij}] \in \mathbb{R}^{N \times N}$. The Adjacency matrix $\mathbf{A}_{\mathbf{G}}$ contains communication weights, where $a_{ij} > 0$ if $(v_j^{\mathrm{g}}, v_i^{\mathrm{g}}) \in \mathbf{E}_{\mathbf{G}}$ and $a_{ij} = 0$, otherwise. a_{ij} is the communication weight for data transfer from node j to node i.

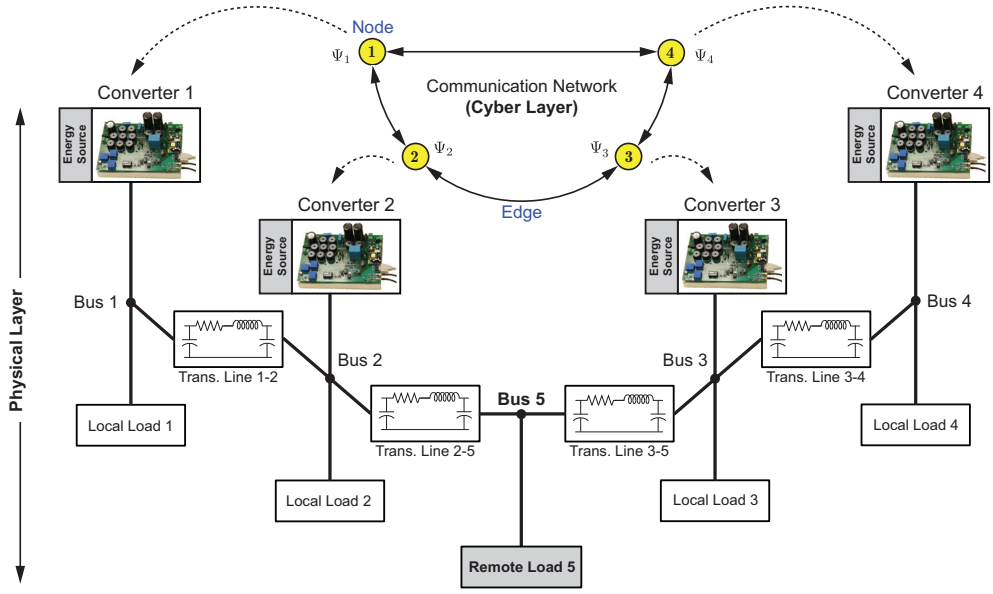

Figure 3-1 General layout of a DC microgrid including energy sources supplying the grid and the cyber network facilitating data exchange among sources.

Here, a time-invariant adjacency matrix is assumed. $N_i = \{j \mid (v_j^g, v_i^g) \in \mathbf{E}_G\}$ denotes the set of all neighbors of node i, i.e., if $j \in N_i$, then v_i^g receives information from v_j^g. However, in a digraph, the link is not necessarily reciprocal, i.e., v_j^g might not receive information from v_i^g. The in-degree matrix $\mathbf{D}_\mathbf{G}^{\text{in}} = \text{diag}\{d_i^{\text{in}}\}$ is a diagonal matrix with $d_i^{\text{in}} = \sum_{j \in N_i} a_{ij}$. Similarly, the out-degree matrix is $\mathbf{D}_\mathbf{G}^{\text{out}} = \text{diag}\{d_i^{\text{out}}\}$, where $d_i^{\text{out}} = \sum_{i \in N_j} a_{ji}$. The Laplacian matrix is then defined as $\mathbf{L} = \mathbf{D}_\mathbf{G}^{\text{in}} - \mathbf{A}_\mathbf{G}$, whose eigenvalues determine the global dynamics [110]. The Laplacian matrix is balanced if the in-degree of each node matches its out-degree, i.e., $\mathbf{D}_\mathbf{G}^{\text{in}} = \mathbf{D}_\mathbf{G}^{\text{out}}$. Particularly, if the graph is undirected, i.e., all links are bidirectional, then the Laplacian matrix is balanced. A

direct path from v_i^g to v_k^g is a sequence of edges that connects the two nodes. A digraph is said to have a spanning tree if it contains a root node, from which there exists at least a direct path to every other node.

The physical layer of the microgrid, shown in Fig. 3-1, includes dispatchable sources (including the power converters), transmission lines, and loads. The cyber layer, comprised of all communication links, is spanned among the sources to facilitate data exchange. This is a sparse communication network with at least one spanning tree. In addition, the graph is chosen such that in case of any link failure the remaining network still contains at least one spanning tree. This redundancy is required to ensure link-failure resiliency. Each converter broadcasts a data set, Ψ_i, to its neighbors. The data package transmitted by node i, $\Psi_i = [\overline{v}_i, i_i^{\mathrm{pu}}]$, consists of two elements; its estimate of the average voltage across the microgrid, $\overline{v}_i$, and the measured per-unit current, i_i^{pu}. The term per-unit here refers to the current provided by the converter divided by its rated current, i.e., $i_i^{\mathrm{pu}} \triangleq i_i \big/ I_i^{\mathrm{rated}}$, where i_i and I_i^{rated} are the supplied and rated currents of the i–th converter, respectively. This terminology of the per-unit is used here to represent loading percentage of each converter. At the receiving ends of the communication links, each converter k receives data from all its neighbors, Ψ_j, $j \in N_k$, with associated communication weights, a_{kj}. These weights are design parameters and can be considered as data transfer gains.

3.2. Adaptive Droop Control

The global voltage regulation and proportional load sharing are the two objectives of the secondary control, which require proper voltage set point assignment for individual converters.

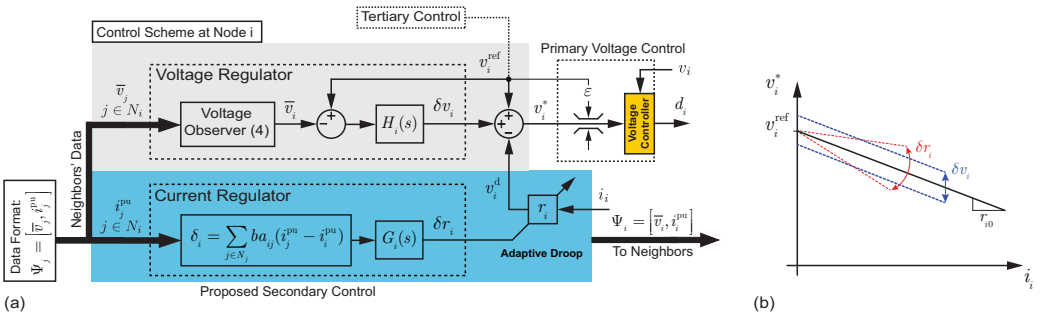

Figure 3-2 Proposed distributed control policy: (a) cooperative adaptive droop control for a single agent (converter), (b) effect of adjustable voltage correction and virtual impedance on the droop characterization.

The proposed secondary controller is elaborated in Fig. 3-2(a), where local and neighbors' information are processed to adjust the local voltage set point, v_i^*. Cooperation among converters, at the secondary control level, helps to fine-tune the voltage set points, v_i^*, and mitigate the current and voltage residues.

The voltage set point for each converter is augmented with two terms provided through cooperation among converters. They are resulted from voltage and current regulators. Based on Fig. 3-2(a), the local voltage set point for an individual converter can be expressed as

$$v_i^* = v_i^{\text{ref}} - v_i^{\text{d}} + \delta v_i = v_i^{\text{ref}} - r_i i_i + \delta v_i, \tag{3.1}$$

where v_i^{ref}, v_i^{d}, δv_i, and r_i are the global reference voltage, droop voltage, voltage correction term, and the virtual impedance of the i–th converter, respectively. This set point is further adjusted by a voltage limiter (see Fig. 3-2(a)) to maintain the bus voltages within an acceptable range. Figure 3-2(b) elaborates how adjustable voltage correction term, δv_i, and virtual impedance, r_i, can navigate operating point of the converter. The

droop mechanism, which generates the term $r_i i_i$ in (3.1), characterizes output impedance of the converters and helps to share load, which leads to the voltage drop across the microgrid. The voltage correction terms, δv_i s, are augmented to the local reference voltages to boost the voltage across the microgrid. Accordingly, the controller contains two modules; a voltage regulator and a current regulator.

The voltage regulator at node i consists of a voltage observer and a PI controller, $H_i(s)$. The voltage observer at each node estimates the averaged voltage across the microgrid, where $\overline{v}_i$ is the estimation at node i. This estimation is then compared with the global reference voltage, v_i^{ref}, to generate the voltage correction term, δv_i. In case of any mismatch between $\overline{v}_i$ and v_i^{ref}, the controller adjusts δv_i to eliminate the discrepancy. In the islanded mode of operation, the global reference voltages, v_i^{ref} s, are typically identical and equal to the rated voltage of the microgrid. However, in the grid-tied mode, the tertiary control sets a new voltage level for the microgrid and relays the new reference values to individual converters. A cooperative observer will process the local voltage measurement and the neighbors' estimates to evaluate the average voltage across the microgrid. Functionality of the observer is discussed in detail in Section 3.3.

The current regulator at node i provides the input to the droop mechanism. The droop mechanism characterizes the converter output impedance using the virtual impedance r_i. Virtual impedances are conventionally initialized in reciprocal to the converters' rated current, i.e., $r_{i0} = m \big/ I_i^{\text{rated}}$, where m is a design parameter and is identical for all converters. However, the distribution line impedances compromise

performance of the droop controller. Thus, the droop gains are suggested to adapt according to the microgrid loading condition. To this end, a cooperative current regulator is included in the secondary control of any converter, e.g., converter i, which compares local per-unit current, i_i^{pu}, with the weighted average of the neighbors' per-unit currents and finds the current mismatch, δ_i,

$$\delta_i = \sum_{j \in N_i} b a_{ij} (i_j^{\mathrm{pu}} - i_i^{\mathrm{pu}}). \tag{3.2}$$

where b is the coupling gain between the voltage and current regulators. This mismatch is then fed to a PI controller, $G_i(s)$, to generate an impedance correction term, δr_i, which updates the virtual impedance,

$$r_i(t) = r_{i0} - \delta r_i(t). \tag{3.3}$$

If the per-unit currents of any two neighbors' differ, the current regulators of the corresponding converters respond and adjust their impedance correction terms to achieve balance.

3.3. Voltage Observer

The observer is the primary stage of the voltage regulator module, as shown in Fig. 3-2. It uses a dynamic cooperative framework to process local and neighbors' information and estimate the average voltage across the microgrid. Figure 3-3 explains the distributed cooperative policy for global averaging. The observer at node i receives its neighbors' estimates, $\overline{v}_j$ s ($j \in N_i$). Then, the observer updates its own estimate, $\overline{v}_i$, by processing the neighbors' estimates and the local voltage measurement, v_i,

$$\overline{v}_i(t) = v_i(t) + \int_0^t \sum_{j \in N_i} a_{ij} \left(\overline{v}_j(\tau) - \overline{v}_i(\tau) \right) \mathrm{d}\tau. \tag{3.4}$$

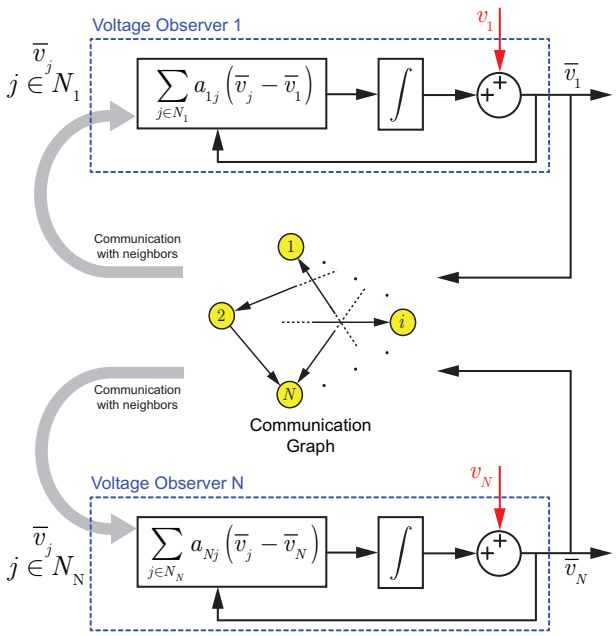

Figure 3-3 Dynamic consensus protocol for averaging voltage across a microgrid; estimating policy at each node.

This updating protocol is referred to as *dynamic consensus* in the literature [111]. As seen in (3.4), the local measurement, i.e., v_i, is directly fed into the estimating protocol. Thus, in case of any voltage variation at node i, the local estimate, $\overline{v}_i$, immediately responds. Then, the change in $\overline{v}_i$ propagates through the communication network and affects all other estimations. By differentiating (3.4),

$$\dot{\overline{v}}_i = \dot{v}_i + \sum_{j\in N_i} a_{ij}\left(\overline{v}_j - \overline{v}_i\right) = \dot{v}_i + \sum_{j\in N_i} a_{ij}\overline{v}_j - d_i^{\text{in}}\overline{v}_i. \tag{3.5}$$

The global observer dynamic can be formulate accordingly,

$$\dot{\overline{\mathbf{v}}} = \dot{\mathbf{v}} - \left(\mathbf{D}_{\mathbf{G}}^{\text{in}} - \mathbf{A}_{\mathbf{G}}\right)\overline{\mathbf{v}} = \dot{\mathbf{v}} - \mathbf{L}\overline{\mathbf{v}}, \tag{3.6}$$

where the voltage measurement vector, $\mathbf{v} = [v_1, v_2, \ldots, v_N]^{\mathrm{T}}$, carries measured voltage of all nodes. Similarly, the voltage estimation vector, $\bar{\mathbf{v}} = [\bar{v}_1, \bar{v}_2, \ldots, \bar{v}_N]^{\mathrm{T}}$, contains the global average voltage estimated by all nodes. Equivalently, in the frequency domain,

$$s\bar{\mathbf{V}} - \bar{\mathbf{v}}(0) = s\mathbf{V} - \mathbf{v}(0) - \mathbf{L}\bar{\mathbf{V}}, \tag{3.7}$$

where $\mathbf{V}$ and $\bar{\mathbf{V}}$ are the Laplace transforms of $\mathbf{v}$ and $\bar{\mathbf{v}}$, respectively. Equation (3.4) implies that $\mathbf{v}(0) = \bar{\mathbf{v}}(0)$. Therefore,

$$\bar{\mathbf{V}} = s(s\mathbf{I}_N + \mathbf{L})^{-1}\mathbf{V} = \mathbf{H}_{\mathrm{obs}}\mathbf{V}, \tag{3.8}$$

where $\mathbf{I}_N \in \mathbb{R}^{N\times N}$ and $\mathbf{H}_{\mathrm{obs}}$ are the identity matrix and the observer transfer function, respectively. Equation (3.8) represents the global dynamics of the voltage observers. It is shown in [109] that if $\mathbf{L}$ is balanced, then all entries of the voltage estimation vector, $\bar{\mathbf{v}}$, converge to a consensus value, which is the true average voltage, i.e., the average of all entries in $\mathbf{v}$. In other words,

$$\bar{\mathbf{v}}^{\mathrm{ss}} = \mathbf{Q}\mathbf{v}^{\mathrm{ss}} = \left\langle \mathbf{v}^{\mathrm{ss}} \right\rangle \underline{\mathbf{1}}, \tag{3.9}$$

where $\mathbf{Q} \in \mathbb{R}^{N\times N}$ is the averaging matrix, whose elements are all equal to $1/N$. $\underline{\mathbf{1}} \in \mathbb{R}^{N\times 1}$ is a vector whose elements are all equal to one. $\mathbf{x}^{\mathrm{ss}}$ and $\langle \mathbf{x} \rangle$ represent the steady-state value of the vector $\mathbf{x} \in \mathbb{R}^{N\times 1}$ and the average of all vector elements, respectively.

3.4. Global Model Development

Global model development is essential to study how the proposed controller affects the transient response and steady-state operation of the microgrid. This model can be used to tune the design parameters and achieve any desired dynamic.

3.4.1. Global Dynamic Model

Switching nature of power electronic converters can potentially result in a nonlinear system. Accordingly, small-signal methods are commonplace for dynamic

characterization purposes (e.g., via averaging) [112]. Such tools are suitable for relatively small disturbances, e.g., as shown in [113], [114]. Thus, small-signal modeling is considered here, where, each variable x is written as $x = x^{\mathrm{q}} + \hat{x}$, where x^{q} and $\hat{x}$ are the quiescent and small-signal perturbation parts, respectively. This representation helps to linearly express the droop voltage for the i–th converter, v_i^{d}, as

$$v_i^{\mathrm{d}} = v_i^{\mathrm{d,q}} + \hat{v}_i^{\mathrm{d}} = \left(r_i^{\mathrm{q}} + \hat{r}_i\right)\left(i_i^{\mathrm{q}} + \hat{i}_i\right). \tag{3.10}$$

By neglecting the second-order term, i.e., $\hat{r}_i \hat{i}_i \approx 0$, (3.10) can be reduced to

$$\hat{v}_i^{\mathrm{d}} = r_i^{\mathrm{q}} \hat{i}_i + i_i^{\mathrm{q}} \hat{r}_i. \tag{3.11}$$

Let $\hat{\mathbf{v}}_{\mathrm{ref}} = [\hat{v}_1^{\mathrm{ref}}, \hat{v}_2^{\mathrm{ref}}, ..., \hat{v}_N^{\mathrm{ref}}]^{\mathrm{T}}$ and $\hat{\mathbf{i}} = [\hat{i}_1, \hat{i}_2, ..., \hat{i}_N]^{\mathrm{T}}$ be the small-signal vectors of the rated voltages and actual supplied currents, respectively. Similarly, $\hat{\mathbf{v}}$, $\hat{\mathbf{v}}^{\mathrm{d}}$, $\Delta\hat{\mathbf{v}}$, $\hat{\mathbf{r}}$, and $\hat{\mathbf{v}}^{*}$ are column vectors containing small-signal portions of the output voltages, droop voltages, voltage correction terms, virtual impedances, and local voltage set points, respectively. $\mathbf{r}^{\mathrm{q}}$ and $\mathbf{i}^{\mathrm{q}}$ are vectors of quiescent virtual impedances and currents, respectively. $\mathbf{I}_{\mathrm{rated}} = \mathrm{diag}\{I_i^{\mathrm{rated}}\}$ is a diagonal matrix containing rated currents of individual sources. $\hat{\mathbf{V}}_{\mathrm{ref}}$, $\hat{\mathbf{I}}$, $\hat{\mathbf{V}}$, $\hat{\mathbf{V}}^{\mathrm{d}}$, $\Delta\hat{\mathbf{V}}$, $\hat{\mathbf{R}}$, and $\hat{\mathbf{V}}^{*}$ are the Laplace transforms of $\hat{\mathbf{v}}_{\mathrm{ref}}$, $\hat{\mathbf{i}}$, $\hat{\mathbf{v}}$, $\hat{\mathbf{v}}^{\mathrm{d}}$, $\Delta\hat{\mathbf{v}}$, $\hat{\mathbf{r}}$, and $\hat{\mathbf{v}}^{*}$, respectively. Based on Fig. 3-2,

$$\mathbf{H}\left(\hat{\mathbf{V}}_{\mathrm{ref}} - \hat{\bar{\mathbf{V}}}\right) = \Delta\hat{\mathbf{V}}, \tag{3.12}$$

where $\mathbf{H} = \mathrm{diag}\{H_i(s)\}$ is the voltage controller matrix. By using (3.3), $\hat{r}_i = -\delta\hat{r}_i$, thus,

$$-b\mathbf{G}\mathbf{L}\mathbf{I}_{\mathrm{rated}}^{-1}\hat{\mathbf{I}} = -\hat{\mathbf{R}}, \tag{3.13}$$

where $\mathbf{G} = \mathrm{diag}\{G_i(s)\}$ is the current controller matrix. Substituting the observer transfer function, $\mathbf{H}_{\mathrm{obs}}$, from (3.8) in (3.12) yields,

$$\Delta\hat{\mathbf{V}} = \mathbf{H}\left(\hat{\mathbf{V}}_{\text{ref}} - \mathbf{H}_{\text{obs}}\hat{\mathbf{V}}\right). \tag{3.14}$$

In addition, (3.11) can be written in the global form,

$$\hat{\mathbf{V}}^{\text{d}} = \mathrm{T}\left(\mathbf{r}^{\text{q}}\right)\hat{\mathbf{I}} + \mathrm{T}\left(\mathbf{i}^{\text{q}}\right)\hat{\mathbf{R}}, \tag{3.15}$$

where $\mathrm{T}(\cdot):\mathbb{R}^{N\times 1} \rightarrow \mathbb{R}^{N\times N}$ is a transformation that maps a vector to a diagonal matrix,

$$\mathrm{T}\left([x_1, x_2, \cdots, x_N]^{\mathrm{T}}\right) \triangleq \mathrm{diag}\{x_1, x_2, \cdots, x_N\}. \tag{3.16}$$

The small-signal reference voltage vector, $\hat{\mathbf{v}}^*$, can be derived using (3.1) and (3.13)-(3.15),

$$\begin{aligned}\hat{\mathbf{V}}^* &= \hat{\mathbf{V}}_{\text{ref}} - \hat{\mathbf{V}}^{\text{d}} + \Delta\hat{\mathbf{V}} \\ &= \hat{\mathbf{V}}_{\text{ref}} - \mathrm{T}\left(\mathbf{r}^{\text{q}}\right)\hat{\mathbf{I}} - \mathrm{T}\left(\mathbf{i}^{\text{q}}\right)\hat{\mathbf{R}} + \mathbf{H}\left(\hat{\mathbf{V}}_{\text{ref}} - \mathbf{H}_{\text{obs}}\hat{\mathbf{V}}\right) \\ &= \left(\mathbf{I}_N + \mathbf{H}\right)\hat{\mathbf{V}}_{\text{ref}} - \left(\mathrm{T}\left(\mathbf{r}^{\text{q}}\right) + b\mathrm{T}\left(\mathbf{i}^{\text{q}}\right)\mathbf{G}\mathbf{L}\mathbf{I}_{\text{rated}}^{-1}\right)\hat{\mathbf{I}} \\ &\quad -\mathbf{H}\mathbf{H}_{\text{obs}}\hat{\mathbf{V}}.\end{aligned} \tag{3.17}$$

On the other hand, dynamic behavior of any converter with closed-loop voltage regulator can be expressed as

$$\hat{V}_i = G_i^{\text{c}}(s)\hat{V}_i^*, \tag{3.18}$$

where $\hat{V}_i$ and $\hat{V}_i^*$ are the Laplace transforms of $\hat{v}_i$ and $\hat{v}_i^*$, respectively. G_i^{c} is the closed-loop transfer function of the i–th converter. The closed-loop transfer functions are derived in [112] for a wide variety of converters. Global small-signal dynamic of the converters can be found according to (3.18),

$$\hat{\mathbf{V}} = \mathbf{G}_{\text{c}}\hat{\mathbf{V}}^*, \tag{3.19}$$

where $\mathbf{G}_{\text{c}} = \mathrm{diag}\{G_i^{\text{c}}\}$ is the converters' transfer function matrix. By substituting (3.19) in (3.17),

$$\begin{aligned}&\left(\mathbf{G}_{\text{c}}^{-1} + \mathbf{H}\mathbf{H}_{\text{obs}}\right)\hat{\mathbf{V}} = \\ &\qquad \left(\mathbf{I}_N + \mathbf{H}\right)\hat{\mathbf{V}}_{\text{ref}} - \left(\mathrm{T}\left(\mathbf{r}^{\text{q}}\right) + b\mathrm{T}\left(\mathbf{i}^{\text{q}}\right)\mathbf{G}\mathbf{L}\mathbf{I}_{\text{rated}}^{-1}\right)\hat{\mathbf{I}}.\end{aligned} \tag{3.20}$$

For a DC microgrid, it is a common practice to assume that the transmission/distribution line and load impedances are predominantly resistive [115]. Accordingly, one can use the microgrid conductance matrix, $\mathbf{g}_{\text{bus}}$, to relate supplied currents to the bus voltages,

$$\mathbf{i} = \mathbf{g}_{\text{bus}}\mathbf{v}. \tag{3.21}$$

Small-signal perturbation expands (3.21),

$$\left(\mathbf{i}^{\text{q}} + \hat{\mathbf{i}}\right) = \left(\mathbf{g}_{\text{bus}}^{\text{q}} + \hat{\mathbf{g}}_{\text{bus}}\right)\left(\mathbf{v}^{\text{q}} + \hat{\mathbf{v}}\right). \tag{3.22}$$

The small-signal portion of the conductance matrix, $\hat{\mathbf{g}}_{\text{bus}}$, models any small-signal changes in the conductance matrix, $\mathbf{g}_{\text{bus}}$, caused by load change or transmission network reconfiguration. Neglecting the second-order term, i.e., $\hat{\mathbf{g}}_{\text{bus}}\hat{\mathbf{v}} \approx \mathbf{0}$, simplifies (3.22),

$$\hat{\mathbf{i}} = \mathbf{g}_{\text{bus}}^{\text{q}}\hat{\mathbf{v}} + \hat{\mathbf{g}}_{\text{bus}}\mathbf{v}^{\text{q}}. \tag{3.23}$$

Or, equivalently, in the frequency domain,

$$\hat{\mathbf{I}} = \mathbf{g}_{\text{bus}}^{\text{q}}\hat{\mathbf{V}} + \hat{\mathbf{G}}_{\text{bus}}\mathbf{v}^{\text{q}}. \tag{3.24}$$

where $\hat{\mathbf{G}}_{\text{bus}}$ is the Laplace transform of $\hat{\mathbf{g}}_{\text{bus}}$. Substituting (3.24) in (3.20) provides the global dynamic model of the microgrid with the proposed controller in effect,

$$\begin{aligned}\left(\mathbf{G}_{\text{c}}^{-1} + \mathbf{H}\mathbf{H}_{\text{obs}} + \left(\mathrm{T}\left(\mathbf{r}^{\text{q}}\right) + b\mathrm{T}\left(\mathbf{i}^{\text{q}}\right)\mathbf{G}\mathbf{L}\mathbf{I}_{\text{rated}}^{-1}\right)\mathbf{g}_{\text{bus}}^{\text{q}}\right)\hat{\mathbf{V}} = \\ \left(\mathbf{I}_N + \mathbf{H}\right)\hat{\mathbf{V}}_{\text{ref}} - \left(\mathrm{T}\left(\mathbf{r}^{\text{q}}\right) + b\mathrm{T}\left(\mathbf{i}^{\text{q}}\right)\mathbf{G}\mathbf{L}\mathbf{I}_{\text{rated}}^{-1}\right)\hat{\mathbf{G}}_{\text{bus}}\mathbf{v}^{\text{q}}.\end{aligned} \tag{3.25}$$

Equation (3.25) implies that the microgrid is systematically a multi-input-multi-output plant where $\hat{\mathbf{V}}^{\text{ref}}$ and $\hat{\mathbf{G}}_{\text{bus}}$ are the inputs and $\hat{\mathbf{v}}$ and $\hat{\mathbf{i}}$ are the outputs. The global dynamic model in (3.25) formulates the transfer function from each input to the primary output, $\hat{\mathbf{v}}$.

3.4.2. Design Approach

For a given microgrid, the matrix of converters' closed-loop transfer functions, $\mathbf{G}_{\text{c}}$, and the current rating matrix, $\mathbf{I}_{\text{rated}}$ are known. The communication graph needs to

be a connected graph with the minimal redundancy defined in Section 3.2, where no single link failure can compromise communication connectivity. Weights of the communication links, a_{ij}, and, thus, the Laplacian matrix, $\mathbf{L}$, may, then, be chosen to provide any desired dynamic response for the voltage observers by evaluating (3.8). It should be noted that the selection of the communication weights must satisfy a balanced Laplacian matrix.

For the given microgrid with known transmission/ distribution network, one can evaluate $\mathbf{g}_{\text{bus}}^{\text{q}}$ assuming base loads at all consumption terminals. Accordingly, quiescent voltage and current vectors ($\mathbf{v}^{\text{q}}$ and $\mathbf{i}^{\text{q}}$, respectively) can be found by iteratively solving (3.26)-(3.27),

$$\mathbf{i}^{\text{q}} = \mathbf{g}_{\text{bus}}^{\text{q}} \mathbf{v}^{\text{q}}, \tag{3.26}$$

$$\mathbf{i}^{\text{pu}^{\text{q}}} = \mathbf{I}_{\text{rated}}^{-1} \mathbf{i}^{\text{q}} = n\underline{\mathbf{1}}, \tag{3.27}$$

where n is a positive real number. The designer may initialize the virtual impedances as

$$\mathbf{r}_0 = m\left[1/I_1^{\text{rated}}, 1/I_2^{\text{rated}}, \cdots, 1/I_N^{\text{rated}}\right]^{\text{T}}, \tag{3.28}$$

where m is a positive scalar design parameter [70]. The adaptive-droop mechanism adjusts the virtual impedances to provide proportional load sharing. Due to the line impedances, this adjustment results in different values than the initial values, i.e., $\mathbf{r}^{\text{q}} \neq \mathbf{r}_0$. However, empirical studies in Section 3.5 will show that the quiescent virtual impedance vector remains almost intact for various operating conditions. Thus, one can run a steady-state numerical analysis to find $\mathbf{r}^{\text{q}}$ for the base load condition and further use it in the design procedure.

Given the Laplacian matrix, $\mathbf{L}$, the observer transfer function, $\mathbf{H}_{\text{obs}}$, the converters' transfer function matrix, $\mathbf{G}_{\text{c}}$, and all other constant vectors in (3.25), one can

use this equation to design the voltage and current controller matrices ($\mathbf{H}$ and $\mathbf{G}$, respectively) and the coupling gain, b, to provide any desired asymptotically stable dynamic response for the entire microgrid, where all poles of the transfer functions extracted from (3.25) lie on the Open Left Hand Plane (OLHP).

3.4.3. Steady-state Analysis

Steady-state analysis of the microgrid operation is essential to ensure that the cooperative controllers satisfy both operational requirements; the global voltage regulation and the proportional load sharing. Since the converters' rated voltages match the microgrid rated voltage, with no loss of generality, one can assume

$$\mathbf{v}_{\text{ref}} = v_{\text{rated}}\underline{\mathbf{1}}, \tag{3.29}$$

where v_{rated} is the microgrid rated voltage. It is also assumed that the control parameters are properly tuned, based on the design approach in Subsection 3.4.2, to stabilize voltage and current throughout the microgrid.

Let's assume that the microgrid voltages and currents are in the steady state for $t \geq t_0$. The voltage and current controller of the i–th converter can be expressed as $H_i = H_i^{\text{P}} + H_i^{\text{I}}/s$ and $G_i = G_i^{\text{P}} + G_i^{\text{I}}/s$, respectively, where H_i^{P} and G_i^{P} are the proportional and H_i^{I} and G_i^{I} are the integral gains. One can show that, with stable voltages, all voltage observers converge to the true average voltage, i.e.,

$$\overline{\mathbf{v}}^{\text{ss}} = \left(\frac{1}{N}\sum_{i=1}^{N} v_i^{\text{ss}}\right)\underline{\mathbf{1}} = \overline{v}^{\text{ss}}\underline{\mathbf{1}}, \tag{3.30}$$

where x^{ss} represents the steady-state value of the variable x. According to Fig. 3-2, for $t \geq t_0$ one can write,

$$\begin{aligned}\Delta\mathbf{v}^{\mathrm{ss}} &= \mathbf{W}_{\mathbf{v}}(t_0) + \mathbf{H}_{\mathrm{P}}(\mathbf{v}_{\mathrm{ref}} - \overline{\mathbf{v}}^{\mathrm{ss}}) \\ &\quad + \mathbf{H}_{\mathrm{I}}(\mathbf{v}_{\mathrm{ref}} - \overline{\mathbf{v}}^{\mathrm{ss}})(t - t_0),\end{aligned} \tag{3.31}$$

where $\mathbf{W}_{\mathbf{v}}(t_0)$ is a vector that carries integrator outputs of the voltage regulators at $t = t_0$.

Similarly,

$$\begin{aligned}\Delta\mathbf{r}^{\mathrm{ss}} &= \mathbf{W}_{\mathbf{r}}(t_0) + \mathbf{G}_{\mathrm{P}}(-b\mathbf{L}\mathbf{i}^{\mathrm{pu}^{\mathrm{ss}}}) \\ &\quad + \mathbf{G}_{\mathrm{I}}(-b\mathbf{L}\mathbf{i}^{\mathrm{pu}^{\mathrm{ss}}})(t - t_0),\end{aligned} \tag{3.32}$$

where $\mathbf{W}_{\mathbf{r}}(t_0)$ is a vector that carries integrator outputs of the current regulators at $t = t_0$.

In the steady state, $\mathbf{v}^{\mathrm{ss}} = \mathbf{v}^{*^{\mathrm{ss}}}$, thus, according to (3.1),

$$\begin{aligned}\mathbf{v}^{\mathrm{ss}} &= \mathbf{v}_{\mathrm{ref}} - \mathrm{T}\left(\mathbf{r}^{\mathrm{ss}}\right)\mathbf{i}^{\mathrm{ss}} + \Delta\mathbf{v}^{\mathrm{ss}} \\ &= v_{\mathrm{rated}}\underline{\mathbf{1}} - \mathrm{T}\left(\mathbf{r}_0 - \Delta\mathbf{r}^{\mathrm{ss}}\right)\mathbf{i}^{\mathrm{ss}} + \Delta\mathbf{v}^{\mathrm{ss}}.\end{aligned} \tag{3.33}$$

By substituting (3.31)-(3.32) in (3.33),

$$\begin{aligned}\mathbf{v}^{\mathrm{ss}} &= v_{\mathrm{rated}}\underline{\mathbf{1}} \\ &\quad -\mathrm{T}\left(\mathbf{r}_0 + b\left(\mathbf{G}_{\mathrm{P}} + \mathbf{G}_{\mathrm{I}}(t - t_0)\right)\mathbf{L}\mathbf{i}^{\mathrm{pu}^{\mathrm{ss}}} - \mathbf{W}_{\mathbf{r}}(t_0)\right)\mathbf{i}^{\mathrm{ss}} \\ &\quad +\left(v_{\mathrm{rated}} - \overline{v}^{\mathrm{ss}}\right)\left(\mathbf{H}_{\mathrm{P}} + \mathbf{H}_{\mathrm{I}}(t - t_0)\right)\underline{\mathbf{1}} + \mathbf{W}_{\mathbf{v}}(t_0).\end{aligned} \tag{3.34}$$

Equation (3.34) holds for all $t \geq t_0$. Thus, the time varying term in (3.34) is zero. Accordingly,

$$\left(v_{\mathrm{rated}} - \overline{v}^{\mathrm{ss}}\right)\mathbf{H}_{\mathrm{I}}\underline{\mathbf{1}} = \mathrm{T}\left(b\mathbf{G}_{\mathrm{I}}\mathbf{L}\mathbf{i}^{\mathrm{pu}^{\mathrm{ss}}}\right)\mathbf{i}^{\mathrm{ss}}. \tag{3.35}$$

One can see that if $\mathbf{G}$ is a diagonal matrix and b a real number then, for any vector $\mathbf{x}$,

$$\mathrm{T}\left(b\mathbf{G}\,\mathbf{x}\right) = b\mathbf{G}\,\mathrm{T}\left(\mathbf{x}\right). \tag{3.36}$$

The transformation property in (3.36) helps to rewrite (3.35),

$$\mathrm{T}\left(\mathbf{L}\mathbf{i}^{\mathrm{pu}^{\mathrm{ss}}}\right)\mathbf{I}_{\mathrm{rated}}\mathbf{i}^{\mathrm{pu}^{\mathrm{ss}}} = \left(v_{\mathrm{rated}} - \overline{v}^{\mathrm{ss}}\right)b^{-1}\mathbf{G}_{\mathrm{I}}^{-1}\mathbf{H}_{\mathrm{I}}\underline{\mathbf{1}}. \tag{3.37}$$

Both $\mathrm{T}(\mathbf{L}\mathbf{i}^{\mathrm{pu}^{\mathrm{ss}}})$ and $\mathbf{I}_{\mathrm{rated}}$ are diagonal matrices and, thus,

$$\mathrm{T}\left(\mathbf{L}\mathbf{i}^{\mathrm{pu}^{\mathrm{ss}}}\right)\mathbf{I}_{\mathrm{rated}} = \mathbf{I}_{\mathrm{rated}}\mathrm{T}\left(\mathbf{L}\mathbf{i}^{\mathrm{pu}^{\mathrm{ss}}}\right). \tag{3.38}$$

Accordingly,

$$\begin{aligned}\mathrm{T}\left(\mathbf{L}\mathbf{i}^{\mathrm{pu}^{\mathrm{ss}}}\right)\mathbf{i}^{\mathrm{pu}^{\mathrm{ss}}} &= \left(v_{\mathrm{rated}}-\overline{v}^{\mathrm{ss}}\right)b^{-1}\mathbf{I}_{\mathrm{rated}}^{-1}\mathbf{G}_{\mathrm{I}}^{-1}\mathbf{H}_{\mathrm{I}}\underline{\mathbf{1}}\\ &= \left(v_{\mathrm{rated}}-\overline{v}^{\mathrm{ss}}\right)\left[u_1,u_2,\cdots,u_N\right]^{\mathrm{T}}.\end{aligned} \tag{3.39}$$

where $u_i = H_i^{\mathrm{I}} / (bG_i^{\mathrm{I}} I_i^{\mathrm{rated}}) > 0$. If any of the currents is zero, e.g., $i_j^{\mathrm{pu}} = 0$, then, (3.39) implies $v_{\mathrm{rated}} = \overline{v}^{\mathrm{ss}}$. Otherwise, one can safely assume that all currents are positive (i.e., $i_i > 0$); sources only deliver power. Using (3.39),

$$\mathbf{L}\mathbf{i}^{\mathrm{pu}^{\mathrm{ss}}} = \left(v_{\mathrm{rated}}-\overline{v}^{\mathrm{ss}}\right)\left[\frac{u_1}{i_1^{\mathrm{pu}}},\frac{u_2}{i_2^{\mathrm{pu}}},\cdots,\frac{u_N}{i_N^{\mathrm{pu}}}\right]^{\mathrm{T}}. \tag{3.40}$$

with the balanced Laplacian matrix, $\mathbf{L}$,

$$\underbrace{\underline{\mathbf{1}}^{\mathrm{T}}\mathbf{L}}_{=0}\mathbf{i}^{\mathrm{pu}^{\mathrm{ss}}} = \left(v_{\mathrm{rated}}-\overline{v}^{\mathrm{ss}}\right)\underbrace{\sum_{j=1}^{N}\frac{u_j}{i_j^{\mathrm{pu}}}}_{>0}. \tag{3.41}$$

Accordingly,

$$v_{\mathrm{rated}} = \overline{v}^{\mathrm{ss}}, \tag{3.42}$$

which, equivalently, satisfies the global voltage regulation, i.e., the controller successfully regulates the average voltage of the microgrid, $\overline{v}^{\mathrm{ss}}$, at the rated value, v_{rated}.

For any vector $\mathbf{x}$ one can investigate that

$$\underline{\mathbf{1}}^{\mathrm{T}}\mathrm{T}(\mathbf{x}) = \mathbf{x}^{\mathrm{T}}. \tag{3.43}$$

Multiplying both sides of (3.39) from left by $\underline{\mathbf{1}}^{\mathrm{T}}$, one can write

$$\left(\mathbf{i}^{\mathrm{pu}^{\mathrm{ss}}}\right)^{\mathrm{T}}\mathbf{L}^{\mathrm{T}}\mathbf{i}^{\mathrm{pu}^{\mathrm{ss}}} = \left(v_{\mathrm{rated}}-\overline{v}^{\mathrm{ss}}\right)\sum_{j=1}^{N}u_j = 0, \tag{3.44}$$

which is a quadratic equation. It is shown in Appendix D that

$$\mathbf{i}^{\mathrm{pu}^{\mathrm{ss}}} = k\underline{\mathbf{1}}, \tag{3.45}$$

is the only solution to the quadratic equation in (3.44), where k is a positive real number. Equation (3.45) ensures consensus of the per-unit currents or, equivalently, achievement of proportional load sharing.

3.5. Experimental Verification

A low-voltage DC microgrid, with the structure shown in Fig. 3-1, is prototyped. Figure 3-4 shows the test bench where four adjustable isolated AC sources are used as energy sources. Each source is driven by a buck converter with an input rectifier. The converters have similar topologies but different ratings, i.e., the rated currents of the first and the fourth converters are twice those for the other two converters. Each distribution line is built using a π–circuit model. The microgrid has five consumption terminals; four to supply local loads and one to supply a remote load, as seen in Fig. 3-1. Although different voltage levels are possible [116], [117], a $48\ \mathrm{V}$ system is considered here. The typical acceptable voltage deviation is about 5% of the rated voltage [85] and, thus, the voltage limiters are set with $\varepsilon = 2.5\ \mathrm{V}$. Electrical and control parameters of the microgrid are provided in Appendix E.

Alternative communication topologies for a group of four agents are represented in Fig. 3-5, where all links are assumed bidirectional to feature a balanced Laplacian matrix. Despite carrying spanning tree, not all alternatives satisfy the communication redundancy required for the safe operation (link failure resiliency) of the proposed method. In other words, some topologies are susceptible to lose connectivity in the case of a single link failure. For example, if any of the links highlighted in red in Figs. 3-5(a) or 5(b) is lost, the corresponding graph losses its connectivity, which renders the whole control mechanism inoperable. However, the circular communication structure in Fig. 3-5(c) is the sparsest network where no single link failure can compromise the graphical connectivity. Figure 3-5(d) shows a fully connected graph, which provides a similar redundancy feature yet lacks sparsity. Therefore, the communication structure in Fig. 3-5(c) is considered for this study.

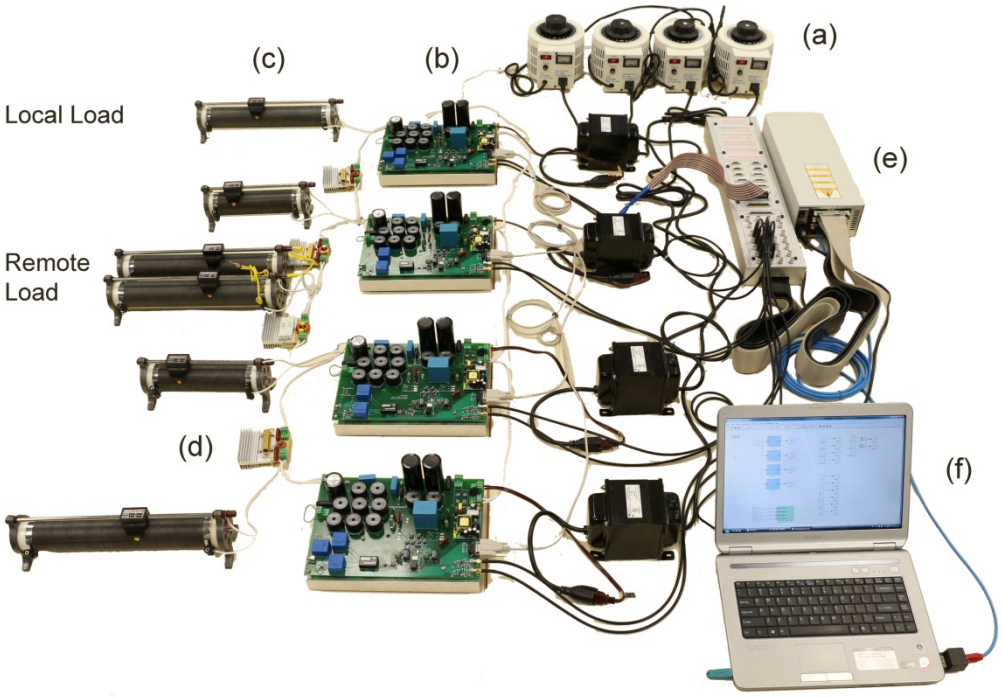

Figure 3-4 DC microgrid prototype: (a) input AC sources, (b) buck converters driving each source, (c) local and remote loads, (d) distribution line, (e) dSAPCE controller board (DS1103), (f) programming/monitoring PC.

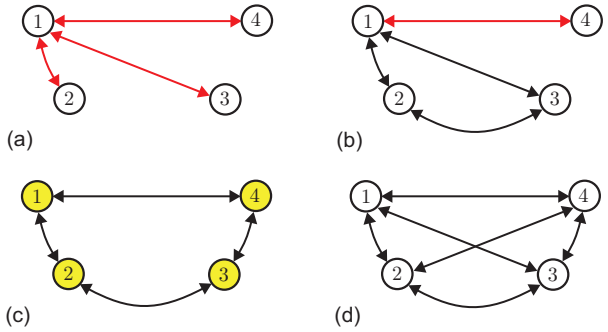

Figure 3-5 Alternative communication topologies forming a connected graph with: (a) no redundant link, (b) suboptimal link redundancy, (c) optimal link redundancy, and (d) full connection.

The communication channels are assumed ideal and are modeled in the dSAPCE. Wireless or fiber optic networks may be used for physical implementation of the data network. The effect of non-idealities such as noise, limited bandwidth, channel delay, packet drop, etc. is studied in [108]. Moreover, consensus protocols are tailored for non-ideal data networks in [118]–[120], whose application in the power distribution systems will be the subject of future studies.

The control approach is built in Simulink on a programming/monitoring PC which is linked to a dSPACE control board (DS1103). The PC compiles the Simulink model and, accordingly, programs the DS1103. It also generates a variable description file further used by the dSPACE monitoring software, ControlDesk 5.0, to provide a live view of any variable. When the proposed control methodology is in effect, the ControlDesk enables the designer to tune any control parameter online and monitor the system performance.

3.5.1. Constant Droop versus Adaptive Droop

Figure 3-6 comparatively studies the performance of the proposed methodology. The microgrid is initially controlled using the conventional droop controller, where a fixed droop impedance is used, i.e., $\mathbf{r}(t) = \mathbf{r}_0$. As seen in Fig. 3-6(a), it leads to voltages less than the desired value, i.e., $v_{\text{rated}} = 48\ \text{V}$. In addition, although the initial values of the droop gains are designed reciprocal to the converters' rated currents, the transmission line effect has clearly incapacitated the droop mechanism, resulting in a poor load sharing where converters with identical ratings supply different currents (see Fig. 3-6(b)). The proposed controller is engaged at $t = 10.1\ \text{s}$. Consequently, the voltages are boosted across the microgrid and the average voltage is finely regulated at the set point, i.e., $v_{\text{rated}} = 48\ \text{V}$.

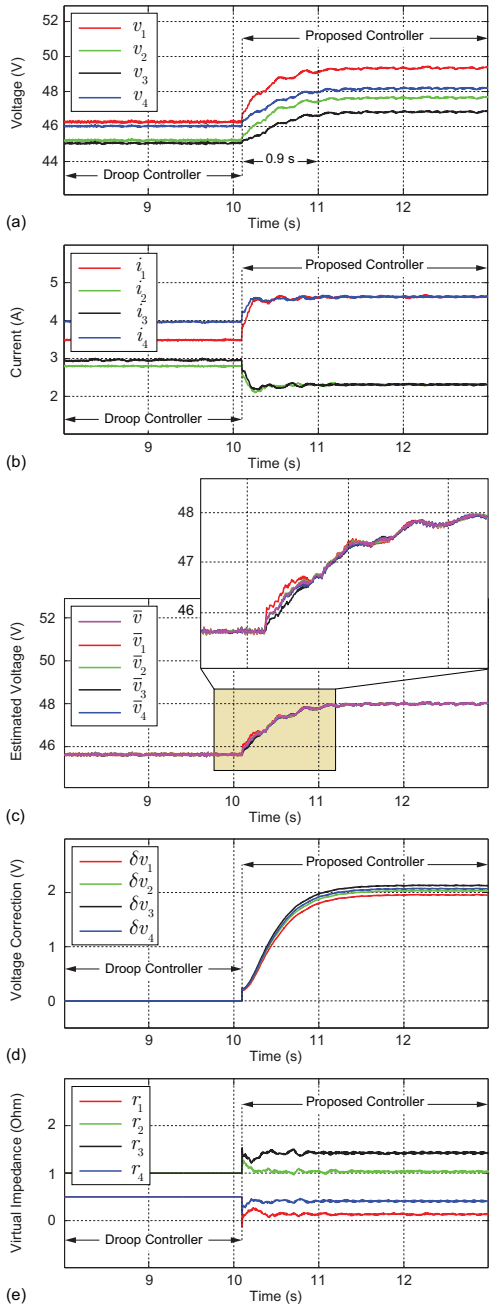

Figure 3-6 Comparative studies of the conventional droop control and the distributed adaptive-droop control: (a) terminal voltages, (b) supplied currents, (c) estimations of the average voltage, (d) voltage correction terms, (e) virtual impedances.

Figure 3-6(b) shows that the proportional load sharing is also carried out, where the first and the fourth converters carry twice the current as the other two converters. Dynamic performance of the controller can be tuned by adjusting the communication weights (or, equivalently, entries of the Adjacency matrix). In comparison with alternative solution in [109], it can be seen that the distributed adaptive droop has provided a faster load sharing; almost twice as fast as the method in [109].

The voltage observers is studied in Fig. 3-6(c), where a good agreement is reported between the true average voltage, $\overline{v}$, and the individual estimated values, $\overline{v}_i$ s. Figure 3-6(d) expresses how the proposed controller sets voltage correction terms, δv_i s, to boost the voltage across the microgrid and overcome the natural voltage drop caused by the droop mechanisms. Figure 3-6(e) shows how the current controller adjusts the virtual impedances, r_i s, to provide proportional load sharing.

3.5.2. Load Variation

The controller performance in case of load change is studied in Fig. 3-7, where the remote load at bus five, R_5, is changed in step between $10\ \Omega$ and $20\ \Omega$. Tight voltage regulation and load sharing can be observed in Figs. 3-7(a) and 3-7(b). Excellent transient load sharing is also noticeable in Fig. 3-7(b). Estimations of the average voltage across the microgrid are plotted in Fig 3-7(c) where a good agreement between the true and estimated values ($\overline{v}$ and $\overline{v}_i$ s, respectively) can be seen. Comparing Figs. 3-7(d) and 7(e), one can observe that load change mostly affects voltage correction terms, δv_i s, and has a negligible impact on the virtual impedances.

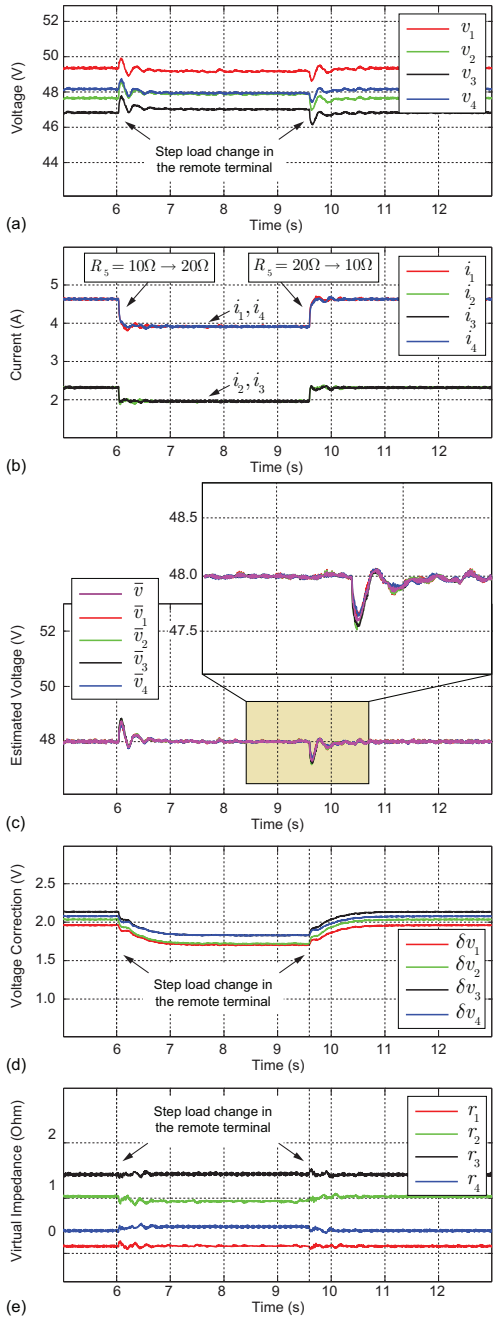

Figure 3-7 Comparative studies of the conventional droop control and the distributed adaptive-droop control: (a) terminal voltages, (b) supplied currents, (c) estimations of the average voltage, (d) voltage correction terms, (e) virtual impedances.

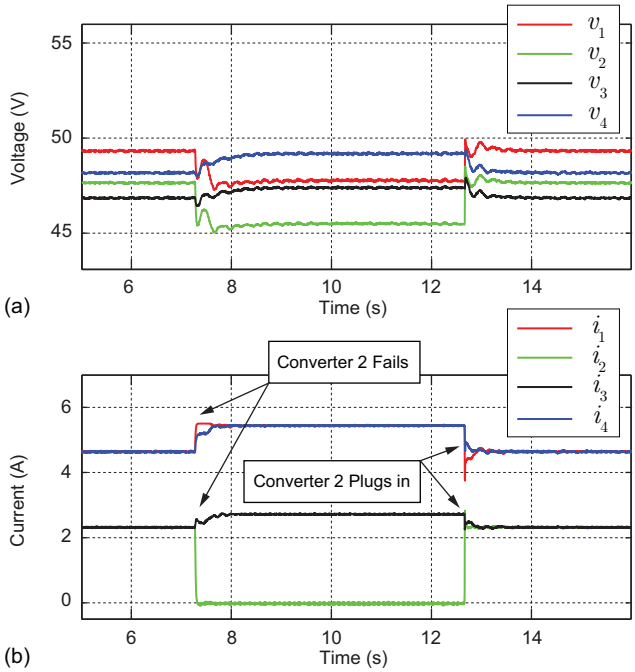

Figure 3-8 Converter failure and plug-and-play studies: (a) Terminal voltages, (b) Supplied currents.

3.5.3. Plug-and-Play Capability

Figure 3-8 studies plug-and-play capability of the proposed method and its performance in the case of a converter failure. As seen, when the second converter fails at $t = 7.3$ s, the controller adjusts the voltages to regain the global voltage regulation. When the Converter 2 fails, the voltage at the second bus, v_2, is no longer available. Thus, the controller averages the three remaining measurements, i.e., v_1, v_3, and v_4, and regulates this new average at the reference value. The controller also readjusts the load sharing among the remaining converters. It should be noted that a converter failure also implies loss of all communication links attached to that particular converter.

Accordingly, failure of the second converter automatically renders the link 1-2 (between nodes 1 and 2) and link 2-3 inoperable. However, the remaining links still form a connected graph with balanced Laplacian matrix (see Fig. 3-1, cyber layer) and, thus, the whole control system is still functional. Then, the Converter 2 is plugged back at $t = 12.6\ \mathrm{s}$. As seen, the controller has properly updated the load sharing and global voltage regulation, afterwards.

3.5.4. Link-failure Resiliency

Resiliency to a single link failure is studied next in Fig. 3-9. The original communication graph in Fig. 3-1 is designed to carry a minimal redundancy, so no single link failure can cause loss of connectivity in the graph. Thus, the control system shall remain operational. As seen in Fig. 3-9, the link 1-2 has failed at $t = 4.0\ \mathrm{s}$, but it does not have any impact on voltage regulation or load sharing. Controller response to the step load change in the remote load is also studied with the failed link, where a satisfactory performance can be seen. It should be noted that the reconfiguration caused by the link failure affects the Laplacian matrix and, thus, the whole system dynamic but not the steady-state performance.

Generally, any link failure limits information flow and can slightly slow down the transient response. Similar to Fig. 3-7(e), Fig. 3-9(d) demonstrates negligible impact of load change on the virtual impedances. However, by comparison, Fig. 3-7(e) shows more stable impedances than those of Fig. 3-9(d). This observation concludes that higher graphical connectivity results in more stable droop impedances. In addition, small variations of the virtual impedance terms in Figs. 3-7(e) and 3-9(d) implies that the developed small-signal model in Subsection 3.4.1 is appropriate for modeling and stability analysis of the proposed adaptive droop mechanism.

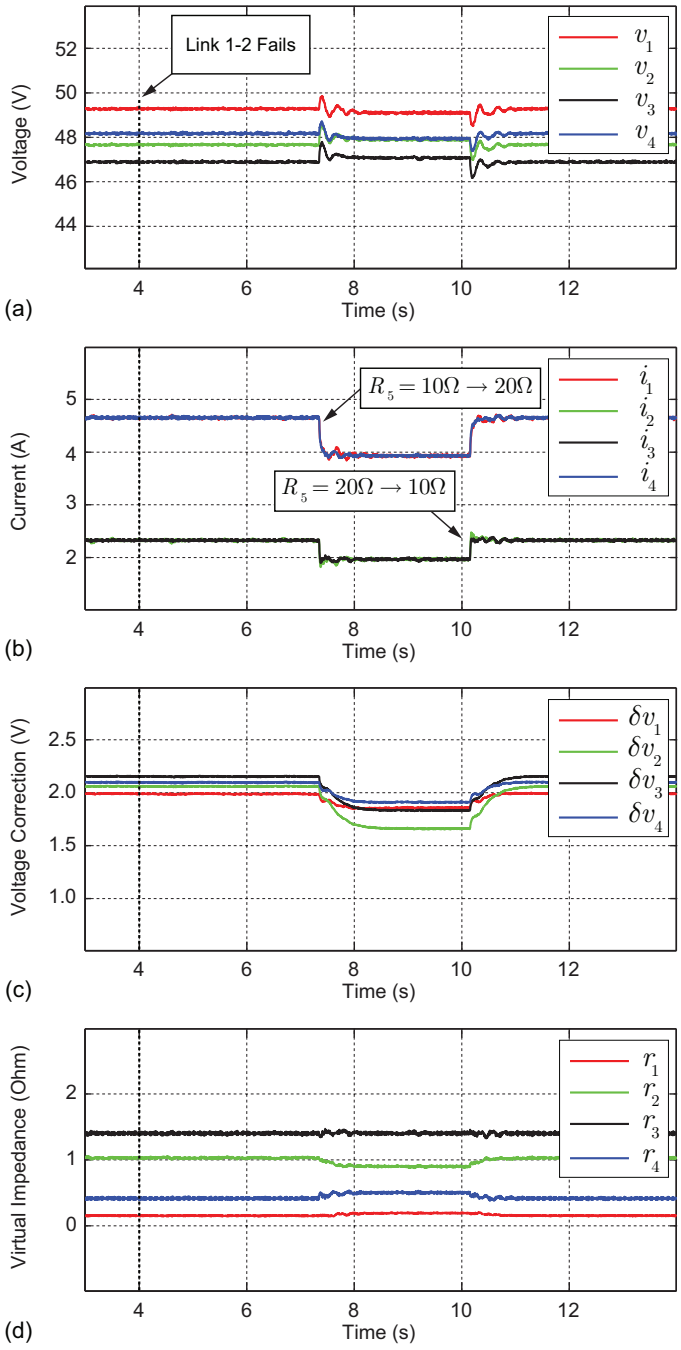

Figure 3-9 Link-failure resiliency: (a) terminal voltages, (b) supplied currents, (c) voltage correction terms, (d) virtual impedances.

3.5. Summary

An adaptive droop-based distributed secondary controller is proposed for DC microgrids. The controller on each converter comprises two modules; the voltage regulator and the current regulator. The voltage regulator uses a cooperative voltage observer to estimate the global average voltage. This estimation is then further used to boost the local voltage set point to provide global voltage regulation. The current regulator at each source compares local per-unit current with its neighbors' and, accordingly, adjusts the local virtual impedance to carry out proportional load sharing. This control paradigm uses a sparse communication network for data exchange among converters. Studies show that the proposed cooperative control provides precise global voltage regulation and proportional load sharing. Plug-and-play capability and link-failure resiliency of the control structure are also verified through experiments. It is also discussed that the droop coefficients show slight variations in response to load variations, which makes the small-signal modeling a viable approach for stability analysis of the proposed controller.

Chapter 4

Droop-free Distributed Control for AC Microgrids

Similar to DC systems, the droop mechanism, or its variations [136]–[147], is a common decentralized approach to realize the primary control, although alternative methods (e.g., virtual oscillator control [148]–[151]) are emerging. They emulate virtual inertia for AC systems and mimic the role of governors in traditional synchronous generators [152]. Despite simplicity, the droop mechanisms suffers from 1) load-dependent frequency/voltage deviation, 2) poor performance in handling nonlinear loads [153], and 3) poor reactive power sharing in presence of unequal bus voltages [154]. Unequal bus voltages are indispensible in practical systems to perform the scheduled reactive power flow. Droop techniques cause voltage and frequency deviations and, thus, a supervisory secondary control is inevitable to update the set points of the local primary controls [155]–[160]. For example, GPS-coordinated time referencing handles frequency synchronization across the microgrid in [153], [158], [159]. Such architecture requires two-way high bandwidth communication links between the central controller and each inverter. This protocol adversely affects the system reliability as failure of any communication link hinders the functionality of the central controller and, thus, the entire microgrid. The central controller itself is also a reliability risk since it imposes a single point-of-failure. Scalability is another issue for that it adds to the complexity of the communication network and it requires updating the settings of the central controller.

Spatially dispersed inverter-based microgrids naturally lend themselves to distributed control techniques to address their synchronization and coordination requirements. Distributed control architectures can discharge duties of a central controller while being resilient to faults or unknown system parameters. Distributed synchronization processes necessitate that each agent (i.e., the inverter) exchange information with other

agents according to some restricted communication protocol [125], [161], [162]. These controllers can use a sparse communication network and have less computational complexity at each inverter controller [163]. Networked control of parallel inverters in [164], [165] embeds the functionality of the secondary control in all inverters, i.e., it requires a fully connected communication network. The master node in the networked master-slave methods [166]–[168] is still a single point-of-failure. Distributed cooperative control is recently introduced for AC [169]–[171] and DC microgrids [172]–[175]. Distributed control of AC microgrids are also discussed in [176]–[178] (using a ratio-consensus algorithm), [170] (a multi-objective approach), and [179]-[182] (using a distributed averaging proportional controller). Majority of such approaches are still based on the droop mechanism (and, thus, inherit its shortcoming), require system information (e.g., number of inverters, inverter parameters, and total load demand), require frequency measurement, and mainly handle active power sharing and frequency regulation (or, only reactive power sharing/voltage control). Recent works of the authors in [170] and [171] investigate distribution networks with negligible line impedances and, potentially, can lack satisfactory performance in practical multi-terminal distribution systems with intricate and lossy transmission networks. They also assign a single source as leader, who relays the rated frequency and voltage set points to other sources through a communication network. Moreover, such solutions focus on the islanded mode of operation and their extension to grid-connected mode is not straightforward.

This chapter provides a comprehensive distributed cooperative solution that satisfies both the secondary and the primary control objectives for an autonomous AC microgrid without relying on the droop mechanism. Herein, each inverter is considered as an agent of a multi-agent system (i.e., the microgrid); each inverter exchanges data with a few other neighbor inverters and processes the information to update its local voltage

set points and synchronize their normalized power and frequencies. The proposed controller includes three modules: voltage regulator, reactive power regulator, and active power regulator. The salient features of the proposed control method are:

- Cooperation among inverters on a communication graph provides two voltage correction terms to be added to the rated voltage and adjust the local voltage set points of individual inverters.
- Cooperation among voltage, reactive power, and active power regulators effectively carries out global voltage regulation, frequency synchronization, and proportional load sharing, particularly, in practical networks where the transmission/ distribution line impedances are not negligible.
- Normally, the controllers share the total load among sources in proportion to their rated active and reactive powers; however, the rated values, embedded in the controller, can be manipulated to achieve any desired load sharing.
- The voltage regulator seeks to adjust the average voltage across the microgrid, rather than the individual inverter busses, at the rated voltage value, and ensures global voltage regulation without the need to run a power flow analysis.
- The control method does not employ any droop mechanism and does not require any frequency measurement.
- The proposed scheme does not require prior knowledge of system parameters or the number of inverters. Thus, it features scalability, modularity, robustness (independent of loads), and plug-and-play capability.
- Only a sparse communication graph is sufficient for the limited message passing among inverters. This is in direct contrast with the centralized control approaches that require high-bandwidth bidirectional communication networks,

or existing networked control techniques that require fully-connected communication graphs.

4.1. Proposed Cooperative Control Framework

4.1.1. Link-failure Resiliency

A distribution network is an electric network that provides the physical connection between sources and loads within a microgrid. Such a physical system can be equipped with a cyber network to exploit different control opportunities. Interaction of the sources (i.e., inverter-augmented DC sources) in the cyber domain offers cooperative decision making, which features scalability and improves reliability. Here, a microgrid is assumed to be cyber-physical system with a communication network that facilitates data exchange among sources for control and monitoring purposes. Figure 4-1(a) illustrates physical and cyber layers of the microgrid. Each source broadcasts its information, e.g., voltage and power measurements, to a few selected sources, called its *neighbors*. As oppose to the centralized/supervisory control, this communication layout forms a sparse network; not all sources need to communicate.

From the control perspective, a multi-agent cyber-physical system can be expressed with a graphical representation with active agents (sources) modeled as nodes of the graph and communication links mapped to edges connecting nodes (see Fig. 4-1(b)). Communication links may not be reciprocal, forming a directed graph (digraph). Each node and edge inherit the dynamic model of the corresponding agent and communication channel, respectively. Information links may exchange data with different gains referred to as the *communication weights*.

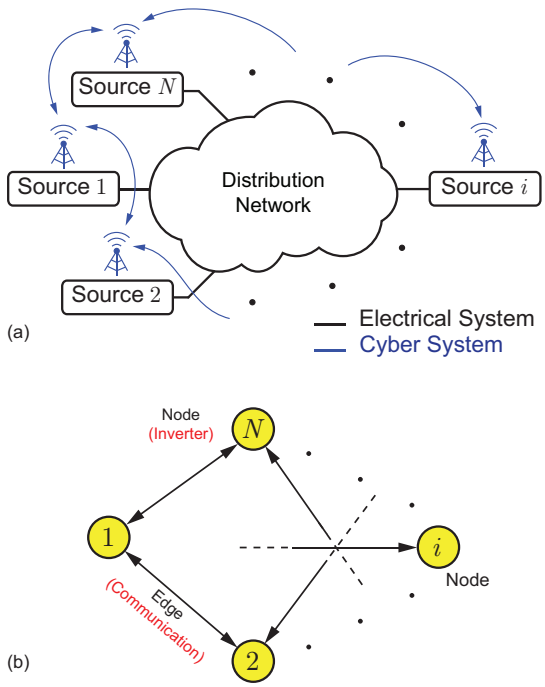

Figure 4-1 General layout of an AC microgrid: (a) sources supplying the grid with communication infrastructure spanned across the grid, (b) graphical representation of the cyber-physical system.

For example, if Node j broadcasts data x_j to Node i through a link with designated a weight of $a_{ij} > 0$, then, the information received at node i is $a_{ij}x_j$. Generally, $a_{ij} > 0$ if Node i receives data from Node j and $a_{ij} = 0$, otherwise. Such a graph is usually represented by an associated adjacency matrix $\mathbf{A}_\mathbf{G} = \left[a_{ij}\right] \in \mathbb{R}^{N\times N}$ that carries the communication weights, where N is the number of dispatchable sources. Communication weights can be time varying and may include some channel delay; however, this study assumes time-invariant and scalar adjacency matrix. N_i denotes the

set of all neighbors of Node i. The in-degree and out-degree matrices $\mathbf{D}^{\text{in}} = \text{diag}\left\{d_i^{\text{in}}\right\}$ and $\mathbf{D}^{\text{out}} = \text{diag}\left\{d_i^{\text{out}}\right\}$ are diagonal matrices with $d_i^{\text{in}} = \sum_{j \in N_i} a_{ij}$ and $d_i^{\text{out}} = \sum_{i \in N_j} a_{ji}$, respectively. The Laplacian matrix is defined as $\mathbf{L} \triangleq \mathbf{D}^{\text{in}} - \mathbf{A}_{\mathbf{G}}$, whose eigenvalues determine the global dynamics of the entire system (i.e., the microgrid) [183], [184]. The Laplacian matrix is balanced if the in-degree and out-degree matrices are equal; particularly, an undirected (bidirectional) data network satisfies this requirement. A direct path from Node i to Node j is a sequence of edges that connects the two nodes. A digraph is said to have a spanning tree if it contains a root node, from which, there exists at least a direct path to every other node. Here, a graph is called to carry the *minimum redundancy* if it contains enough redundant links that, in the case of any single link failure, it remains connected and presents a balanced Laplacian matrix.

4.1.2. Proposed Cooperation Policy

The proposed method requires a communication graph with the adjacency matrix $\mathbf{A}_{\mathbf{G}} = \left[a_{ij}\right] \in \mathbb{R}^{N \times N}$ that 1) has at least a spanning tree, 2) can be undirected or directional, yet with a balanced Laplacian matrix, and 3) the graph must carry the minimum redundancy. Communication weights, a_{ij}, are design parameters. Each source exchanges a vector of information, $\Psi_i = \left[\overline{e}_i, p_i^{\text{norm}}, q_i^{\text{norm}}\right]$, with its neighbor sources on the communication graph, where $\overline{e}_i$ is the estimation of the averaged voltage magnitude across the microgrid, processed at Node i. $p_i^{\text{norm}} \triangleq p_i \big/ p_i^{\text{rated}}$ and $q_i^{\text{norm}} \triangleq q_i \big/ q_i^{\text{rated}}$ are the normalized active and reactive powers supplied by Source i. p_i and q_i are the measured active and reactive powers supplied by Source i, respectively, and p_i^{rated} and

q_i^{rated} are the rated active and reactive powers of the same source. The control strategy attempts to share the load among sources in proportion to their rated powers.

Objectives of the secondary/primary controller are 1) global voltage regulation, 2) frequency synchronization, 3) active power sharing, and 4) reactive power sharing. Generally, fine adjustment of the voltage magnitude and frequency can satisfy all four objectives. Particularly, active and reactive power flow can be managed by tuning the frequency and voltage magnitude, respectively. The proposed control method is established on this notion. Figure 4-2 shows the schematic of the control policy for Node i (Source i). The controller consists of three separate modules: the voltage regulator, reactive power regulator, and active power regulator.

The controller at Node i receives its neighbors' information, Ψ_js, and processes the neighbors' and local data, Ψ_i, to update its voltage set point. e_i^* and ω_i^* are the set points of the (line to neutral) voltage magnitude (rms value) and frequency, respectively. Accordingly, the Space Vector PWM module generates the actual voltage set point, v_i^*,

$$v_i^*(t) = e_i^*(t)\sqrt{2}\sin\left(\int_0^t \omega_i^*(\tau)\mathrm{d}\tau\right), \tag{4.1}$$

and assigns appropriate switching signals to drive the inverter module [185]. It should be noted that the controller is assumed activated at $t=0$. As seen in Fig. 4-2, each inverter is followed by an LCL filter to attenuate undesired (switching and line-frequency) harmonics. The set point in (4.1) is the reference voltage for the output terminal of the filtering module or, equivalently, the microgrid bus that corresponds to Source i.

The voltage and reactive power regulators adjust the set point of the voltage magnitude by producing two voltage correction terms, δe_i^1 and δe_i^2, respectively, as

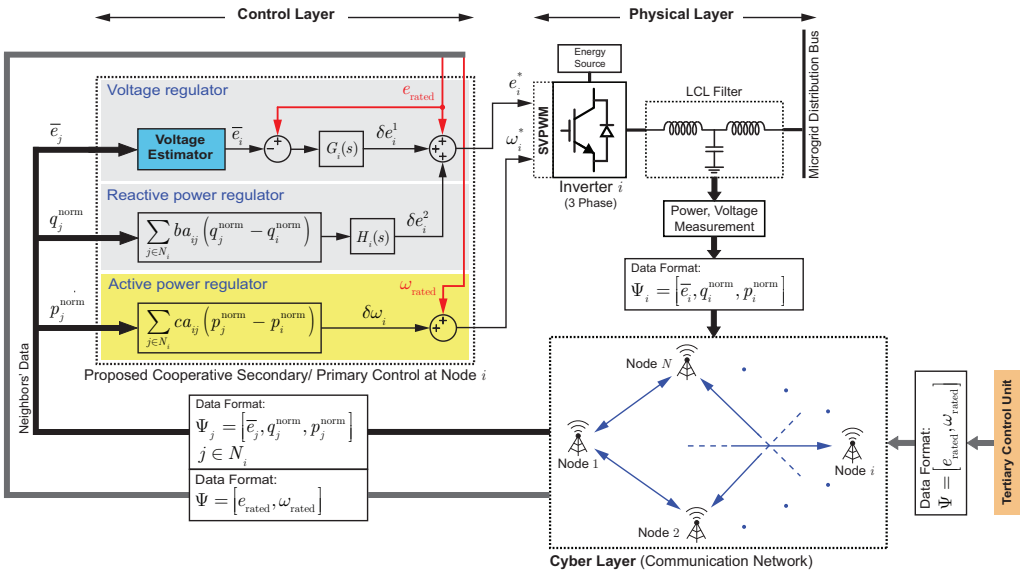

Figure 4-2 Proposed cooperative secondary control for the Source i, of the AC microgrid. Note data exchange with the neighbor nodes.

$$e_i^*(t) = e_{\text{rated}} + \delta e_i^1(t) + \delta e_i^2(t), \tag{4.2}$$

where e_{rated} is the rated voltage magnitude of the microgrid. Regardless of the operating mode, i.e., islanded or grid-connected modes, the rated voltage can be safely assumed equal for all active nodes (dispatchable sources). The voltage regulator at Node i includes an estimator that finds the global averaged voltage magnitude, i.e., the averaged voltage across the microgrid. This estimation is, then, compared with the rated voltage, e_{rated}, and the difference is fed to a PI controller, G_i, to generate the first voltage correction term, δe_i^1, and, thus, handle global voltage regulation. Accordingly, the voltage regulators collectively adjust the average voltage of the microgrid on the rated value, yet individual bus voltages may slightly deviate from the rated value (typically, less than 5%). This deviation is essential in practice to navigate reactive power across the microgrid.

Therefore, the reactive power regulator at Node i adjusts an additional (i.e., the second) voltage correction term, δe_i^2, to control the supplied reactive power. This module calculates the neighborhood reactive loading mismatch, mq_i,

$$mq_i = \sum_{j \in N_i} ba_{ij}(q_j^{\text{norm}} - q_i^{\text{norm}}), \tag{4.3}$$

which measures how far is the normalized reactive power of the Source i from the average of its neighbors'. The coupling gain b is a design parameter. The mismatch in (4.3) is then fed to a PI controller, H_i, (see Fig. 4-2) to adjust the second voltage correction term, δe_i^2, and, accordingly, mitigate the mismatch. Performance analysis in Subsection 4.2.5 will show that all the mismatch terms, in the steady state, converge to zero and, thus, all normalized reactive powers would synchronize. This satisfies the proportional reactive power sharing among sources.

The active power regulator at Source i controls its frequency and active power. This module calculates the neighborhood active loading mismatch to assign the frequency correction term, $\delta\omega_i$,

$$\delta\omega_i = \sum_{j \in N_i} ca_{ij}(p_j^{\text{norm}} - p_i^{\text{norm}}), \tag{4.4}$$

where the coupling gain c is a design parameter. As seen in Fig. 4-2, this correction term is added to the rated frequency, ω_{rated},

$$\omega_i^*(t) = \omega_{\text{rated}} + \delta\omega_i(t), \tag{4.5}$$

and, thus, (4.1) can be written as

$$v_i^*(t) = e_i^*(t)\sqrt{2}\sin\left(\omega_{\text{rated}}t + \int_0^t \delta\omega_i \mathrm{d}\tau\right). \tag{4.6}$$

Equation (4.6) helps to define the phase angle set point for Source i,

$$\delta_i^*(t) \triangleq c\int_0^t \sum_{j\in N_i} a_{ij}(p_j^{\text{norm}} - p_i^{\text{norm}})\,\mathrm{d}\tau. \tag{4.7}$$

According to (4.6)–(4.7), the active power regulator module keeps the frequency at the rated value and fine tunes the phase angle set point, δ_i^*, to reroute the active power across the microgrid and mitigate the neighborhood active loading mismatch. It is shown in Subsection 4.2.5 that all phase angles, δ_i^*, will converge to their steady-state values and, thus, all frequency correction terms, $\delta\omega_i$, decay to zero. Therefore, the microgrid frequency synchronizes to the rated frequency, ω_{rated}, without any frequency measurement loop, while the controller stabilizes the phase angles, δ_i. Indeed, transient variations in the inverter frequency adjust its phase angle and control the active power flow; the frequency will not deviate from the rated value in the steady state and normalized active powers will synchronize, which provides the proportional active load sharing.

The proposed controller is a general solution that can handle load sharing for variety of distribution systems; i.e., predominantly inductive, inductive-resistive, or primarily resistive networks. Indeed, the nature of the line impedances defines the role of the active and reactive power regulators (see Fig. 4-2) for load sharing. In particular, a predominantly inductive network naturally decouples the load sharing process; the reactive power regulator must handle the reactive load sharing by adjusting voltage magnitude while the active power regulator would handle the active load sharing through adjusting the frequency (or, equivalently, the phase angle). However, for other types of distribution network, active and reactive power flows are entangled to both voltage and phase angle adjustment.

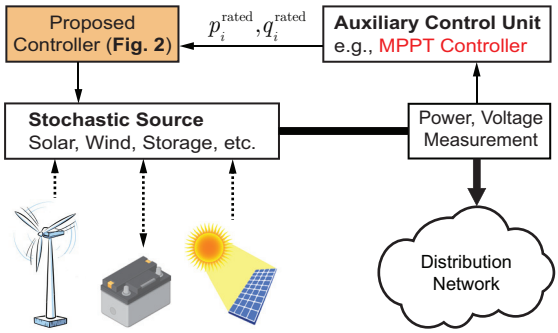

Figure 4-3 Extension of the proposed controller to non-dispatchable (e.g., stochastic) energy sources.

For such cases, the load sharing is a collaborative task where the two regulators (i.e., both the active and reactive power regulators) would work together to generate the desired set points.

The proposed controller, so far, assumes fixed and known power rating for dispatchable sources. In a scenario that some sources are non-dispatchable, i.e., renewable energy sources with stochastic power output, the proposed controller can be augmented with the methodology shown in Fig. 4-3. Supplied power by each stochastic source is measured and reported to an auxiliary control unit. This module runs optimization scenarios, e.g., Maximum Power Point Tracking (MPPT), to decide the desired operating points. It also compares the desired generation with the actual supplied power and updates the rated powers, p_i^{rated} and q_i^{rated}, to address any mismatch. The proposed control routine in Fig. 4-2 uses the tuned rated powers to adjust the voltage and frequency set points. With the modification in Fig. 4-3, the stochastic sources will be pushed to exploit their potentials (e.g., to produce maximum power) while the controller in Fig. 4-2 proportionally shares the remaining load demand among dispatchable sources.

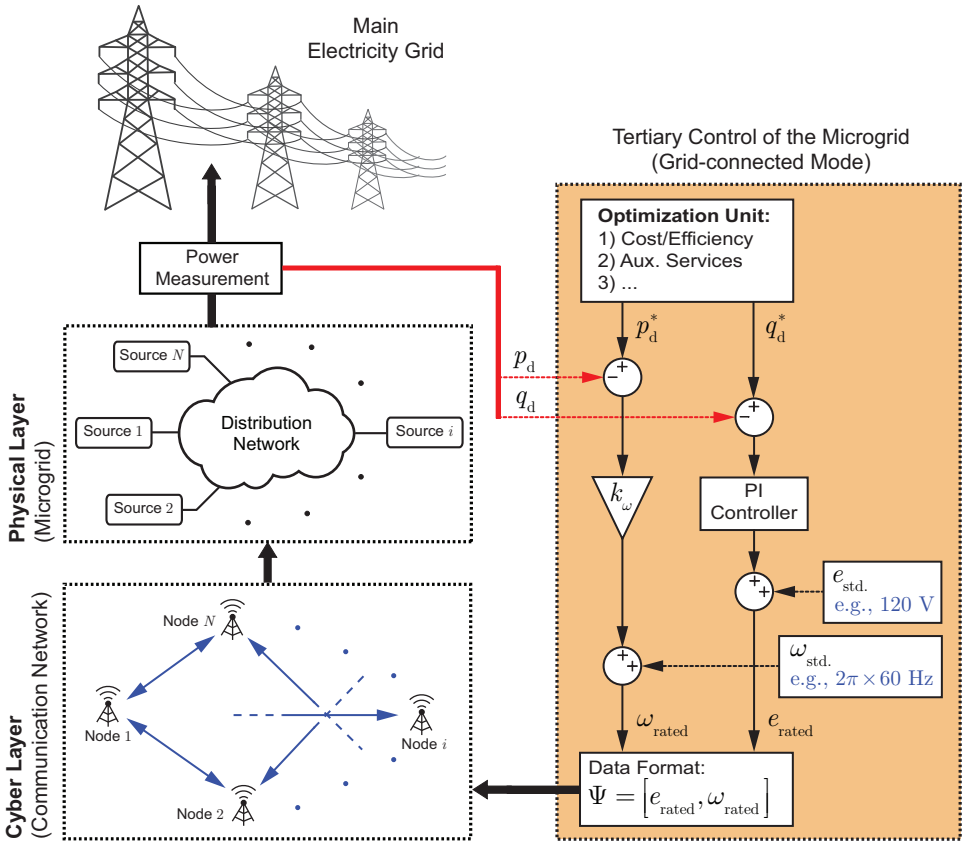

Figure 4-4 Functionality of the tertiary controller in the grid-connected mode.

In the islanded mode, the system operational autonomy requires preset (fixed) values for the rated voltage magnitude and frequency, e_{rated} and ω_{rated}, in all controllers. The voltage and frequency settings typically follow the standard ratings of the nearby electricity grid. To further extend operational range of the proposed controller to the grid-connected mode, one can consider adjustable voltage magnitude and frequency ratings. To this end, a tertiary controller (highlighted in Fig. 4-2) fine-tunes such ratings. There is a single tertiary controller for the entire microgrid, and it uses the same communication network as the secondary controllers, to propagate updated voltage and frequency

ratings to all secondary controllers across the microgrid. Functionality of the tertiary controller is elaborated in Fig. 4-4. The tertiary control unit runs cost/efficiency optimization to determine the desired active and reactive powers to be exchanges between the microgrid and the main grid, p_{d}^{*} and q_{d}^{*}, respectively. The optimization scenarios can also account for auxiliary services such as frequency regulation or reactive power support. It is noteworthy that the power flow between the microgrid and the main grid can be bidirectional and, thus, the desired powers p_{d}^{*} and q_{d}^{*} can be either positive or negative. The controller compares the actual powers supplied to the main grid, p_{d} and q_{d}, with the desired values and, accordingly, updates voltage and frequency ratings sent to the secondary controllers. The steady-state rated voltage assignment, e_{rated}, may have slight deviation from the standard value, however, the steady-state value of the rated frequency, ω_{rated}, will always converge to the standard value (e.g., $60\ \mathrm{Hz}$ in the North America). In fact, it is the transient variations in the rated frequency that adjusts the phase angles across the microgrid and manages the active power flow.

4.1.3. Voltage Estimation Policy

Each node has an estimation module that develops the estimation of the averaged voltage magnitude across the microgrid, e.g., $\overline{e}_i$, for Node i, and exchanges this estimation with its neighbors. The voltage estimation policy is demonstrated in Fig. 4-5. Accordingly, the estimator at Node i updates its own output, $\overline{e}_i$, by processing the neighbors' estimates, $\overline{e}_j$s ($j \in N_i$), and the local voltage measurement, e_i ,

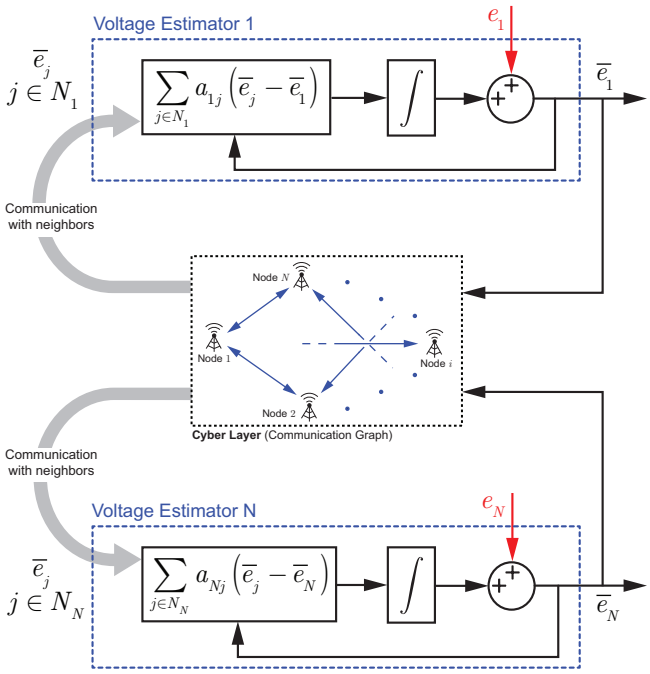

Figure 4-5 Voltage averaging policy at each node; dynamic consensus protocol.

$$\overline{e}_i(t) = e_i(t) + \int_0^t \sum_{j\in N_i} a_{ij}\left(\overline{e}_j(\tau) - \overline{e}_i(\tau)\right)\mathrm{d}\tau. \tag{4.8}$$

This updating policy is commonly referred to as the *dynamic consensus protocol* in the literature [186]. As seen in (4.8), the local measurement, e.g., e_i, is directly fed into the estimation protocol. Thus, in case of any voltage variation at Node i, the local estimate, $\overline{e}_i$, immediately responds. The change in $\overline{e}_i$ propagates through the communication network and affects all other estimations. Assume that $\mathbf{e} = [e_1, e_2, ..., e_N]^{\mathrm{T}}$ and $\overline{\mathbf{e}} = [\overline{e}_1, \overline{e}_2, ..., \overline{e}_N]^{\mathrm{T}}$ are the measured voltage and the estimated average voltage vectors, respectively. $\mathbf{E}$ and $\overline{\mathbf{E}}$ are the Laplace transforms of $\mathbf{e}$ and $\overline{\mathbf{e}}$, respectively. Accordingly, global dynamic response of the estimation policy is formulated in [173] as

$$\bar{\bar{\mathbf{E}}} = s(s\mathbf{I}_N + \mathbf{L})^{-1}\mathbf{E} = \mathbf{H}_{\text{est}}\mathbf{E}, \tag{4.9}$$

where $\mathbf{I}_N \in \mathbb{R}^{N\times N}$, $\mathbf{L}$, and $\mathbf{H}_{\text{est}}$ are the identity, Laplacian, and the estimator transfer-function matrices, respectively. It is shown in [173] that if the communication graph has a spanning tree with a balanced Laplacian matrix, $\mathbf{L}$, then, all elements of $\bar{\mathbf{e}}$ converge to a consensus value, which is the true average voltage, i.e., the average of all elements in $\mathbf{e}$. Equivalently,

$$\bar{\mathbf{e}}^{\text{ss}} = \mathbf{M}\mathbf{e}^{\text{ss}} = \left\langle \mathbf{e}^{\text{ss}} \right\rangle \underline{\mathbf{1}}, \tag{4.10}$$

where $\mathbf{M} \in \mathbb{R}^{N\times N}$ is the averaging matrix, whose elements are all $1/N$. $\mathbf{x}^{\text{ss}}$ expresses the steady-state value of the vector $\mathbf{x} \in \mathbb{R}^{N\times 1}$. $\langle \mathbf{x} \rangle$ is a scalar that represents the average of all elements in the vector $\mathbf{x}$. $\underline{\mathbf{1}} \in \mathbb{R}^{N\times 1}$ is a column vector whose elements are all one.

4.2. System-level Modeling

System-level modeling studies the dynamic/static response of the entire microgrid with the proposed controller in effect. The system under study encompasses interactive cyber and physical subsystems. The communication graph topology defies the interaction among controllers, functionality of the controllers determines output characteristics of the sources, and, finally, the transmission/distribution network rules the physical interaction among sources (and loads). Thus, the system-level study involves in mathematical modeling of each of the subsystems and establishment of mathematical coupling between the interactive subsystems.

4.2.1. Distribution Network Model

Dispatchable sources, transmission network, and loads form the physical layer of the microgrid. This layer is shown in Fig. 4-1(a), where sources are considered as controllable voltage source inverters. The proposed controller determines the voltage set

pints (both magnitude, e_i^*, and phase, δ_i^*) for each source (i.e., inverter) by processing the supplied active and reactive powers. Such controller acts on the physical layer, which is a multi-input/multi-output plant with the voltage set points as the inputs and the supplied active and reactive powers as the outputs. Herein, we express the output variables, i.e., the supplied powers, in terms of the input variables, i.e., the voltage set points.

Figure 4-1(a) helps to formulate the supplied current of each source. By formulating the supplied current by Source i,

$$I_i = Y_{ii}V_i + \sum_{j=1(\neq i)}^{N} Y_{ij}(V_i - V_j), \tag{4.11}$$

where I_i and V_i are the phasor representation of the supplied current and phase voltage of the Source i, respectively. Y_{ii} and Y_{ij} are the local load admittance at Bus i (Source i) and the admittance of the transmission line connecting busses i and j, respectively. With no loss of generality, the distribution network is assumed reduced (i.e., by using Kron reduction) such that all non-generating busses are removed from the network. Thus, the complex power delivered by the Source i is,

$$s_i = 3V_iI_i^* = 3\left|V_i\right|^2 \sum_{j=1}^{N} Y_{ij}^* - 3\sum_{j=1(\neq i)}^{N} V_iV_j^*Y_{ij}^*. \tag{4.12}$$

Assume $V_i = e_i\angle\delta_i$ and $Y_{ij} = y_{ij}\angle\theta_{ij}$ where e_i, y_{ij}, δ_i, and θ_{ij} are the magnitude of V_i, magnitude of Y_{ij}, phase of V_i, and phase of Y_{ij}, respectively. $Y_{ij} = g_{ij} + jb_{ij}$ is the rectangular representation of the admittance Y_{ij}. One can use (4.12) to derive the active and reactive powers delivered by the Source i (p_i and q_i, respectively),

$$p_i = 3e_i^2 \sum_{j=1}^{N} g_{ij} - 3 \sum_{j=1(\neq i)}^{N} e_i e_j y_{ij} \cos(\delta_i - \delta_j - \theta_{ij}), \tag{4.13}$$

$$q_i = -3e_i^2 \sum_{j=1}^{N} b_{ij} - 3 \sum_{j=1(\neq i)}^{N} e_i e_j y_{ij} \sin(\delta_i - \delta_j - \theta_{ij}), \tag{4.14}$$

The secondary control typically acts slower than the dynamic of the power network (microgrid), as its objectives are voltage and power regulation in the steady state. Accordingly, one can safely neglect the fast dynamic transient responses of the microgrid and use the phasor analysis in (4.13)–(4.14) to model the power flow. Equations (4.13)–(4.14) express nonlinear relationships between the voltages and supplied powers. In time domain, any variable x can be represented as $x = x^{\mathrm{q}} + \hat{x}$ where x^{q} and $\hat{x}$ are the quiescent and small-signal perturbation parts, respectively. Thus, one can write,

$$\begin{aligned} p_i &= p_i^{\mathrm{q}} + \hat{p}_i = p_i^{\mathrm{q}} + \sum_{j=1}^{N} \frac{\partial p_i}{\partial e_j} \hat{e}_j + \sum_{j=1}^{N} \frac{\partial p_i}{\partial \delta_j} \hat{\delta}_j \\ &\Rightarrow \hat{p}_i = \sum_{j=1}^{N} k_{e,ij}^{p} \hat{e}_j + \sum_{j=1}^{N} k_{\delta,ij}^{p} \hat{\delta}_j \end{aligned} \tag{4.15}$$

$$\begin{aligned} q_i &= q_i^{\mathrm{q}} + \hat{q}_i = q_i^{\mathrm{q}} + \sum_{j=1}^{N} \frac{\partial q_i}{\partial e_j} \hat{e}_j + \sum_{j=1}^{N} \frac{\partial q_i}{\partial \delta_j} \hat{\delta}_j \\ &\Rightarrow \hat{q}_i = \sum_{j=1}^{N} k_{e,ij}^{q} \hat{e}_j + \sum_{j=1}^{N} k_{\delta,ij}^{q} \hat{\delta}_j \end{aligned} \tag{4.16}$$

where the coefficients in (4.15)–(4.16) are formulated,

$$k_{e,ii}^{p} = \frac{p_i^{\mathrm{q}}}{e_i^{\mathrm{q}}} + 3e_i^{\mathrm{q}} \sum_{j=1}^{N} g_{ij}, \tag{4.17}$$

$$k_{e,ij}^{p} = -3e_i^{\mathrm{q}} y_{ij} \cos(\delta_i^{\mathrm{q}} - \delta_j^{\mathrm{q}} - \theta_{ij}), \quad j \neq i \tag{4.18}$$

$$k_{\delta,ii}^{p} = 3 \sum_{j=1(\neq i)}^{N} e_i^{\mathrm{q}} e_j^{\mathrm{q}} y_{ij} \sin(\delta_i^{\mathrm{q}} - \delta_j^{\mathrm{q}} - \theta_{ij}) = -q_i^{\mathrm{q}} - 3e_i^2 \sum_{j=1}^{N} b_{ij}, \tag{4.19}$$

$$k_{\delta,ij}^{p} = -3e_i^{\mathrm{q}} e_j^{\mathrm{q}} y_{ij} \sin(\delta_i^{\mathrm{q}} - \delta_j^{\mathrm{q}} - \theta_{ij}), \quad j \neq i \tag{4.20}$$

$$k_{e,ii}^{q} = \frac{q_i^{\mathrm{q}}}{e_i^{\mathrm{q}}} - 3e_i^{\mathrm{q}} \sum_{j=1}^{N} b_{ij}, \tag{4.21}$$

$$k_{e,ij}^{q} = -3e_i^{\mathrm{q}} y_{ij} \sin(\delta_i^{\mathrm{q}} - \delta_j^{\mathrm{q}} - \theta_{ij}), \quad j \neq i \tag{4.22}$$

$$k_{\delta,ii}^{q} = -3 \sum_{j=1(\neq i)}^{N} e_i^{\mathrm{q}} e_j^{\mathrm{q}} y_{ij} \cos(\delta_i^{\mathrm{q}} - \delta_j^{\mathrm{q}} - \theta_{ij}) = p_i^{\mathrm{q}} - 3e_i^{2} \sum_{j=1}^{N} g_{ij}, \tag{4.23}$$

$$k_{\delta,ij}^{q} = 3e_i^{\mathrm{q}} e_j^{\mathrm{q}} y_{ij} \cos(\delta_i^{\mathrm{q}} - \delta_j^{\mathrm{q}} - \theta_{ij}), \quad j \neq i. \tag{4.24}$$

Equations (4.15)–(4.24) explain how a disturbance in any of the voltage magnitudes, $\hat{e}_i$ s, or phases, $\hat{\delta}_i$ s, affects the power flow in the entire microgrid. These equations can be represented in the matrix format,

$$\hat{\mathbf{p}} = \mathbf{k}_e^{p} \hat{\mathbf{e}} + \mathbf{k}_\delta^{p} \hat{\boldsymbol{\delta}} \tag{4.25}$$

$$\hat{\mathbf{q}} = \mathbf{k}_e^{q} \hat{\mathbf{e}} + \mathbf{k}_\delta^{q} \hat{\boldsymbol{\delta}} \tag{4.26}$$

where $\hat{\mathbf{p}} = \left[\hat{p}_1, \hat{p}_2, ..., \hat{p}_N\right]^{\mathrm{T}}$, $\hat{\mathbf{q}} = \left[\hat{q}_1, \hat{q}_2, ..., \hat{q}_N\right]^{\mathrm{T}}$, $\hat{\mathbf{e}} = \left[\hat{e}_1, \hat{e}_2, ..., \hat{e}_N\right]^{\mathrm{T}}$, and $\hat{\boldsymbol{\delta}} = \left[\hat{\delta}_1, \hat{\delta}_2, ..., \hat{\delta}_N\right]^{\mathrm{T}}$ are column vectors carrying small-signal portions of the active powers, reactive powers, voltage magnitudes, and voltage phases, respectively. $\mathbf{k}_e^{p} = [k_{e,ij}^{p}]$, $\mathbf{k}_\delta^{p} = [k_{\delta,ij}^{p}]$, $\mathbf{k}_e^{q} = [k_{e,ij}^{q}]$, and $\mathbf{k}_\delta^{q} = [k_{\delta,ij}^{q}]$ are all matrices in $\mathbb{R}^{N \times N}$ that contain coefficients in (4.17)–(4.24). $\mathbf{k}_\delta^{p}$ and $\mathbf{k}_e^{q}$ are referred to here as the $p-\delta$ and $q-e$ transfer matrices, respectively.

4.2.2. Dynamic Model of the Control and Cyber Subsystems

The cyber domain is where the controllers exchange measurements, process information and, update the voltage set points. Interactions and functionality of the controllers are shown in Fig. 4-2. One can see how the voltage and reactive power regulators cooperate to adjust the voltage magnitude set points, e_i^{*}. In the frequency domain,

$$G_i(s)\left(E_{\text{rated}} - \bar{E}_i\right) = \Delta E_i^1, \tag{4.27}$$

$$H_i(s)\left(\sum_{j\in N_i} ba_{ij}(Q_j^{\text{norm}} - Q_i^{\text{norm}})\right) = \Delta E_i^2, \tag{4.28}$$

$$E_{\text{rated}} + \Delta E_i^1 + \Delta E_i^2 = E_i^*, \tag{4.29}$$

where E_{rated}, $\bar{E}_i$, ΔE_i^1, Q_i^{norm}, ΔE_i^2, and E_i^* are the Laplace transforms of e_{rated}, $\overline{e}_i$, Δe_i^1, q_i^{norm}, Δe_i^2, and e_i^*, respectively. Equations (4.27)–(4.29) can be represented in the matrix format,

$$\mathbf{G}\left(\mathbf{E}_{\text{rated}} - \bar{\mathbf{E}}\right) = \mathbf{G}\left(\mathbf{E}_{\text{rated}} - \mathbf{H}_{\text{est}}\mathbf{E}\right) = \mathbf{\Delta E}^1, \tag{4.30}$$

$$-b\mathbf{HLQ}^{\text{norm}} = -b\mathbf{HLq}_{\text{rated}}^{-1}\mathbf{Q} = \mathbf{\Delta E}^2, \tag{4.31}$$

$$\mathbf{E}_{\text{rated}} + \mathbf{\Delta E}^1 + \mathbf{\Delta E}^2 = \mathbf{E}^*, \tag{4.32}$$

where $\mathbf{G} = \text{diag}\{G_i\}$ and $\mathbf{H} = \text{diag}\{H_i\}$ are diagonal matrices containing voltage and reactive power controllers, respectively. $\mathbf{G}$ and $\mathbf{H}$ are referred to as the voltage-controller and Q-controller matrices, respectively. $\mathbf{q}_{\text{rated}} = \text{diag}\{q_i^{\text{rated}}\}$ is a diagonal matrix that carries the rated reactive powers of the sources. $\mathbf{E}_{\text{rated}} = E_{\text{rated}}\underline{\mathbf{1}}$, $\mathbf{\Delta E}^1 = \left[\Delta E_i^1, \Delta E_2^1, ..., \Delta E_N^1\right]^{\text{T}}$, $\mathbf{\Delta E}^2 = \left[\Delta E_i^2, \Delta E_2^2, ..., \Delta E_N^2\right]^{\text{T}}$, $\mathbf{E}^* = \left[E_1^*, E_2^*, ..., E_N^*\right]^{\text{T}}$, and $\mathbf{Q}^{\text{norm}} = \left[Q_1^{\text{norm}}, Q_2^{\text{norm}}, ..., Q_N^{\text{norm}}\right]^{\text{T}}$ are column vectors carrying control variables.

It is assumed that for $t < 0$ all sources of the microgrid operate with identical voltage set points, i.e., for all $1 \le i \le N$, $e_i^* = e_{\text{rated}}$ and $\omega_i^* = \omega_{\text{rated}}$ and, thus, $v_i(t) = e_{\text{rated}}\sin(\omega_{\text{rated}}t)$. Then, the proposed controller is activated at $t = 0$. Thus, the quiescent value of any variable x, x^{q}, represents its steady-state value for $t < 0$, i.e., before activating the controller, and the small-signal part, $\hat{x}$, captures the variable

response to the controller activation for $t>0$. Therefore, one can safely write $\boldsymbol{\delta}\mathbf{e}^{1,\mathrm{q}}=\left[\delta e_1^{1,\mathrm{q}},\delta e_2^{1,\mathrm{q}},...,\delta e_N^{1,\mathrm{q}}\right]^{\mathrm{T}}=\mathbf{0}$, $\boldsymbol{\delta}\mathbf{e}^{2,\mathrm{q}}=\left[\delta e_1^{2,\mathrm{q}},\delta e_2^{2,\mathrm{q}},...,\delta e_N^{2,\mathrm{q}}\right]^{\mathrm{T}}=\mathbf{0}$, and $\mathbf{e}^{\mathrm{q}}_{\mathrm{rated}}=e_{\mathrm{rated}}\underline{\mathbf{1}}$ and, accordingly, simplify (4.30)–(4.31),

$$\mathbf{G}\left(\hat{\mathbf{E}}_{\mathrm{rated}}-\mathbf{H}_{\mathrm{est}}\hat{\mathbf{E}}\right)=\boldsymbol{\Delta}\hat{\mathbf{E}}^{1}, \tag{4.33}$$

$$-b\mathbf{H}\mathbf{L}\mathbf{q}^{-1}_{\mathrm{rated}}\left(\frac{\mathbf{q}^{\mathrm{q}}}{s}+\hat{\mathbf{Q}}\right)=\boldsymbol{\Delta}\hat{\mathbf{E}}^{2}, \tag{4.34}$$

where $\mathbf{q}^{\mathrm{q}}=\left[q_1^{\mathrm{q}},q_2^{\mathrm{q}},...,q_N^{\mathrm{q}}\right]^{\mathrm{T}}$ carries the reactive powers supplied by individual sources for $t<0$. Since the rated voltage does not change before and after activating the controller, $\hat{\mathbf{E}}_{\mathrm{rated}}=\mathbf{0}$. The voltage set points dynamics can now be found by substituting (4.33)–(4.34) into (4.32),

$$\hat{\mathbf{E}}^{*}=-\mathbf{G}\mathbf{H}_{\mathrm{est}}\hat{\mathbf{E}}-b\mathbf{H}\mathbf{L}\mathbf{q}^{-1}_{\mathrm{rated}}\left(\frac{\mathbf{q}^{\mathrm{q}}}{s}+\hat{\mathbf{Q}}\right). \tag{4.35}$$

As seen, (4.35) has two terms. The first term, $-\mathbf{G}\mathbf{H}_{\mathrm{est}}\hat{\mathbf{E}}$, represents the controller effort to achieve the global voltage regulation, and, the second term, $-b\mathbf{H}\mathbf{L}\mathbf{Q}^{-1}_{\mathrm{rated}}\left(\mathbf{q}^{\mathrm{q}}/s+\hat{\mathbf{Q}}\right)$, explains how the controller balances reactive load sharing across the microgrid.

Active power regulators (see Fig. 4-2) adjust the active power flow by tuning the phase angles. The controller at each source, e.g., Source i, compares its normalized active power with those of its neighbors and, accordingly, updates the phase angle set point as in (4.7). Controller activation at $t=0$ implies that $\omega_i^{*}(t<0)=\omega_{\mathrm{rated}}$ and, thus, $\delta_i^{\mathrm{q}}=\delta_i^{\mathrm{ss}}(t<0)=0$. Accordingly,

$$\hat{\delta}_i^{*}(t\geq 0)=\int_0^t\sum_{j\in N_i}ca_{ij}(p_j^{\mathrm{norm}}-p_i^{\mathrm{norm}})\,\mathrm{d}\tau. \tag{4.36}$$

Equivalently, in the frequency domain,

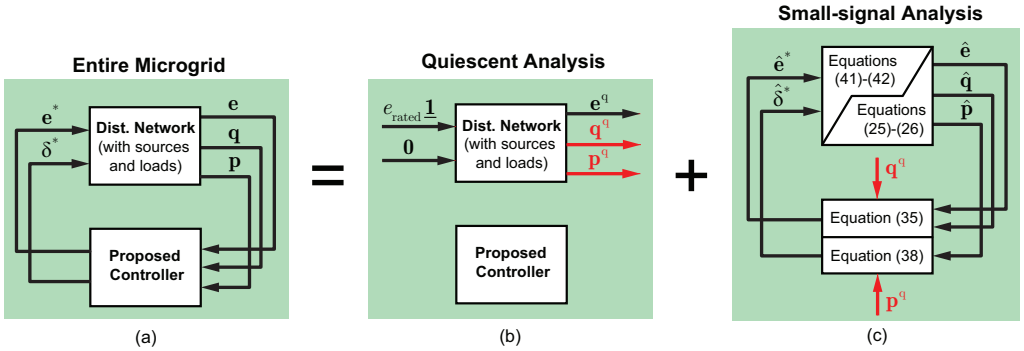

Figure 4-6 Model of the entire microgrid: (a) interaction between the physical layer and the control/cyber layer, (b) quiescent analysis, (c) small-signal analysis.

$$\hat{\Delta}_i^* = \frac{1}{s}\left(\sum_{j\in N_i} ca_{ij}(P_j^{\text{norm}} - P_i^{\text{norm}})\right), \tag{4.37}$$

where $\hat{\Delta}_i^*$ is the Laplace transform of $\hat{\delta}_i^*$. One can write (4.37) in the matrix format,

$$\hat{\boldsymbol{\Delta}}^* = -\frac{c}{s}\mathbf{L}\mathbf{p}_{\text{rated}}^{-1}\mathbf{P} = -\frac{c}{s}\mathbf{L}\mathbf{p}_{\text{rated}}^{-1}\left(\frac{\mathbf{p}^{\text{q}}}{s} + \hat{\mathbf{P}}\right), \tag{4.38}$$

where $\hat{\boldsymbol{\Delta}}^* = \left[\hat{\Delta}_1^*, \hat{\Delta}_2^*, ..., \hat{\Delta}_N^*\right]^{\text{T}}$ and $\mathbf{p}_{\text{rated}} = \text{diag}\{p_i^{\text{rated}}\}$ is a diagonal matrix that includes the rated active powers of the sources. $\mathbf{p}^{\text{q}} = \left[\mathbf{p}_1^{\text{q}}, \mathbf{p}_2^{\text{q}}, ..., \mathbf{p}_N^{\text{q}}\right]^{\text{T}}$ carries the active powers supplied by individual sources before the controller activation, i.e., for $t < 0$. Equation (4.38) represents the phase angles dynamic response to mitigate and, eventually, eliminate the active load sharing mismatch.

4.2.3. Dynamic Model of the Entire Microgrid

Figure 4-6 represents the model of the entire microgrid, which is separated into two sub-models; the quiescent model and the small-signal model. The entire system in the small-signal model can be treated as a multi-input/multi-output plant, where $\mathbf{p}^{\text{q}}/s$ and

$\mathbf{q}^{\mathrm{q}}/s$ are the inputs and $\hat{\mathbf{E}}$, $\hat{\mathbf{P}}$, and $\hat{\mathbf{Q}}$ are the outputs. Equations (4.35) and (4.38) show how the controller adjusts the voltage set points by processing the load sharing mismatches. Dynamic model of the inverters are studied in [187]–[189]. Accordingly, for the inverter driving the Source i, one can write,

$$\hat{\Delta}_i = G_i^{\Delta}\hat{\Delta}_i^*, \tag{4.39}$$

$$\hat{E}_i = G_i^{E}\hat{E}_i^*, \tag{4.40}$$

where G_i^{E} and G_i^{Δ} are the magnitude and phase transfer functions, respectively. Each inverter accommodates an output filter to eliminate the switching harmonics, whose dynamic is included in the transfer functions G_i^{E} and G_i^{Δ}. Equivalently, in the matrix format,

$$\hat{\boldsymbol{\Delta}} = \mathbf{G}^{\Delta}\hat{\boldsymbol{\Delta}}^*, \tag{4.41}$$

$$\hat{\mathbf{E}} = \mathbf{G}^{E}\hat{\mathbf{E}}^*, \tag{4.42}$$

where $\mathbf{G}^{E} = \mathrm{diag}\{G_i^{E}\}$ and $\mathbf{G}^{\Delta} = \mathrm{diag}\{G_i^{\Delta}\}$ are diagonal matrices of the inverter transfer functions. By substituting (4.35) and (4.38) in (4.25)–(4.26), and also using (4.41)–(4.42), one can formulate the entire system.

It is commonly assumed that the transmission/distribution network is predominantly inductive and, thus, active and reactive powers are mainly controlled by adjusting the voltage phases and magnitudes, respectively [190]. This assumption implies that in (4.25) and (4.26), $\mathbf{k}_e^p \simeq \mathbf{0}$ and $\mathbf{k}_\delta^q \simeq \mathbf{0}$, respectively, which helps to find the reduced-order dynamic model of the entire system. Substituting (4.41) in (4.38) and (4.42) in (4.35) yields

$$\left(\mathbf{G}^{\Delta}\right)^{-1}\hat{\boldsymbol{\Delta}} = -\frac{c}{s}\mathbf{L}\mathbf{p}_{\mathrm{rated}}^{-1}\left(\frac{\mathbf{p}^{\mathrm{q}}}{s} + \hat{\mathbf{P}}\right), \tag{4.43}$$

$$\left(\left(\mathbf{G}^{E}\right)^{-1}+\mathbf{G}\mathbf{H}_{\text{est}}\right)\hat{\mathbf{E}}=-b\mathbf{H}\mathbf{L}\mathbf{q}_{\text{rated}}^{-1}\left(\frac{\mathbf{q}^{\text{q}}}{s}+\hat{\mathbf{Q}}\right). \tag{4.44}$$

Substituting the reduced form of (4.25)–(4.26) in (4.43)–(4.44) yields

$$\hat{\mathbf{P}}=-\mathbf{T}_{P}\mathbf{L}\mathbf{p}_{\text{rated}}^{-1}\frac{\mathbf{p}^{\text{q}}}{s}, \tag{4.45}$$

$$\hat{\mathbf{Q}}=-\mathbf{T}_{Q}\mathbf{L}\mathbf{q}_{\text{rated}}^{-1}\frac{\mathbf{q}^{\text{q}}}{s}, \tag{4.46}$$

where, $\mathbf{T}_{P}$ and $\mathbf{T}_{Q}$ are the P–balancing and Q–balancing matrices, and are defied as,

$$\mathbf{T}_{P}\triangleq\left(s\left(c\mathbf{k}_{\delta}^{p}\mathbf{G}^{\Delta}\right)^{-1}+\mathbf{L}\mathbf{p}_{\text{rated}}^{-1}\right)^{-1}, \tag{4.47}$$

$$\mathbf{T}_{Q}\triangleq\left(\left(b\mathbf{k}_{e}^{q}\mathbf{G}^{E}\mathbf{H}\right)^{-1}+b^{-1}\mathbf{H}^{-1}\mathbf{G}\mathbf{H}_{\text{est}}\left(\mathbf{k}_{e}^{q}\right)^{-1}+\mathbf{L}\mathbf{q}_{\text{rated}}^{-1}\right)^{-1}. \tag{4.48}$$

Equations (4.43)–(4.48) describe dynamic response of the entire microgrid with the proposed controller in effect. Equations (4.45)–(4.46) describe that if the power (either active or reactive) was proportionally shared prior to activating the controller, i.e., $\mathbf{p}_{\text{rated}}^{-1}\mathbf{p}^{\text{q}}=n\underline{\mathbf{1}}$ or $\mathbf{q}_{\text{rated}}^{-1}\mathbf{q}^{\text{q}}=m\underline{\mathbf{1}}$, the power flow would remain intact after the controller activation, i.e., $\hat{\mathbf{p}}=\mathbf{0}$ or $\hat{\mathbf{q}}=\mathbf{0}$.

4.2.4. Controller Design Guideline

Appropriate selection of the control parameters is essential for proper operation of the proposed control methodology. For a given microgird, converter transfer function matrices, $\mathbf{G}^{\Delta}$ and $\mathbf{G}^{E}$, rated active and reactive matrices, $\mathbf{p}_{\text{rated}}$ and $\mathbf{q}_{\text{rated}}$, respectively, and $p-\delta$ and $q-e$ transfer matrices, $\mathbf{k}_{\delta}^{p}$ and $\mathbf{k}_{e}^{q}$, respectively, are known. Alternative communication networks may be chosen to exchange information; they, however, must satisfy three requirements; it should be a sparse graph with 1) at least a spanning tree, 2) balanced Laplacian matrix, and 3) minimum communication redundancy. Communication

weights of the graph, a_{ij}, and, thus, the Laplacian matrix, $\mathbf{L}$, directly determine the voltage estimator dynamic, $\mathbf{H}_{\text{est}}$. One may tune the weights and examine the estimators dynamic through (4.9) to achieve a fast enough response. More details and insightful guidelines for optimal design of communication weights in cooperative systems can be found in [191].

Next, the designer may adjust the controller matrices $\mathbf{G} = \text{diag}\{G_i\}$ and $\mathbf{H} = \text{diag}\{H_i\}$ and the coupling gain b by evaluating (4.48) to place all poles of $\mathbf{T}_Q$ in the Open Left Hand Plane (OLHP). Intuitively, smaller gains help to stabilize the entire system while larger gains provide a faster dynamic response. Accordingly, the designer may decide the parameters by making a trade-off between relative stability and settling time. The estimator dynamic should be considerably faster than the microgrid dynamics. Therefore, to evaluate (4.48), one can safely assume $\mathbf{H}_{\text{est}} \simeq \mathbf{M}$. Moreover, inverter switching frequency can be assumed high enough to provide a prompt response to the voltage command, i.e., $\mathbf{G}^E \simeq \mathbf{I}_N$.

As can be seen in Fig. 4-2, two separate modules, i.e., the voltage and the reactive power regulators, adjust the voltage magnitude, e_i^*, by generating two voltage correction terms, δe_i^1 and δe_i^2, respectively. As discussed in Subsection 4.1.2, the voltage regulator is tasked to maintain average voltage across the microgrid at the rated value. Per such assignment, the voltage regulator must act fast to ensure voltage stability/regulation. On the other hand, the reactive power regulator is accountable for reactive load sharing in the steady state and its transient performance has less significance. Accordingly, the voltage control loops (including voltage estimators,

controllers G_i s, and voltage measurement filters) must be designed for a higher bandwidth compared to the reactive power control loops (involving controllers H_i s and reactive power measurement filters). Typically, voltage measurement filters have a relatively high bandwidth as they only need to remove the switching harmonics. On the contrary, besides damping the switching harmonics, the active and reactive measurement units should filter out much lower frequency terms of the line-frequency harmonics and other contents caused by load nonlinearity or unbalance. Such design requirement slows down the power measurements process and, thus, the overall active/reactive load sharing control loops. Accordingly, as a design guideline, it is sufficient to choose the reactive power controllers H_i s to be slightly slower than the voltage controllers G_i s; low bandwidth power measurement filters automatically set the frequency response of the power regulators to be quite slower than the voltage regulator module.

Next step in the design procedure considers active power regulators. Equation (4.45) and (4.47) provide dynamic response of the active load sharing mechanism. Given the fast response of the inverters, one may assume $\mathbf{G}^{\Delta} \simeq \mathbf{I}_N$, which simplifies (4.47). The designer may sweep the coupling gain c and assess the stability and dynamic response through (4.47) to find an appropriate choice for c.

4.2.5. Steady-state Performance Analysis

The design guideline in Subsection 4.2.4 assures stable operation of the microgrid; physical variables such as voltages (magnitude and phase), system frequency, and supplied active and reactive powers would converge to steady-state values. This performance analysis investigates load sharing and voltage regulation quality in the

steady state. To this end, assume that the system operates in the steady state for $t \geq t_0$. It should be noted that although the controller stabilizes voltages across the microgrid, one cannot simply deduce that the voltage and reactive power mismatches are zero. In other words, the inputs to the PI controllers G_i and H_i in Fig. 4-2 may be nonzero in the steady state, yet the two voltage correction terms δe_i^1 and δe_i^2 continuously vary with opposite rates such that sum of the two terms leaves a constant value and, thus, the voltage magnitude set point converges to a steady-state value. The following discussion attempts to show that such a scenario never happens; i.e., the mismatch inputs to both controllers decay to zero in the steady state, resulting in successful global voltage regulation and reactive load sharing. It also explains that the active power mismatch terms would all decay to zero, which provides the desired active load sharing while maintaining the rated frequency.

Voltage regulation and reactive load sharing is first to study. In the steady state, the voltage estimators converge to the true average voltage of the microgrid. Equivalently, $\overline{\mathbf{e}}^{\mathrm{ss}} = \mathbf{M}\mathbf{e}^{\mathrm{ss}} = \left\langle \mathbf{e}^{\mathrm{ss}} \right\rangle \underline{\mathbf{1}}$. Thus, based on the control methodology in Fig. 4-2, one can write

$$\begin{cases} \boldsymbol{\delta}\mathbf{e}^1 = \boldsymbol{\delta}\mathbf{e}_0^1 + \left(\mathbf{G}_{\mathrm{P}} + \mathbf{G}_{\mathrm{I}}(t-t_0)\right)(e_{\mathrm{rated}}\underline{\mathbf{1}} - \mathbf{M}\mathbf{e}^{\mathrm{ss}}) \\ \boldsymbol{\delta}\mathbf{e}^2 = \boldsymbol{\delta}\mathbf{e}_0^2 + \left(\mathbf{H}_{\mathrm{P}} + \mathbf{H}_{\mathrm{I}}(t-t_0)\right)(-b\mathbf{L}\mathbf{q}_{\mathrm{rated}}^{-1}\mathbf{q}^{\mathrm{ss}}) \end{cases}, \tag{4.49}$$

where $\boldsymbol{\delta}\mathbf{e}_0^1$ and $\boldsymbol{\delta}\mathbf{e}_0^2$ are column vectors that carry the integrator outputs in G_is and H_is at $t = t_0$, respectively. Accordingly,

$$\begin{aligned} \mathbf{e}^{*\mathrm{ss}} &= \mathbf{e}_{\mathrm{rated}} + \boldsymbol{\delta}\mathbf{e}^1 + \boldsymbol{\delta}\mathbf{e}^2 \\ &= e_{\mathrm{rated}}\underline{\mathbf{1}} + \boldsymbol{\delta}\mathbf{e}_0^1 + \boldsymbol{\delta}\mathbf{e}_0^2 + \mathbf{G}_{\mathrm{P}}(e_{\mathrm{rated}} - \left\langle \mathbf{e}^{\mathrm{ss}} \right\rangle)\underline{\mathbf{1}} - b\mathbf{H}_{\mathrm{P}}\mathbf{L}\mathbf{q}_{\mathrm{rated}}^{-1}\mathbf{q}^{\mathrm{ss}} \\ &\quad + \left(\mathbf{G}_{\mathrm{I}}(e_{\mathrm{rated}} - \left\langle \mathbf{e}^{\mathrm{ss}} \right\rangle)\underline{\mathbf{1}} - b\mathbf{H}_{\mathrm{I}}\mathbf{L}\mathbf{q}_{\mathrm{rated}}^{-1}\mathbf{q}^{\mathrm{ss}}\right)(t-t_0), \end{aligned} \tag{4.50}$$

where $\mathbf{G}_{\mathrm{I}}$ and $\mathbf{G}_{\mathrm{P}}$ are the diagonal matrices carrying the integral and proportional gains of the voltage-controller matrix $\mathbf{G}$ such that $\mathbf{G}_{\mathrm{P}} + \mathbf{G}_{\mathrm{I}}/s = \mathbf{G}$. Similarly, $\mathbf{H}_{\mathrm{I}}$ and $\mathbf{H}_{\mathrm{P}}$ are the diagonal matrices carrying the integral and proportional gains of the Q-controller matrix $\mathbf{H}$. Equation (4.50) holds for all $t \geq t_0$, and provides a constant voltage set point vector, $\mathbf{e}^{*\mathrm{ss}}$. Thus, the time-varying part of (4.50) is zero or, equivalently,

$$(e_{\mathrm{rated}} - \left\langle \mathbf{e}^{\mathrm{ss}} \right\rangle)\mathbf{U}\underline{\mathbf{1}} = \mathbf{L}\mathbf{q}_{\mathrm{rated}}^{-1}\mathbf{q}^{\mathrm{ss}}, \tag{4.51}$$

where $\mathbf{U} = b^{-1}\mathbf{G}_{\mathrm{I}}\mathbf{H}_{\mathrm{I}}^{-1} = \mathrm{diag}\{u_i\}$ is a diagonal matrix. Multiplying both sides of (4.51) from the left by $\underline{\mathbf{1}}^{\mathrm{T}}$,

$$(e_{\mathrm{rated}} - \left\langle \mathbf{e}^{\mathrm{ss}} \right\rangle)\underline{\mathbf{1}}^{\mathrm{T}}\mathbf{U}\underline{\mathbf{1}} = \underline{\mathbf{1}}^{\mathrm{T}}\mathbf{L}\mathbf{q}_{\mathrm{rated}}^{-1}\mathbf{q}^{\mathrm{ss}}. \tag{4.52}$$

Given the balanced Laplacian matrix, $\underline{\mathbf{1}}^{\mathrm{T}}\mathbf{L} = \mathbf{0}$ [174], which simplifies (4.52),

$$(e_{\mathrm{rated}} - \left\langle \mathbf{e}^{\mathrm{ss}} \right\rangle)\sum_{i=1}^{N} u_i = 0. \tag{4.53}$$

Since all entries of the matrix $\mathbf{U}$ are positive, (4.53) yields $e_{\mathrm{rated}} = \left\langle \mathbf{e}^{\mathrm{ss}} \right\rangle$, which implies that the controllers successfully regulates the averaged voltage magnitude of the microgrid, $\left\langle \mathbf{e}^{\mathrm{ss}} \right\rangle$, at the rated value, e_{rated}. Moreover, by substituting $e_{\mathrm{rated}} - \left\langle \mathbf{e}^{\mathrm{ss}} \right\rangle = 0$ in (4.51),

$$\mathbf{L}\mathbf{q}_{\mathrm{rated}}^{-1}\mathbf{q}^{\mathrm{ss}} = \mathbf{0}. \tag{4.54}$$

If $\mathbf{L}$ is the Laplacian matrix associated with a graph that contains a spanning tree, the only nonzero solution to $\mathbf{L}\mathbf{x} = \mathbf{0}$ is $\mathbf{x} = n\underline{\mathbf{1}}$, where n is any real number [173]. Thus, (4.54) implies $\mathbf{q}^{\mathrm{ss}} = n\mathbf{q}_{\mathrm{rated}}\underline{\mathbf{1}}$, which assures that the controller shares the total reactive load among the sources in proportion to their ratings.

Frequency regulation and active load sharing is the next to study. The controller guarantees the convergence of the voltage magnitude vector, $\mathbf{e}$, and phase angle vector, δ to steady-state values. Thus, (4.6)–(4.7) suggest that all sources would synchronize to the rated frequency, ω_{rated}. Moreover, based on (4.7), stabilizing the phase angles across the microgrid implies that all the frequency correction terms in (4.4) should decay to zero. Equivalently,

$$c\mathbf{L}\mathbf{p}_{\text{rated}}^{-1}\mathbf{p}^{\text{ss}} = \mathbf{0}, \tag{4.55}$$

which offers, $\mathbf{p}^{\text{ss}} = m\mathbf{p}_{\text{rated}}\underline{\mathbf{1}}$, where m is a positive real number. Thus, the controller successfully handles the proportional active load sharing.

4.3. Experimental Verification

A $120/208\ \text{V}, 60\ \text{Hz}$ three-phase AC microgrid, shown in Fig. 4-7, is prototyped in the Intelligent Microgrid Laboratory at Aalborg University. System schematic is described in Fig. 4-8, where four inverter-driven sources are placed in a radial connection to supply two loads, Z_1 and Z_4. The inverters (sources) have similar topologies but different ratings, i.e., the ratings of the inverters 1 and 2 are twice those for the inverters 3 and 4. Each inverter is augmented with an LCL filter to eliminate switching and line-frequency harmonics. RL-circuit model is used for each transmission line. An inductive-resistive distribution network is adopted to investigate collaborative interaction of the active and reactive power regulators in load sharing. Structure of the cyber network is highlighted in Fig. 4-8. Alternative cyber networks for a set of four agents in DC microgrids are discussed by authors in [173], [174] where the ring structure is shown to be the most effective option and, thus, is considered here. It can be seen that the ring connection provides a sparse network that carries the required minimum redundancy where no single communication link failure would hinder the connectivity of the graph.

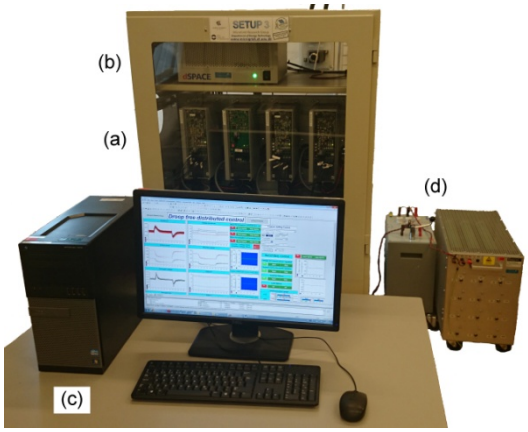

Figure 4-7 AC microgrid prototype: (a) inverter modules, (b) dSAPCE processor board (DS1006), (c) programming and monitoring PC, (d) RL loads.

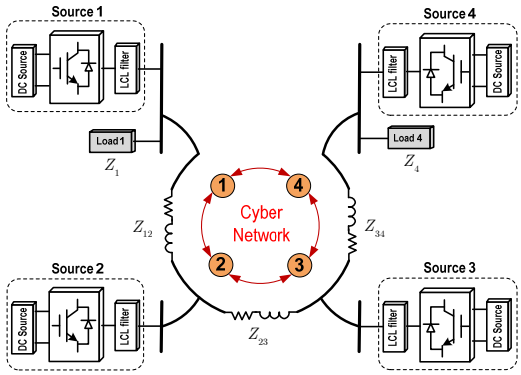

Figure 4-8 Schematic of the microgrid prototype; radial electrical connection and ring cyber network.

Communication links are bidirectional to feature a balanced Laplacian matrix. A dSPACE processor board (DS1006) models the communication channels and implements the control routines. Electrical and control parameters of the microgrid are provided in the Appendix F.

4.3.1. Performance Assessment

Figure 4-9 evaluates performance of the proposed control methodology. Inverters are initially driven with fixed voltage command, i.e., $e_i^* = 120\ \mathrm{V}$ and $\omega_i^* = 120\pi\ \mathrm{rad/s}$. It should be noted that no voltage feedback control had been initially in action to compensate the voltage drop across the LCL filters and, thus, the resulting bus voltages in Fig. 4-9(a) are less than the desired set point, i.e., $e_i^* = 120\ \mathrm{V}$. It can also be seen in Figs. 4-9(e) and 4-8(f) that the total load is not shared among sources in proportion to their power ratings.

It can be seen in the Appendix F that the voltage controllers G_is are designed slightly faster than the reactive power controllers H_i s. Cut-off frequencies of the power measurement filters are as low as $3\ \mathrm{Hz}$ to damp all undesired low-frequency harmonics. These design considerations set the dynamic responses of the two voltage and reactive power regulators apart enough to dynamically separate the two resulting voltage correction terms, i.e., δe_i^1 and δe_i^2. The proposed controller is activated at $t = 8\ \mathrm{s}$. The voltage correction terms have been added to the voltage set points to help with the global voltage regulation and reactive load sharing. Figure 4-9(a) demonstrates that the controllers have boosted the bus voltages across the microgrid to satisfy the global voltage regulation; i.e., for $t > 8\ \mathrm{s}$, the average voltage across the microgrid is successfully regulated at the desired $120\ \mathrm{V}$. As seen in Figs. 4-9(b) and 4-9(c), the first and the second voltage correction terms respond at two different time scales; the first correction term δe_i^1 (output of the voltage regulator) responds four times faster than the second correction term δe_i^2 (output of the reactive power regulator).

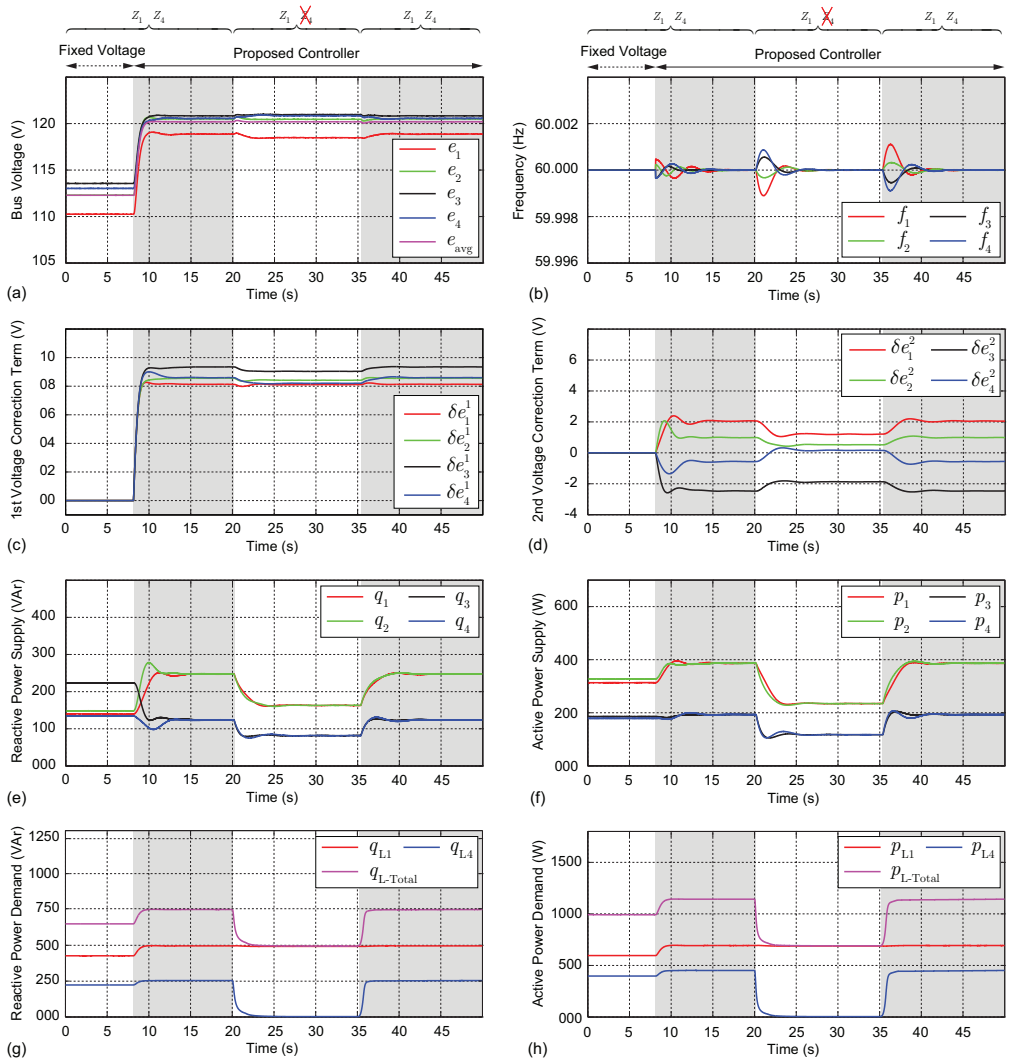

Figure 4-9 Performance evaluation of the proposed controller: (a) bus voltage (phase-to-neutral), (b) inverter frequency set points, (c) first voltage correction term, δe_i^1, (d) second voltage correction term, δe_i^2, (e) supplied reactive power, (f) supplied active power, (g) load reactive power, and (h) load active power. Power ratings of the inverters 1 and 2 are twice those of inverters 3 and 4.

Figure 4-9(b) shows that the controllers have varied the frequency set points in transients to adjust individual phase angles and provide the desired active load sharing. This figure supports the discussions in Section 4.2.5, where the active power regulator is proven to only enforce transient deviations in frequency and that imposes no steady-state deviation. It can be seen that all inverter frequencies synchronize to the rated frequency of $60\ \mathrm{Hz}$ in the steady state. Figures 4-9(e) and 4-9(f) show the filtered power measurements and explain how the controllers have effectively rerouted the power flow to provide proportional load sharing. Individual and total reactive and active load demands are plotted in Figs. 4-9(g) and 4-9(h), respectively. It should be noted that the loads have drawn more power once the controller is activated since the voltages are boosted across the entire microgrid.

Next, the controller performance is studied in response to the load change. The load at Bus 4, Z_4, has been unplugged at $t = 20\ \mathrm{s}$ and plugged back in at $t = 35\ \mathrm{s}$. As seen in Fig. 4-9, the controller has successfully maintained global voltage regulation, frequency synchronization, and proportional load sharing, despite the change in load. It can also be observed in Figs. 4-9(e) and 4-9(f) that the inverters 3 and 4 respond faster to the load change than the other two inverters as they are in closer vicinity of Z_4. Soft load change is performed in this study for safety purposes. In fact, the load inductor at Bus 4 features an air-gap control knob. Using this control opportunity, at $t = 20\ \mathrm{s}$, the load inductance is manually increased to its maximum value to provide an ultimate current damping feature. Then, the load is physically unplugged. A reverse procedure is followed at $t = 35\ \mathrm{s}$ to plug the load, Z_4, back in. This soft load change procedure, besides the damping effect of the power measurement filters, explains why the supplied

powers in Figs. 4-9(e) and 4-9(f) and the load demands in Figs. 4-9(g) and 4-9(h) show a slow and gradual profile rather than sudden changes.

4.3.2. Communication Delay and Channel Bandwidth

Communication is indispensable to access neighbor data and, thus, to the operation of distributed systems. Accordingly, channel non-idealities, e.g., transmission/propagation delay and limited bandwidth, and channel deficiencies such as packet loss may compromise the overall system performance. Thus, low delay and high bandwidth communication protocols are of paramount value for distributed control structures. For example, WiFi and Ultra Wide Band (UWB) protocols offer bandwidths up to 5 GHz and 7.5 GHz, respectively, with delays less than $1\,\mu s$. It should be noted that the length of the communication link directly affects the channel delay. Channel non-ideality effects on the controller performance has been studied in [192] for distributed systems and, particularly, for microgrids in [160], [193], and [194]. It is shown that such non-idealities have a negligible impact on the overall system performance if the channel delay is negligible compared to the controller dynamics. For the underlying microgrid, results in Fig. 4-9 clearly show that the controller dynamics are in the orders of hundreds of milliseconds (or longer); the system dynamics exhibit different time constants for the voltage, active, and reactive power regulation. Therefore, the proposed controller is expected to operate safely with most of the existing communication protocols. To further study the effect of communication delay and limited bandwidth, a detailed model of the underlying microgrid is simulated in MATLAB/SIMULINK environment. Figure 4-10 shows the transient load sharing performance in response to the step load change for a variety of communication delays and bandwidths. It should be noted that the results in this figure present *instantaneous* active and reactive powers; not the filtered measurements.

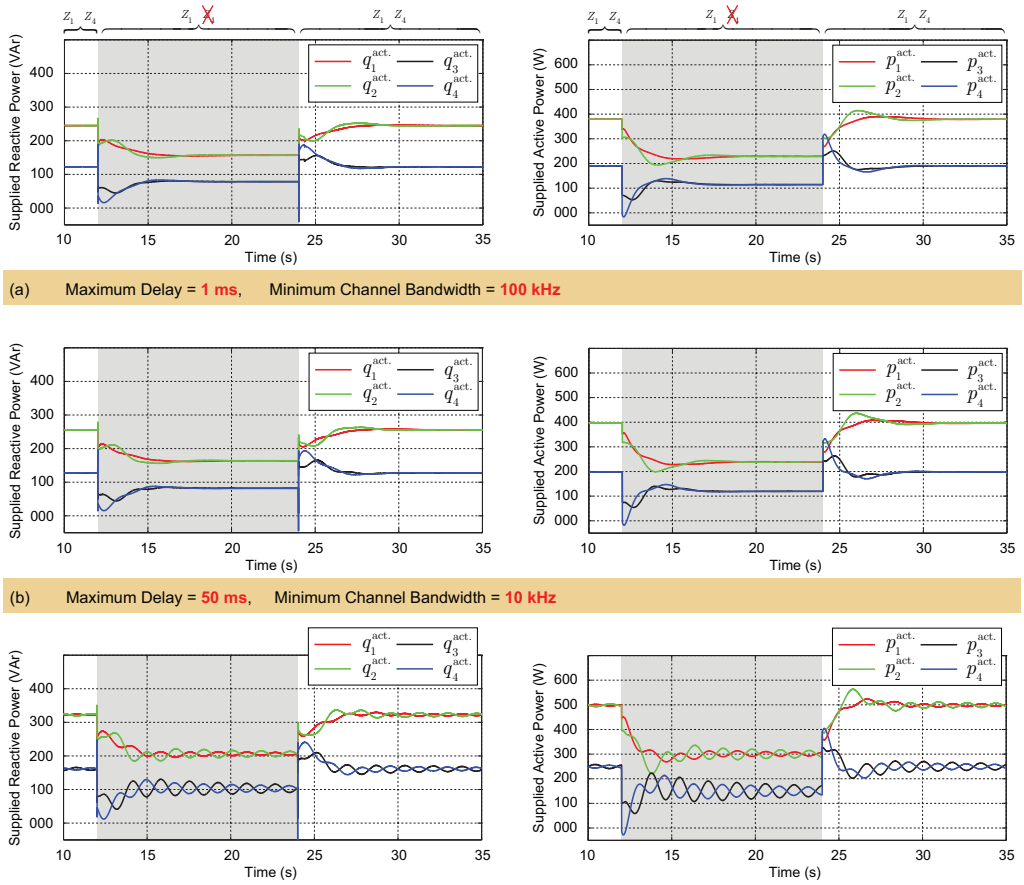

Figure 4-10 Controller performance with non-ideal communication channel. Supplied active and reactive powers for (a) $\mathrm{delay} = 1$ ms and $\mathrm{BW} = 100$ kHz, (b) $\mathrm{delay} = 50$ ms and $\mathrm{BW} = 10$ kHz, and (c) $\mathrm{delay} = 150$ ms and $\mathrm{BW} = 1$ kHz.

However, the controller still processes the filtered quantities. Comparison of studies in Fig. 4-10 shows how large delays can compromise system stability (see Fig. 4-10(c)).

Analysis of distributed control protocols in [195] demonstrates that large communication delays impose DC errors on the voltage estimations and cause drift from a consensus. One can see such effect in Fig. 4-10, where longer delays introduce larger

errors in voltage estimations and lead to bus voltages regulated at higher values than the desired rated voltage. This undesired voltage increment explains elevated supplied powers in Figs. 4-10(b) and 4-10(c) in comparison to Fig. 4-10(a). Simulation studies ensure immunity of the controller performance to delays as long as $10\ \mathrm{ms}$ and channel bandwidths as low as $100\ \mathrm{kHz}$, which makes communication protocols such as WiFi and UWB very suitable for the field implementation.

4.3.3. Plug-and-Play Study

Figure 4-11 studies the plug-and-play capability of the proposed method. Inverter 3 has intentionally been unplugged at $t = 10\ \mathrm{s}$. Although this inverter is turned off instantly, the power measurements exponential decay to zero because of the existing low-pass filters. It should be noted that a source failure also implies loss of all communication links connected to that particular source. Accordingly, when Source 3 fails, it automatically renders the links 2-3 (between Nodes 2 and 3) and 3-4 inoperable. However, as seen in Fig. 4-11, the remaining links still form a connected graph with balanced Laplacian matrix and, thus, the control methodology should remain functional. As seen in Figs. 4-11(c) and 4-11(d), the controllers have successfully responded to the inverter loss and shared the excess power among the remaining inverters in proportion to their power ratings. After the loss of Inverter 3, the voltage measurement for Bus 3 would be unavailable. Thus, the controllers collectively regulate the new average voltage, i.e., the average voltage of the remaining three inverters, at the rated value of $120\ \mathrm{V}$. However, the actual average voltage across the microgrid is seen to be slightly less than the rated voltage. As seen in Fig. 4-11(a), Bus 3 experiences voltage sag due to the loss of generation. It should be noted that although inverter 3 is disconnected from Bus 3 the bus voltage is still available.

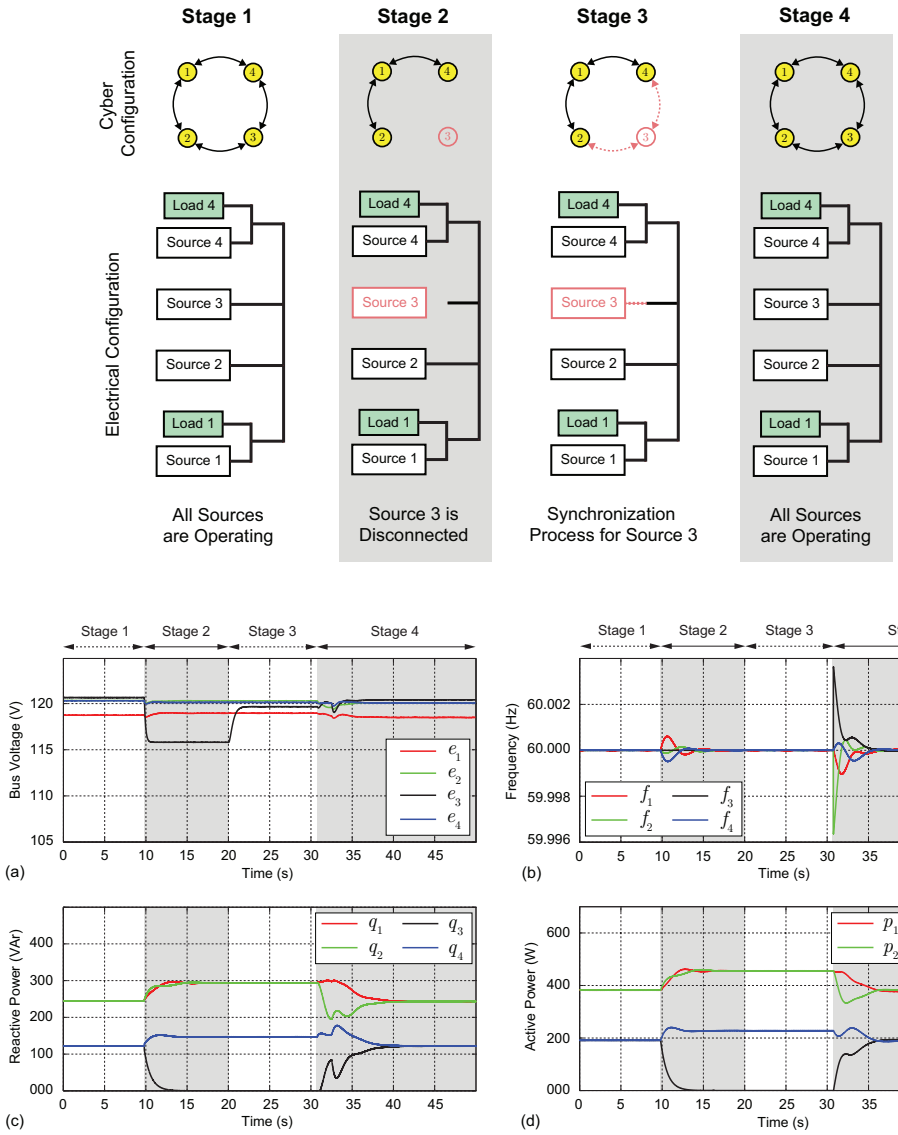

Figure 4-11 Plug-and-play study for Inverter 3: (a) bus voltage (phase-to-neutral), (b) inverter frequency, (c) supplied reactive power, and (d) supplied active power.

Inverter 3 is plugged back in at $t = 20\ \mathrm{s}$; however, the synchronization procedure delays inverter engagement. After successful synchronization, the controller is activated at $t = 31\ \mathrm{s}$ and has shown excellent performance in the global voltage regulation and readjusting the load sharing to account for the latest plugged-in inverter.

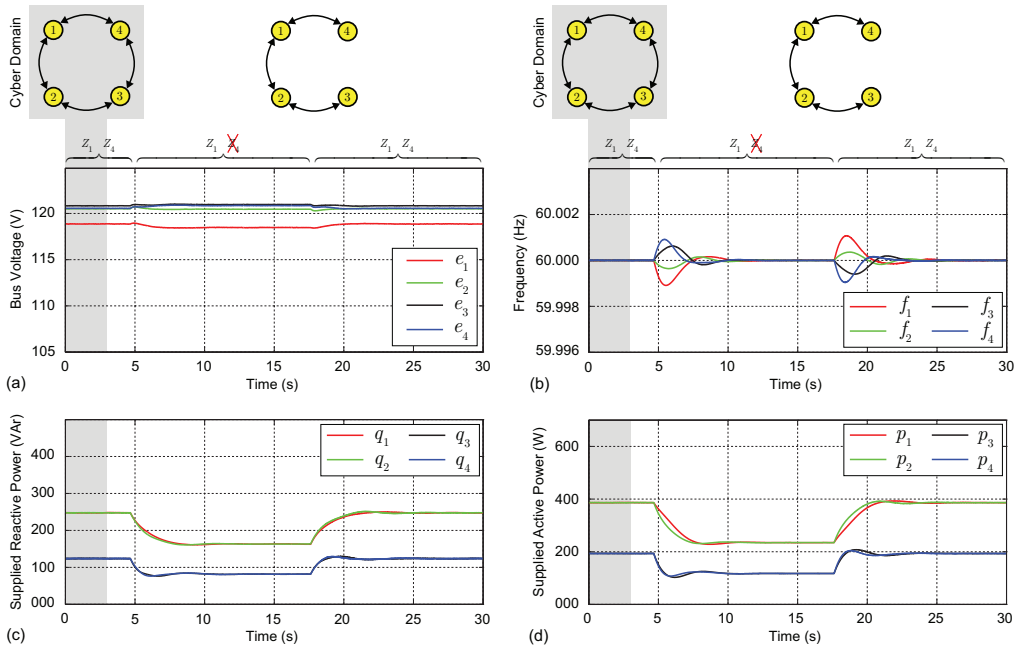

Figure 4-12 Resiliency to failure in Link 3-4: (a) bus voltage (phase-to-neutral), (b) inverter frequency, (c) supplied reactive power, and (d) supplied active power.

4.3.4. Failure Resiliency in Cyber Domain

Resiliency to a single link failure is studied in Fig. 4-12. The original communication graph is designed to carry a minimum redundancy, such that no single communication link failure can compromise the connectivity of the cyber network. As seen in Fig. 4-12, the Link 3-4 has been disabled at $t = 3\,\mathrm{s}$, yet, it does not have any impact on the voltage regulation or load sharing, as the new graph is still connected and has a balanced Laplacian matrix. It should be noted that, by practicing error detection/control protocols in the communication modules, any link failure can be immediately detected at the receiving end. Accordingly, the receiving-end controller updates its set of neighbors by ruling out the node on the transmitting end of the failed link. This reconfiguration ensures that the misleading zero-valued data associated to the

failed link (e.g., zero active and reactive power measurements) will not be processed by the receiving-end controller and, thus, the system remains functional.

The controller response to load change is then studied in Fig. 4-12 with the failed link, where a satisfactory performance is reported. In this study, the load at Bus 4, i.e., Z_4, has been unplugged and plugged back in at $t=5\,\mathrm{s}$ and $t=17.5\,\mathrm{s}$, respectively. It should be noted that although the link failure does not affect the steady-state performance, it slows down the system dynamics as it limits the information flow.

It should be noted that any reconfiguration in the cyber domain, e.g., communication link failure, affects the Laplacian matrix and, thus, the whole system dynamic. However, it will not compromise the steady-state performance of the control methodology, so long as the cyber network remains connected and presents a balanced Laplacian matrix. Connectivity of the cyber network plays a key role in the functionality of the entire microgrid. Including redundant cyber links, as discussed in subsections 4.1.1 and 4.1.2, ensures network connectivity for the most probable contingencies. However, any communication link failure requires immediate attention/maintenance before other links fail. It should be noted that it is very unlikely to lose connectivity due to simultaneous failures of several communication links.

4.4. Summary

A distributed secondary/primary controller is proposed for AC microgrids. The controller embedded on each inverter has three modules: the voltage, reactive power, and the active power regulators. The voltage regulator estimates the global average voltage across the microgrid. This estimation is then further used to adjust the local voltage set point. The reactive power regulator also adjusts the voltage set point by comparing the local normalized reactive power with the neighbors'. The active power regulator compares the local normalized active power with the neighbors' and,

accordingly, adjusts the frequency (or, phase angle) set point to carry out the proportional active power sharing. This control paradigm does not rely on the droop mechanism, yet it is fully distributed, i.e., it uses a sparse communication network for data exchange among inverters. Experimental results show that the proposed cooperative control provides a precise global voltage regulation and proportional load sharing. Controller performance, plug-and-play capability, and resiliency to a single communication link failure are also verified through experiments.

Chapter 5

Assistive Coordination of Power Buffers in DC Microgrids

Distributed generation offers improved efficiency, reliability, expandability, and stability over traditional power grids [196]-[199]. Microgrids are leading examples of such active distribution networks; small-scale power systems where power generation, consumption, and storage occur in a close physical vicinity. The DC natures of emerging renewable energy sources, storage units, and electronically-driven loads lend themselves to a DC distribution paradigm that avoids redundant conversion stages, hence improving conversion efficiency, reliability, and availability compared to their AC counterparts. Moreover, DC microgrids are not afflicted with transformer inrush current, frequency synchronization, reactive power flow, and other power quality issues that are common in AC systems [200]-[202].

Proliferation of power electronics loads in DC distribution networks shifts the load consumption profiles from the traditional constant impedance loads to electronically driven loads with potentially volatile power profiles. Such fast-changing consumption patterns can destabilize the entire distribution network, given its weak nature due to the lack of sufficient generational inertia [203], [204]. Hardware-centric approaches focus on placement and management of energy storage devices to decouple the source and load dynamics, e.g., [205]-[208]. However, widespread utilization of these devices can be costly. Control-centric approaches [209]-[215] are the alternative methods found in the literature.

The concept of power buffer is introduced in [216], [217] to shield the power distribution network from abrupt load changes, and the sensitive loads from the transients in distribution network, by adjusting the effective loading impedance imposed to the distribution network. Power buffers are power electronic converters with two prominent

features. From the hardware perspective, power buffers have relatively large storage components. Form the control perspective, they are mainly concerned with buffering and managing stored energy rather than regulating the voltage/current delivery. The later task is usually performed with a point-of-load converter that follows the power buffer. Therefore, power buffers can provide a holistic approach between the hardware- and control-centric approaches to help damp the effects of transients on the DC distribution networks [218]-[220]. The challenge in the control of power buffers roots in the trade-off between demands of the final loads and the power network and the limited generational capacity in the microgrids.

A geometric manifold is derived from the optimal state trajectories based on the energy-impedance state-space representation in [221]. Game-theoretic solutions for steady-state conditions [222] or trajectory formation [223], [224] are provided in a decentralized fashion. Team formation and player-by-player optimization to find the Nash equilibrium is discussed in [225]. Non-cooperative game-theoretic control frameworks extract geometric manifolds based on the a-priori computation of state trajectories in [226]. Majority of these endeavors neglect the role of the distribution network in problem formulation, leading to a suboptimal trajectory. However, the transmission line impedances practically limit the effective range of a buffer to assist only its physical neighbors. Moreover, the existing literature lacks a closed-form solution to control the buffers; optimal trajectories are usually numerically calculated for the most probable load change/fault scenarios and, then, saved in lookup tables for further use, i.e., when a load transient occurs.

Information exchange, even limited, can group the power buffers to share a common objective and appropriately respond to systematic changes. This work uses a limited information exchange among active loads and establishes an assistive

coordination of these entities in a DC microgrid. It offers an analytical solution that accounts for the distribution network effect. Salient features of this work are as following:

- Power buffers add a degree of freedom in addressing the transient mismatch between the power supplied by the distribution network and the power delivered to the final load.
- A communication network is spanned across the active loads. This network spatially extends the effective range of a power buffer to assist its neighboring loads.
- A distributed cooperative controller is proposed that processes local and neighbor load demands and, accordingly, adjusts local energy set point to assist any local or neighboring load transients.
- Active loads and their physical coupling though the distribution network are properly modeled using the small-signal analysis.

5.1. Preliminary of Power Buffers and Distributed Control

5.1.1. Operational Principle of a Power Buffer

A power buffer is connected in series to a power-electronics-driven load and shapes the instantaneous power profile drawn from the distribution line of the microgrid, as illustrated in Fig. 5-1. Here, *final load* refers to the point-of-load converter and its load. The *active load* refers to the series connection of a power buffer and a final load. In Fig. 5-1, the final load abruptly changes its load, p_{out}, at $t = t_1$. To handle the extra power demand, the power buffer gently ramps up its input power, p_{in}, and, thus, there would be a mismatch between the supplied and the demanded powers.

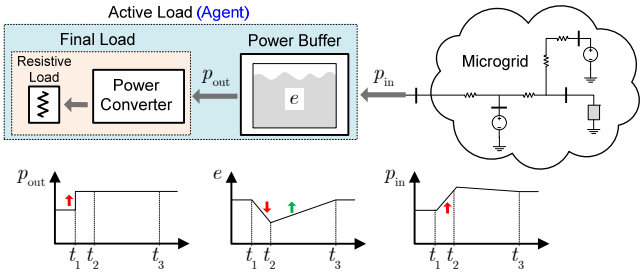

Figure 5-1 Power buffer operation during a step change in power demand.

The buffer uses its stored energy, e, to compensate for this mismatch. At $t = t_2$ the input power reaches the load demand and, thus, the buffering mode ends. Then, the controller triggers the energy restoration procedure. In this stage, i.e., $t_2 < t < t_3$, the buffer slightly draws extra power from the microgrid to restore its energy. At $t = t_3$ the buffer regains its initial energy level and ends the energy restoration mode. For $t > t_3$ the input power to the buffer equals the load power, i.e., $p_{in} = p_{out}$, and the stored energy, e, remains steady until the next load change occurs. It is noteworthy that the buffering interval $[t_1, t_2]$ is significantly shorter than the energy restoration interval $[t_2, t_3]$.

5.1.2. Distributed Control

Active loads can be individually controlled by processing their local measurements, e.g., the final load power or the input bus voltage. However, such a localized approach limits the effectiveness of the power buffer to its local load. Alternatively, nearby active loads can collectively respond to load changes. Here, any active load that can communicate data/measurement with active load i would be called its *neighbor*.

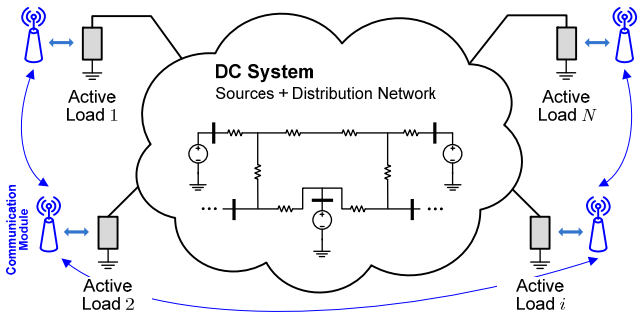

Figure 5-2 Communication modules facilitate data exchange among active loads to perform distributed control routines.

In case of a load change at the active load i, the stored energy of all its neighbor buffers can collectively smoothen the power demanded from the microgrid. It is noteworthy that due to the loss of energy on the transmission lines, seeking assistance from remote buffers is not recommended.

As distributed coordination of active loads requires communication with neighbors, each active load is equipped with a communication module (see Fig. 5-2) that facilitates data exchange with its neighbors. This communication network transforms the DC microgrid into a multi-agent dynamic system where each active load is an *agent*. The set of all neighbors of the agent i, is called the *neighborhood set* and is denote by N_i. Each agent i relays an information vector $\varphi_i = \left[p_i, v_i\right]^{\mathsf{T}}$, which relays its local measurements, to its neighbors and receives their data φ_j, $j \in N_i$. p_i and v_i represent the power supplied by the buffer i and its input voltage, respectively. The controller at agent i will process its local data, φ_i, as well as the neighbors', φ_j s, to appropriately adjust the energy stored in buffer i and provide assistance during transients.

5.2. Proposed Distributed Controller

An active load in a DC microgrid is shown in Fig. 5-3. The figure also elaborates the proposed controller for the power buffer i. A sparse communication network is spanned across the entire microgrid that facilitates data exchange among power buffers; any power buffer is in direct contact with only a few other neighbor buffers and not all other buffers. The controller for the power buffer i processes its local measurements, φ_i, along with the neighbors, i.e., φ_j, $j \in N_i$. Accordingly, it calculates the neighborhood assistive term

$$\delta_i = -\sum_{j \in \bar{N}_i} \mathbf{k}_i^j \varphi_j, \tag{5.1}$$

where control vectors, $\mathbf{k}_i^j \in \mathbb{R}^{1\times 2}$, are design parameters and $\bar{N}_i = \{i, N_i\}$ is the extended neighborhood for buffer i. The neighborhood assistive term, δ_i, is then fed to a controller, G_i, to produce the energy correction term, δe_i. This correction term is then added to the rated energy, e_i^{rated}, to generate the energy set point for buffer i, e_i^*. As the capacitor stores the majority of the energy in a power buffer (e.g., output capacitor in the boost converter), the energy set point can be translated into the capacitor voltage set point as

$$v_{\text{b}i}^* = \sqrt{\frac{2e_i^*}{C_i}}, \tag{5.2}$$

where C_i and $v_{\text{b}i}^*$ are the capacitance and the voltage set point of the buffering capacitor, respectively. The power buffer features fast voltage tracker that assures fast regulation of the voltage, or, equivalently, the energy level to the desired level provided by the proposed controller.

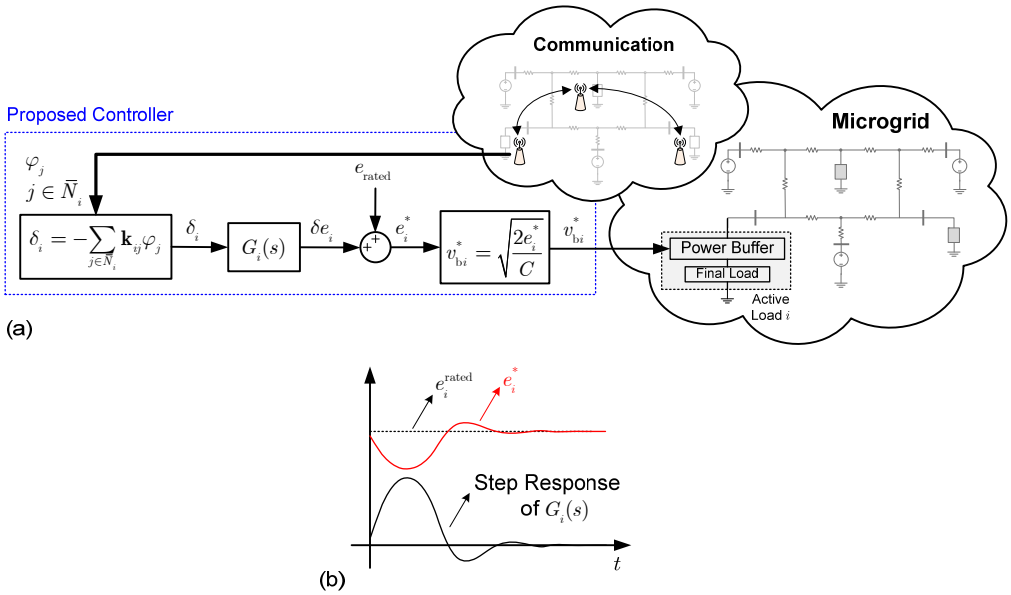

Figure 5-3 Proposed control methodology: (a) functionality of the controller, (b) response of the controller to step load changes.

The controller G_i is a second order controller of the general form of

$$G_i(s) = \frac{a_i s^2 + b_i s}{s^2 + c_i s + d_i}, \tag{5.3}$$

where a_i, b_i, c_i, and d_i are design parameters that shape transient response of the controller. Figure 5-3(b) shows the general shape of the step response of the controller G_i. As can be seen, steady-state response of the controller is zero to DC signals. Thus, during the steady-state operation, the energy correction term, δe_i, damps to zero and the buffer regulates for the rated voltage/energy level. However, during load transients, the controller varies the energy set point to assist the distribution network in providing power. For example, if the load i increases in step, its local controller senses the load change

and, accordingly, the assistive neighborhood term, δ_i, experiences a step drop. The controller, G_i, responds to this drop and adjusts the transient energy level as shown in Fig. 5-3(b). The transient energy loss assists the network in providing the instantaneous excess load power. Equivalently, the controller helps to smoothen the transient current supplied by the distribution network. As the distribution network increases supplied power to respond load demand, the controller increases the energy set point to restore the rated energy reservoir. In addition to the power buffer i, its neighbor buffers would sense the load change and adjust their energy set point to assist the distribution network. Accordingly, one can notice that in case of a load transient, local and neighbor power buffers collectively use their energy reservoir to smoothen the transient current supplied by the distribution network and, intuitively, help to improve stability of the grid. Furthermore, this group assistance of the power buffers enables smaller storage elements in individual buffer designs.

5.3. System-level Modeling

A DC microgrid, as shown in Fig. 5-4(a), is the interconnection of DC sources and loads through a distribution network. Figure 5-4(b) demonstrates the internal architecture of an active load wherein a power buffer drives the final load. Active loads are physically coupled through the distribution network. Therefore, to study the group behavior of the active loads, it is essential to develop a dynamic model that accounts for both the loads and their interconnection through the distribution network, as well as the controller dynamics. This model helps to tune the controller parameters to achieve a desirable coordination of the active loads.

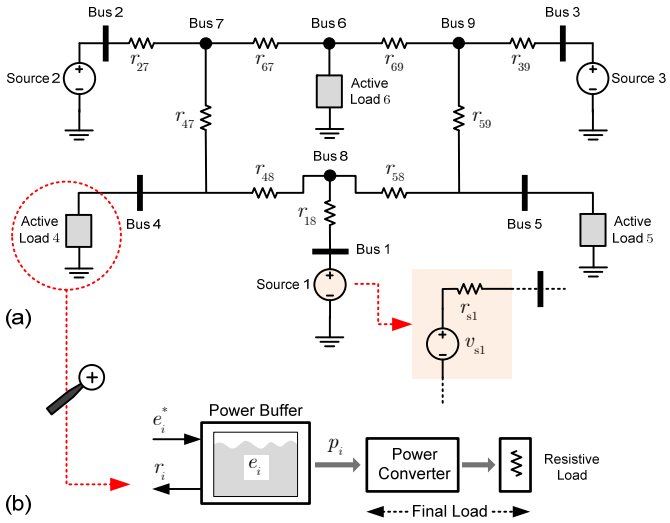

Figure 5-4 DC microgrid layout: (a) physical components including sources, distribution network, and active loads, (b) architecture of an active load.

5.3.1. Dynamic Model of the Physical Entities

For the purpose of analysis, a power buffer is seen as a dynamic system with the control input e_i^*, the disturbance p_i, and the output r_i. This interpretation is shown in Fig. 5-4(b). e_i^*, p_i, and r_i are the set point for the stored energy, the output power, and the input impedance of the buffer i. It should be noted that the point-of-load converter, that drives the resistive load in Fig. 5-4(b), features a fast voltage tracker and, thus, maintains steady stored energy. Accordingly, one can safely conclude that p_i equals the power delivered to the resistive load. Energy-balance equation for the buffer i implies that

$$\dot{e}_i = \frac{v_i^2}{r_i} - p_i. \tag{5.4}$$

As (5.4) suggests a nonlinear model, linearization can be used to capture the system response to small changes in the state variables. Let's express any variable x as

$$x = x^{\mathrm{q}} + \hat{x}, \tag{5.5}$$

where x^{q} and $\hat{x}$ are the quiescent and small-signal portions of the state variable x, respectively. Accordingly, one can linearize (5.4) as

$$\dot{\hat{e}}_i = -\left(i_i^{\mathrm{q}}\right)^2 \hat{r}_i + 2i_i^{\mathrm{q}}\hat{v}_i - \hat{p}_i, \tag{5.6}$$

where $i_i^{\mathrm{q}} = v_i^{\mathrm{q}} \big/ r_i^{\mathrm{q}}$. Equation (5.6) explains how the adjustment of the stored energy in the buffer i, $\hat{e}_i$, can manage the transient impedance profile of the active load, $\hat{r}_i$, in response to the load change $\hat{p}_i$. Assume there exist M sources numbered 1 to M and N loads numbered $M+1$ to $M+N$, where each source or load represents an individual bus in the microgrid. Equation (5.6) can be extended to include all buffer dynamics

$$\dot{\hat{\mathbf{e}}} = -\left(\mathbf{I}^{\mathrm{q}}\right)^2 \hat{\mathbf{r}} + 2\mathbf{I}^{\mathrm{q}}\hat{\mathbf{v}} - \hat{\mathbf{p}}, \tag{5.7}$$

where $\hat{\mathbf{e}} = \begin{bmatrix} \hat{e}_{N+1} & \hat{e}_{N+2} & \cdots & \hat{e}_{M+N} \end{bmatrix}^{\mathsf{T}}$, $\hat{\mathbf{r}} = \begin{bmatrix} \hat{r}_{N+1} & \hat{r}_{N+2} & \cdots & \hat{r}_{M+N} \end{bmatrix}^{\mathsf{T}}$, $\hat{\mathbf{v}} = \begin{bmatrix} \hat{v}_{N+1} & \hat{v}_{N+2} & \cdots & \hat{v}_{M+N} \end{bmatrix}^{\mathsf{T}}$, and $\hat{\mathbf{p}} = \begin{bmatrix} \hat{p}_{N+1} & \hat{p}_{N+2} & \cdots & \hat{p}_{M+N} \end{bmatrix}^{\mathsf{T}}$ are the small signal portions of the energy, impedance, voltage and power vectors, respectively. $\mathbf{I}^{\mathrm{q}} = \mathrm{diag}\left\{i_i^{\mathrm{q}}\right\}$ is a diagonal matrix that carries quiescent currents supplied to the power buffers.

The voltage variation in (5.6), $\hat{v}_i$, not only depends on the local load change, $\hat{p}_i$, but also on the response of all other loads and sources in the microgrid. The distribution network couples the load dynamics, i.e., as one load's power demand changes, it changes the current flow across the entire microgrid and, thus, affects the voltages globally. Modeling the interaction of the loads and sources through the distribution network explains how the

voltage varies across the entire microgrid in response to the load change, $\hat{p}_i$. The admittance matrix, $\mathbf{y}$, models the interaction between the loads and sources.

Besides source and load terminals there might be other intermediate buses in the distribution network. However, reduction methods, e.g., the Kron reduction, can be used to eliminate intermediate buses such that the reduced admittance matrix only represents the interaction between the sources and loads. Accordingly, one can write

$$\underbrace{\left[\underbrace{v_{s1}/r_{s1} \quad \cdots \quad v_{sM}/r_{sM}}_{\mathbf{i}} \;\middle|\; 0 \quad \cdots \quad 0\right]^{\mathsf{T}}}_{} = \mathbf{y}\underbrace{\left[v_1 \quad \cdots \quad v_M \;\middle|\; v_{M+1} \quad \cdots \quad v_{M+N}\right]^{\mathsf{T}}}_{\mathbf{v}_{\mathrm{MG}}}, \tag{5.8}$$

where each source i is modeled as the series connection of a regulated voltage source, v_{si}, and a resistor, r_{si}, as shown in Fig. 5-4(a). Entries of the admittance matrix, $\mathbf{y}$, are determined by the admittance of the sources, loads, and the distribution lines. Small-signal analysis of (5.8) results in

$$\mathbf{i}^{\mathrm{q}} + \hat{\mathbf{i}} = \left(\mathbf{y}^{\mathrm{q}} + \hat{\mathbf{y}}\right)\left(\mathbf{v}_{\mathrm{MG}}^{\mathrm{q}} + \hat{\mathbf{v}}_{\mathrm{MG}}\right) \Rightarrow \hat{\mathbf{i}} = \mathbf{y}^{\mathrm{q}}\hat{\mathbf{v}}_{\mathrm{MG}} + \hat{\mathbf{y}}\mathbf{v}_{\mathrm{MG}}^{\mathrm{q}}. \tag{5.9}$$

Given the regulated internal voltages of all sources, entries of the current vector $\mathbf{i}$ are constant and, thus, $\hat{\mathbf{i}} = \mathbf{0}$. Therefore, (5.9) yields

$$\hat{\mathbf{v}}_{\mathrm{MG}} = -\left(\mathbf{y}^{\mathrm{q}}\right)^{-1}\hat{\mathbf{y}}\mathbf{v}_{\mathrm{MG}}^{\mathrm{q}} = -\mathbf{z}^{\mathrm{q}}\hat{\mathbf{y}}\mathbf{v}_{\mathrm{MG}}^{\mathrm{q}}, \tag{5.10}$$

where $\mathbf{z}^{\mathrm{q}} = \left(\mathbf{y}^{\mathrm{q}}\right)^{-1}$ is the impedance matrix. Intuitively, the load change at the active load i globally affects the power flow and, consequently, the voltage regulation across the microgrid. Accordingly, all other active loads would adjust their input impedances, $\hat{r}_j$ s, to maintain their desired power delivery. Therefore, $\hat{\mathbf{y}}$ can be generally written as

$$\hat{\mathbf{y}} = \left[\begin{array}{c|ccc} \mathbf{0}^{M\times M} & \multicolumn{3}{c}{\mathbf{0}^{M\times N}} \\ \hline \mathbf{0}^{N\times M} & \dfrac{-\hat{r}_{M+1}}{\left(r^{\mathrm{q}}_{M+1}\right)^2} & \cdots & 0 \\ & \vdots & \ddots & \vdots \\ & 0 & \cdots & \dfrac{-\hat{r}_{M+N}}{\left(r^{\mathrm{q}}_{M+N}\right)^2} \end{array}\right], \tag{5.11}$$

which captures the effect of all impedance variations, i.e., $\hat{r}_i$ s. Plugging (5.11) into (5.10) gives

$$\begin{aligned} \hat{\mathbf{v}}_{\mathrm{MG}} &= \mathbf{z}^{\mathrm{q}} \left[\begin{array}{ccc|ccc} 0 & \cdots & 0 & \dfrac{\hat{r}_{M+1} v^{\mathrm{q}}_{M+1}}{\left(r^{\mathrm{q}}_{M+1}\right)^2} & \cdots & \dfrac{\hat{r}_{M+N} v^{\mathrm{q}}_{M+N}}{\left(r^{\mathrm{q}}_{M+N}\right)^2} \end{array}\right]^{\mathsf{T}} \\ &= \Gamma_{\mathrm{MG}} \left[\begin{array}{ccc} \hat{r}_{M+1} & \hat{r}_{M+2} & \cdots \quad \hat{r}_{M+N} \end{array}\right]^{\mathsf{T}} = \Gamma_{\mathrm{MG}} \hat{\mathbf{r}}, \end{aligned} \tag{5.12}$$

where $\Gamma_{\mathrm{MG}} = \left[\gamma_{ij}\right] \in \mathbb{R}^{(N+M)\times N}$. Particularly, (5.12) implies that each load voltage variation, $\hat{v}_i$, can be expressed as a linear function of the impedance variations, $\hat{r}_i$ s, i.e.,

$$\hat{v}_i = \sum_{j=M+1}^{M+N} \gamma_{ij} \hat{r}_j, \qquad i = M+1, \cdots, M+N, \tag{5.13}$$

or, in other words,

$$\hat{\mathbf{v}} = \Gamma \hat{\mathbf{r}}. \tag{5.14}$$

which only formulates the variations of the voltages supplying active loads. Equation (5.12) models the physical coupling among the active loads, and, together with (5.7), form the dynamic model of the entire microgrid.

5.3.2. Dynamic Model of the Controller

Herein, x^* and X represents the set point for variable x and its Laplace transform, respectively. According to the proposed controller in Section 5.2, for the power buffer i,

$$\hat{E}_i^* = -G_i \sum_{j \in \bar{N}_i} \mathbf{k}_i^j \psi_j = -G_i \mathbf{k}_i \Psi \tag{5.15}$$

where $\Psi = \begin{bmatrix} \psi_{N+1} & \psi_{N+2} & \cdots & \psi_{M+N} \end{bmatrix}^{\mathsf{T}}$ is the Laplace transform of the global information vector and ψ_i is the Laplace transform of the information vector for buffer i, φ_i. $\mathbf{k}_i = \begin{bmatrix} \mathbf{k}_i^{M+1} & \mathbf{k}_i^{M+2} & \cdots & \mathbf{k}_i^{M+N} \end{bmatrix}^{\mathsf{T}}$ is a vector that carries self and neighborhood control gains; $\mathbf{k}_i^j = \mathbf{0}$ if $j \notin \bar{N}_i$. As the global information vector, Ψ, carries voltage and power measurements, one can write (5.15) as

$$\hat{E}_i^* = -G_i \left(\mathbf{k}_{iv} \mathbf{V} + \mathbf{k}_{ip} \mathbf{P} \right), \tag{5.16}$$

where $\mathbf{k}_{iv}$ and $\mathbf{k}_{ip}$ carry the control gains in $\mathbf{k}_i$ that correspond to voltage and power measurements, respectively. As the steady-state response of the controller G_i to the quiescent values of the voltage and power vectors, $\mathbf{v}^{\mathrm{q}}$ and $\mathbf{p}^{\mathrm{q}}$, respectively, are zero, one can write (5.16) as Thus,

$$\hat{E}_i^* = -G_i \left(\mathbf{k}_{iv} \hat{\mathbf{V}} + \mathbf{k}_{ip} \hat{\mathbf{P}} \right), \tag{5.17}$$

or, in the global format,

$$\hat{\mathbf{E}}^* = -\mathbf{G} \left(\mathbf{k}_{\mathrm{v}} \hat{\mathbf{V}} + \mathbf{k}_{\mathrm{p}} \hat{\mathbf{P}} \right), \tag{5.18}$$

where $\mathbf{k}_{\mathrm{v}}$ and $\mathbf{k}_{\mathrm{p}}$ are matrices that concatenate vectors $\mathbf{k}_{iv}$ and $\mathbf{k}_{ip}$, respectively, for all active loads.

$\mathbf{G} = \mathrm{diag}\left\{ G_i \right\}$ is a diagonal matrix that carries the controller transfer functions. Multiplying both sides of (5.18) by s gives

$$s\hat{\mathbf{E}}^* = -s\mathbf{G} \left(\mathbf{k}_{\mathrm{v}} \hat{\mathbf{V}} + \mathbf{k}_{\mathrm{p}} \hat{\mathbf{P}} \right), \tag{5.19}$$

which represents the global controller dynamics.

5.3.3. Dynamic Model of the Entire Microgrid

Equations (5.7) and (5.14) can be expressed in the frequency domain

$$s\hat{\mathbf{E}} = -\left(\mathbf{I}^{\mathrm{q}}\right)^2 \hat{\mathbf{R}} + 2\mathbf{I}^{\mathrm{q}}\hat{\mathbf{V}} - \hat{\mathbf{P}}, \tag{5.20}$$

$$\hat{\mathbf{V}} = \Gamma\hat{\mathbf{R}}. \tag{5.21}$$

By substituting (5.21) in (5.20)

$$s\hat{\mathbf{E}} = \mathbf{I}^{\mathrm{q}}\left(2\Gamma - \mathbf{I}^{\mathrm{q}}\right)\hat{\mathbf{R}} - \hat{\mathbf{P}}. \tag{5.22}$$

Given the fast voltage trackers on power buffers, one can safely assume that each power buffer promptly regulates its voltage on the desired set point. Equivalently, it immediately adjusts the energy level on the desired value, i.e., $e_i = e_i^*$ or $\mathbf{e} = \mathbf{e}^*$. Thus,

$$\hat{\mathbf{E}} = \hat{\mathbf{E}}^*. \tag{5.23}$$

Comparing (5.19) and (5.22), given (5.23), yields

$$\left(\mathbf{I}_N - s\mathbf{G}\mathbf{k}_{\mathrm{p}}\right)\hat{\mathbf{P}} = \left(2\mathbf{I}^{\mathrm{q}}\Gamma - \left(\mathbf{I}^{\mathrm{q}}\right)^2 + s\mathbf{G}\mathbf{k}_{\mathrm{v}}\Gamma\right)\hat{\mathbf{R}}. \tag{5.24}$$

By substituting (5.24) in (5.12)

$$\hat{\mathbf{V}}_{\mathrm{MG}} = \Gamma_{\mathrm{MG}}\left(2\mathbf{I}^{\mathrm{q}}\Gamma - \left(\mathbf{I}^{\mathrm{q}}\right)^2 + s\mathbf{G}\mathbf{k}_{\mathrm{v}}\Gamma\right)^{-1}\left(\mathbf{I}_N - s\mathbf{G}\mathbf{k}_{\mathrm{p}}\right)\hat{\mathbf{P}}. \tag{5.25}$$

Equation (5.25) determines the voltage dynamics throughout the microgrid in response to the load change $\hat{\mathbf{P}}$. It is noteworthy that when the proposed controller is deactivated, $\mathbf{k}_{\mathrm{p}} = \mathbf{k}_{\mathrm{v}} = \mathbf{0}$ and, thus,

$$\hat{\mathbf{V}}_{\mathrm{MG}} = \Gamma_{\mathrm{MG}}\left(2\mathbf{I}^{\mathrm{q}}\Gamma - \left(\mathbf{I}^{\mathrm{q}}\right)^2\right)^{-1}\hat{\mathbf{P}}, \tag{5.26}$$

which implies that the voltage variations, $\hat{\mathbf{v}}_{\mathrm{MG}}$, follow the exact dynamic of the power changes, $\hat{\mathbf{p}}$, as each voltage variation $\hat{v}_i$ can be expressed as a linear function of the power changes, $\hat{p}_j$s. Control matrices in (5.25), i.e., $\mathbf{k}_{\mathrm{p}}$, $\mathbf{k}_{\mathrm{v}}$, and $\mathbf{G}$, are control

parameters and can be freely chosen to provide a desired dynamic response to step load changes, which can be evaluated through (5.25).

5.4. Hardware-in-the-Loop Verification

A 48 V DC microgrid, that collectively supplies three active loads through three sources, is adopted to study the proposed control methodology. Schematic of the DC microgrid is shown in Fig. 5-5(a), where a resistive distribution system spans among sources and loads. Figure 5-5(b) elaborates the design of an active load incorporating the power buffer and the point-of-load converter. Accordingly, each active load consists of three modules: 1) an adjustable resistive load, 2) a buck converter, and 3) a boost converter. The buck converter features a fast Proportional-Integral (PI) controller and drives the resistive load at the fixed voltage set point of $48\ \mathrm{V}$. The boost converter features large storage elements, particularly, a large output capacitor. It drives the final load at the rated voltage of $100\ \mathrm{V}$, however, this voltage set point is subject to vary in load transients, as the buffer varies its stored energy to perform the proposed control routine and smoothen the system transients. A high-frequency LC filter is placed in the design between the buck and the boost converters to eliminate high-frequency contents of the current drawn by the buck converter. Each load carries a communication module to exchange information with neighbor loads. Cyber neighborhood assignment in this study is inspired by physical vicinity; a load exchanges information with those loads that are in its physical vicinity. Figure 5-5(c) exhibits the communication network. Control and physical parameters of the underlying system are provided in detail in the Appendix G.

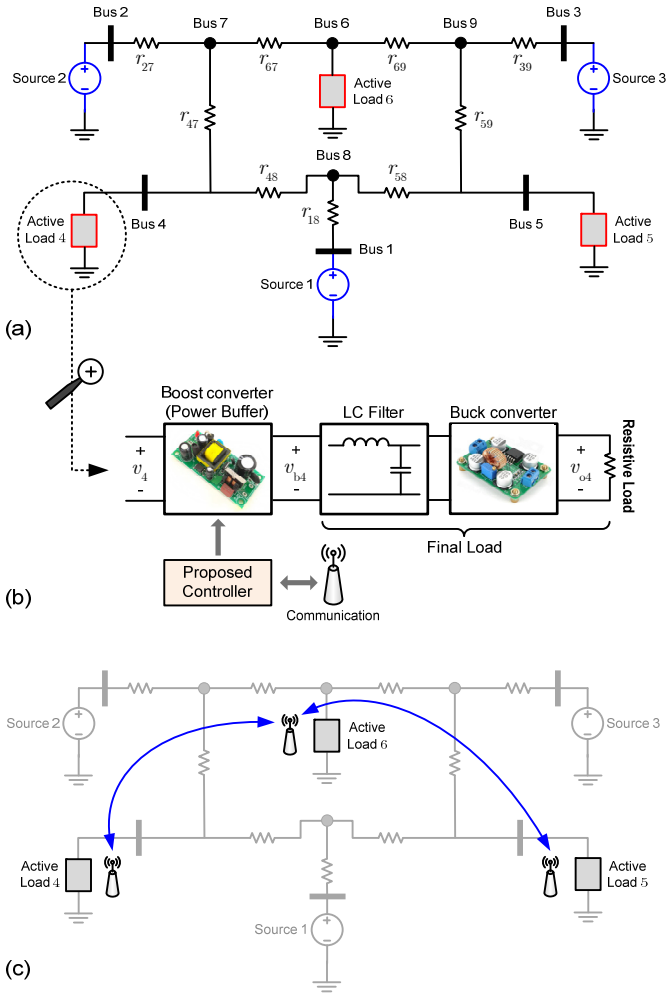

Figure 5-5 DC microgrid layout: (a) physical layer that includes sources, distribution network, and the active loads, (b) structure of an active load, (c) communication network among active loads.

Hardware-in-the-Loop (HIL) simulation is a fast prototyping approach that is commonly used for controller development and performance assessment. This validation approach significantly reduces the prototyping time and cost and, thus, is considered in this study.

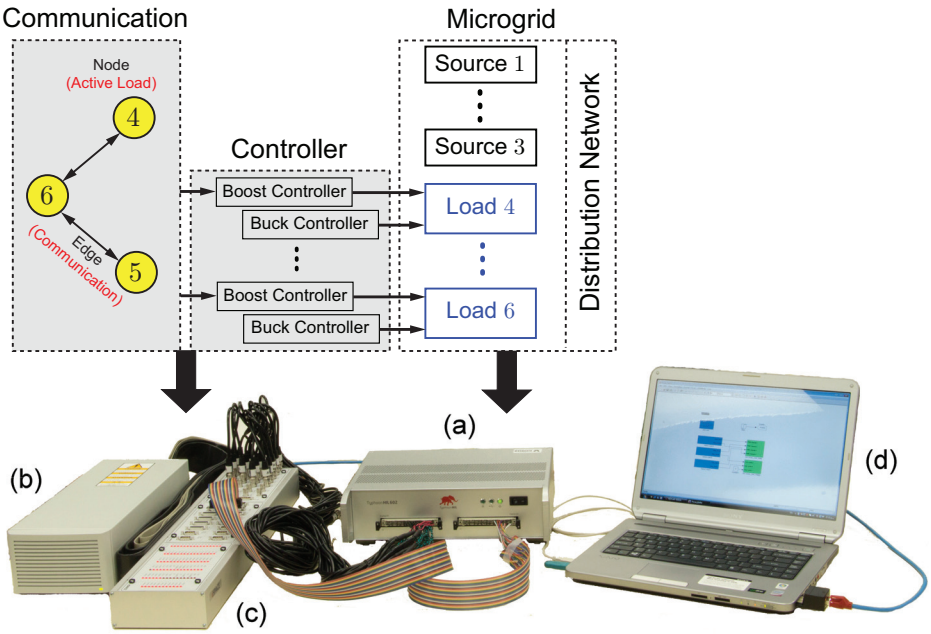

Figure 5-6 Hardware-in-the-loop setup: (a) Typhoon HIL 602 (emulates the physical components of the underlying microgrid), (b) dSPACE Controller DS1103 (handles the control routines), (c) analog/digital expansion board, (d) programming/monitoring computer.

It enables fast and effective adjustment of the control parameters for a superb field performance. HIL simulation features a computational setup that provides real-time simulation of the physical entities of the underlying cyber-physical system. This computational system joins with a controller that carries the developed control routine; the controller performance would be measured against the HIL-generated waveforms rather than waveforms of an actual physical system. Figure 5-6 shows the HIL setup. A Typhoon HIL 602 is used to emulate the entire physical components of the microgrid in Fig. 5-5(a). A dSPACE controller board (DS1103) is used for controller implementation and managing information exchange among active loads.

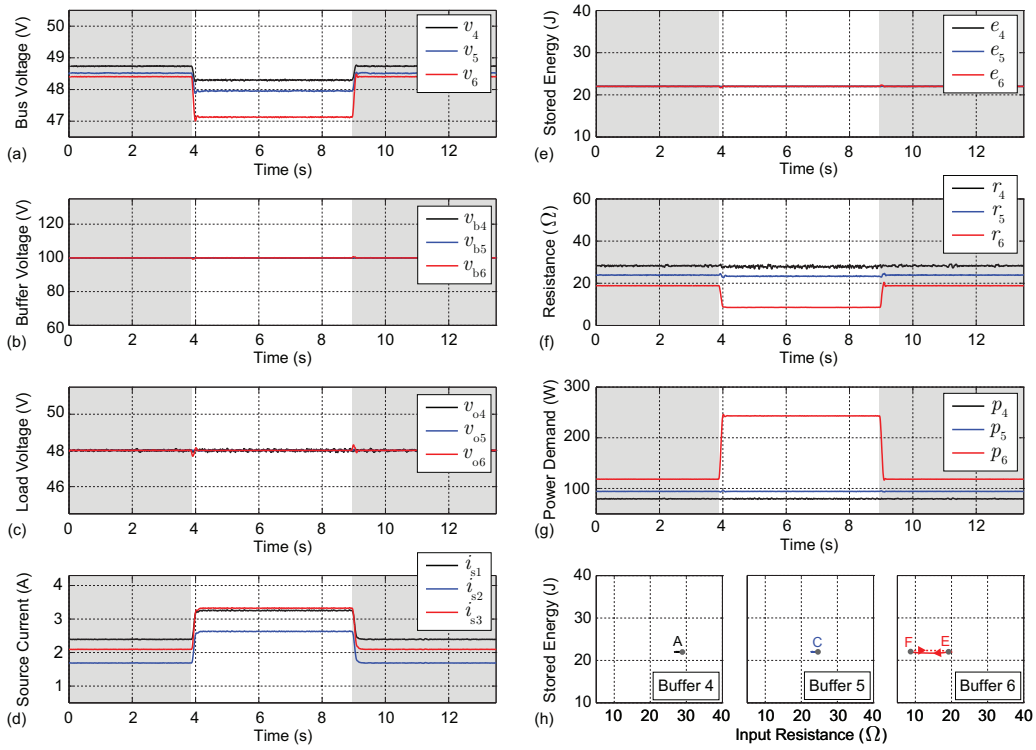

Figure 5-7 Microgrid performance in response to the load change at terminal 6 with deactivated power buffers: (a) microgrid bus voltages at the load terminals, (b) output voltage of the power buffers, (c) output voltage across the resistive loads, (d) source currents, (e) stored energy in power buffers, (f) input impedance of the power buffers, (g) output of the active loads, (h) energy-impedance trajectories of the power buffers during the load transient.

5.4.1. Conventional Approach, Deactivated Power Buffers

This study replicates conventional control approach where the voltage controller on the point-of-load converters work with fixed set point of $v_{oi}^{*} = 48\ \mathrm{V}$. All buffers are deactivated, i.e., the buffers work with a fixed voltage set point of $v_{bi}^{*} = 100\ \mathrm{V}$, and do

not use their stored energy to assist load transients. Resistive loads connected to terminals 4, 5, and 6 are $30\,\Omega$, $25\,\Omega$, and $20\,\Omega$, respectively. Figure 5-7 shows the empirical results. At $t = 3.9\ \mathrm{s}$, the load at bus 6 is changed in step from $20\,\Omega$ to $10\,\Omega$, which doubles the power demand, as seen in Fig. 5-7(g). A sudden change in the bus voltages, source currents, and input resistance of the converters, v_is, i_{si}s, and r_is, respectively, can be seen. It can also be seen in Figs. 5-7(b) and 7(c) that the voltage controllers on the boost and buck converters respond fast to the load change and preserve regulated voltages. Figure 5-7(f) exhibits the input impedance of the active loads, i.e., the input impedance of the boost converters.

Figure 5-7(h) represents the energy-impedance trajectory of the boost converters during the load change. As seen, only the converter supplying the varied load, i.e., load 6, shows a transient behavior while other converters tend not to change their energy or impedance. It can also be seen that the converter 6 reduces its impedance while keeping its stored energy almost intact as the trajectory moves from point E to point F. Such observation implies that the boost converter is not in the buffering mode and maintains a steady energy reserve throughout its operation. The load at bus 6 is changed back to $20\,\Omega$ At $t = 8.9\ \mathrm{s}$ and, accordingly, the energy-impedance trajectory for the buffer in load 6 travels back to point E. The dashed lines in Fig. 5-7(h) show the trajectories when the load changes back to $20\,\Omega$.

5.4.2. Proposed Method, Single Assisting Buffer

The power buffers are activated to perform the proposed control methodology. The load at bus 4 experiences a step change from $30\,\Omega$ to $15\,\Omega$ at $t = 3.85\ \mathrm{s}$.

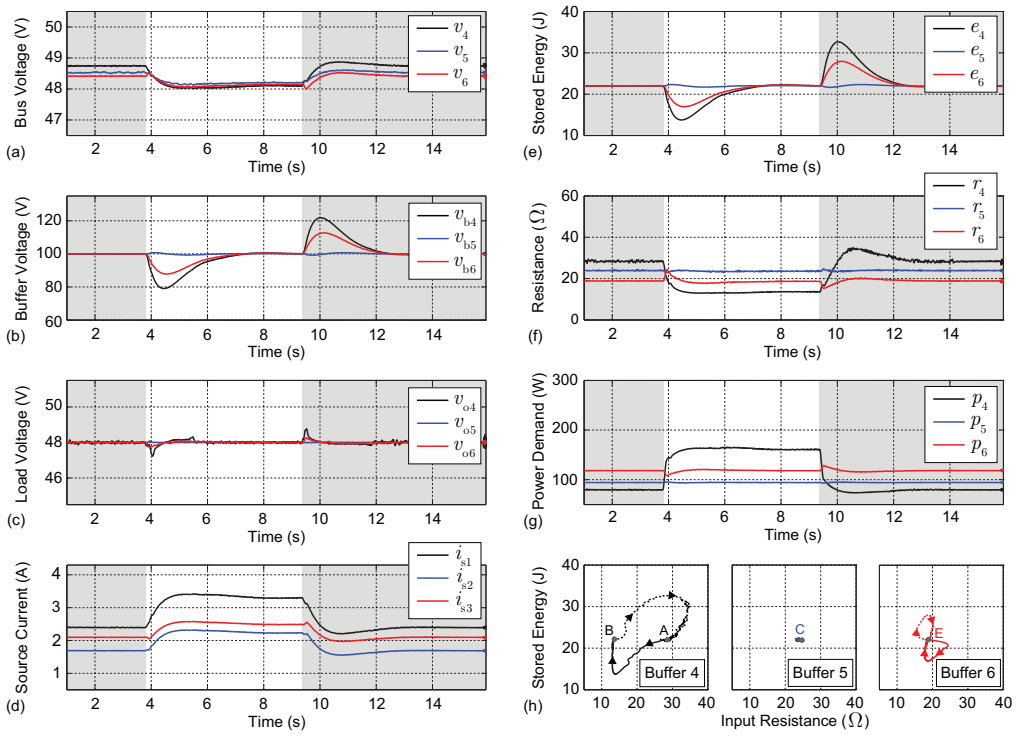

Figure 5-8 Controller performance in response to the load change at terminal 4; single assisting neighbor: (a) microgrid bus voltages at the load terminals, (b) output voltage of the power buffers, (c) output voltage across the resistive loads, (d) source currents, (e) stored energy in power buffers, (f) input impedance of the power buffers, (g) output of the active loads, (h) energy-impedance trajectories of the power buffers during the load transient.

As seen in Fig. 5-5(c), load 6 is the only neighbor of load 4 and, thus, engages in supporting the load transient with its stored energy. Figure 5-8 exhibits the state variables during this study. Fast voltage regulation can be observed in Fig. 5-8(c). It can be seen in Figs. 5-8(a), 5-8(d), and 5-8(f) that the controller has successfully smoothen the bus voltages, sources currents, and buffer impedances in response to the step load transient (see Fig. 5-8(g)).

Buffers 4 and 6 use their stored energy to smoothen the impedance profile. Load 5 is not a neighbor of load 4 and, thus, has taken no action; it maintains its energy and impedance steadily at point C in Fig. 5-8(h). Figures 5-8(b) and 8(e) show how buffers 4 and 6 spend their stored energy during the load transient. The energy-impedance trajectories in Fig. 5-8(h) exhibit movements only in buffers 4 and 6. During the load transient, buffer 6 starts from point E and triggers assisting buffer 4 by dropping its energy and increasing its impedance. It, then, gradually regains its stored energy and moves back to the starting condition, i.e., point E. Buffer 4 drops its energy and, at the same time, decreases its impedance to respond to the load transient. After reaching the desired impedance level, it slightly absorbs more power to reestablish its initial energy level. By comparison, with no buffering effect, the trajectory would go straight from point A to point B. The load at bus 4 is changed back to $30\ \Omega$ At $t = 9.2\ \mathrm{s}$ and, accordingly, the energy-impedance trajectory for the buffer in load 4 travels back to point A. The dashed lines in Fig. 5-8(h) show the trajectories when the load changes back to $30\ \Omega$.

5.4.3. Proposed Method, Multiple Assisting Buffer

The load at bus 6 changes from $20\ \Omega$ to $10\ \Omega$ at $t = 2.9\ \mathrm{s}$. As seen in Fig. 5-4(c), load 6 has two neighbors, loads 4 and 5, which both will assist with this load transient. Figure 5-9 exhibits the state variables during this study. Figures 5-9(a), 5-9(d), and 5-9(f) clearly show that the controller has successfully smoothen the bus voltages, sources currents, and buffer impedances in response to the load transient.

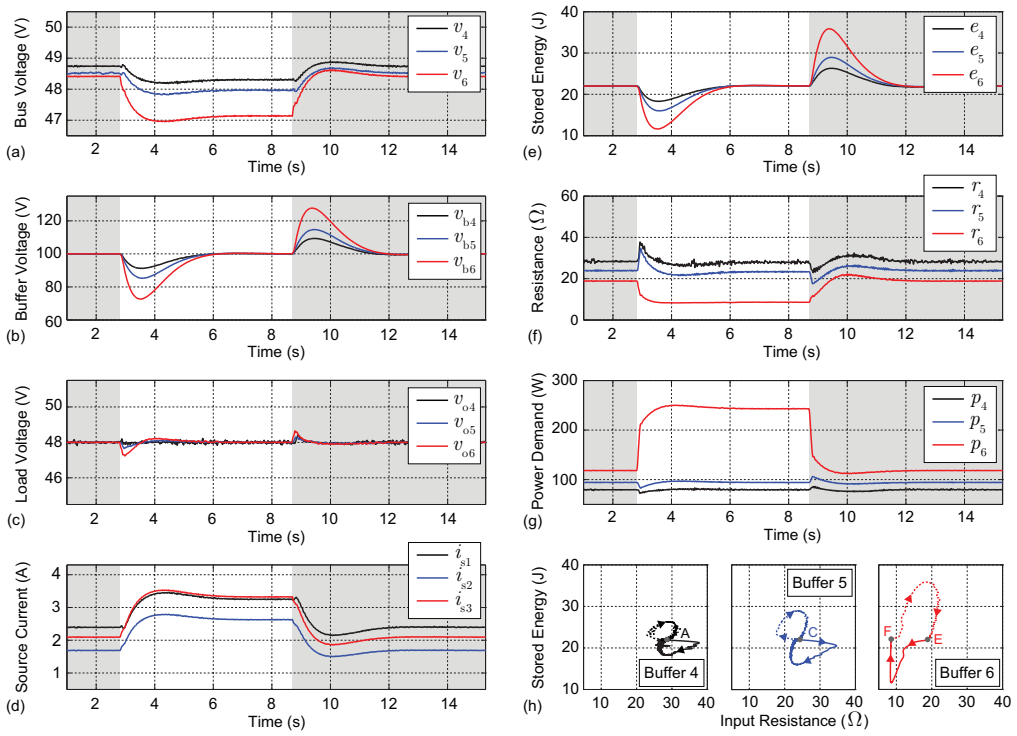

Figure 5-9 Controller performance in response to the load change at terminal 6; multiple assisting neighbors: (a) microgrid bus voltages at the load terminals, (b) output voltage of the power buffers, (c) output voltage across the resistive loads, (d) source currents, (e) stored energy in power buffers, (f) input impedance of the power buffers, (g) output of the active loads, (h) energy-impedance trajectories of the power buffers during the load transient.

All buffers contribute by using their stored energy to smoothen the impedance profile. Figures 5-9(b) and 5-9(e) show how the buffers spend their energy asset during the load transient. The energy-impedance trajectories in Fig. 5-9(h) exhibit movements for all buffers. During the load transient, buffers 4 and 5 start from points A and C in Fig. 5-9(h), respectively, and assist buffer 6 by losing their energy and increasing their

impedance. They regain their energy shortly and move back to the starting condition, i.e., points A and C. Buffer 6, the primary buffer in handling the load demand, drops its energy and, at the same time, reduces its impedance to respond to the load transient. After reaching the desired impedance level, it slightly absorbs more power to restore its initial energy level. In contrast, with no buffering effect, buffer 6 trajectory would have travelled a straight path from point E to point F (see Fig. 5-7(h)). The load at bus 6 is changed back to $20\ \Omega$ At $t = 8.7\ \mathrm{s}$ and, accordingly, the energy-impedance trajectory for the buffer in load 6 travels back to point E. The dashed lines in Fig. 5-9(h) show the trajectories when the load changes back to $20\ \Omega$.

5.5. Summary

Loads in a DC microgrid can be augmented with power buffers to form active loads. A dynamic model of the active loads is derived that accounts for the physical coupling through the distribution system. Proper adjustment of the energy level of the power buffers is shown to help shape transient power demanded from the distribution network. Group assistance of the power buffers is proposed to shape transient power demand. To group the loads, a communication network is considered that enables data exchange. Such group information helps to collectively respond to any load change by exploiting all energy reservoirs in the close vicinity of the consumption terminal that faces the load changes. A cooperative distributed controller is proposed that processes local and neighbor measurements and, accordingly, adjusts the energy level of the buffers to assist the transient load demand. Hardware-in-the-Loop (HIL) studies on a low-voltage DC microgrid validated efficacy of the proposed controller.

Chapter 6

Distributed Economic Dispatch for DC Distribution Networks

Economic dispatch is one of the most important studies in the power system realm. It seeks to coordinate sources to meet the total power demand while minimizing the total generation cost [227]–[231]. This is naturally a nonlinear optimization problem with solutions based on Lagrange multipliers theory [232], dynamic programming [233], or evolutionary algorithms [234]. These approaches are commonly implemented in a supervisory controller, called the *tertiary* controller, which handles communication, processing, and transmitting the decision to the sources. This central command unit is a data fusion and processing center that requires complex communication infrastructure and intricate computational machinery and poses a reliability concern [235]. In addition, prior knowledge of the system dynamics and load forecast is essential to the operation of the economic dispatch.

Decentralized and distributed control approaches are introduced in the literature to handle economic dispatch with distributed computational units across the distribution grid. Limited message passing among these controller help to global coordination and economic dispatch. A distributed auction-based algorithm is presented in [236]. The consensus-based economic dispatch in [237] handles the supply-demand mismatch due to the transmission losses. Decentralized and scalable economic dispatch solutions for small-scale power systems are also discussed in [238]–[239]. Majority of such efforts, however, focus on AC distribution systems and less attention is given to the DC distribution systems. Such distribution systems are rising in popularity given the improved efficiency and simpler control compared to the AC distribution network. This chapter focuses on developing a distributed control framework to handle economic dispatch in DC microgrids.

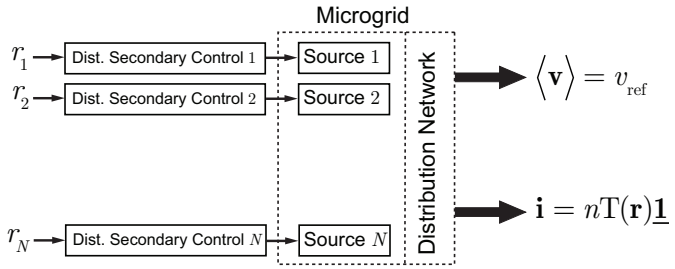

Figure 6-1 Model of a DC microgrid with the secondary controllers introduced in [240]–[241].

It uses a distributed secondary/primary control introduced in [240]–[241] that handles load sharing among DC sources in proportion to a given ratio, called the loading ratio, as shown in Fig. 6-1. By adjusting the loading ratios, one can reroute the power flow from the costly sources to cheaper ones. The proposed controller measures its local incremental cost and compares it with its neighbors' on the communication graph. It then adjusts its local loading ratio to mitigate any discrepancy among the neighbor incremental costs. Through cooperation among controllers, they collectively synchronize the incremental costs across all sources and, thus, provide the optimal economic dispatch.

6.1. Proposed Control Methodology

The proposed two-tier control structure for a DC system is shown in Fig. 6-2. As seen, the tertiary controllers exchange data in a distributed communication network. Through processing local and neighbor data, the controllers decide appropriate loading ratios, r_is, which synchronizes the incremental costs.

6.1.1. Preliminary of Graph Theory

From the control perspective, a multi-agent cyber-physical system can be expressed with a graphical representation with active agents (sources) modeled as nodes of the graph and communication links mapped to edges connecting nodes.

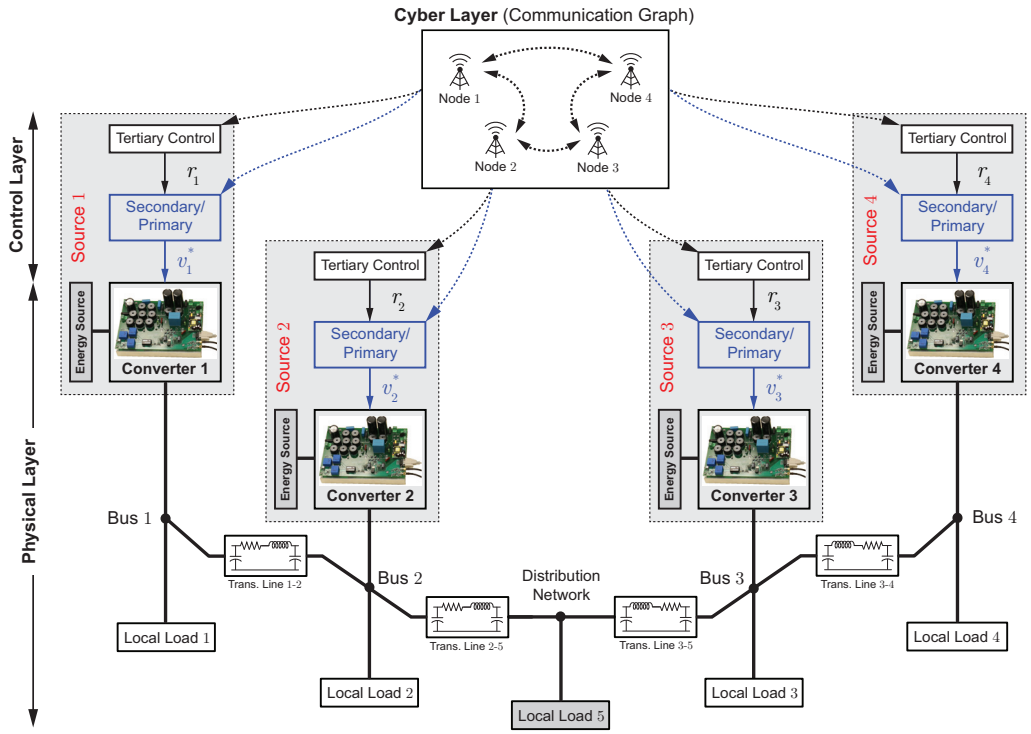

Figure 6-2 Schematic of a DC microgrid with two-tier distributed control structure. The controllers communicate through a distributed data network.

Communication links may not be reciprocal, forming a directed graph (digraph). Each node and edge inherit the dynamic model of the corresponding agent and communication channel, respectively. Information links may exchange data with different gains referred to as the *communication weights*. For example, if Node j broadcasts data Ψ_j to Node i through a link with a designated weight of $a_{ij} > 0$, then, the information received at Node i is $a_{ij}\Psi_j$. Generally, $a_{ij} > 0$ if Node i receives data from Node j and $a_{ij} = 0$, otherwise. Such a graph is usually represented by an associated adjacency matrix $\mathbf{A}_\mathbf{G} = \left[a_{ij}\right] \in \mathbb{R}^{N\times N}$ that carries the communication weights, where N is the number of dispatchable sources.

N_i denotes the set of all neighbors of Node i. The in-degree and out-degree matrices $\mathbf{D}^{\text{in}} = \text{diag}\{d_i^{\text{in}}\}$ and $\mathbf{D}^{\text{out}} = \text{diag}\{d_i^{\text{out}}\}$ are diagonal matrices with $d_i^{\text{in}} = \sum_{j \in N_i} a_{ij}$ and $d_i^{\text{out}} = \sum_{i \in N_j} a_{ji}$, respectively. The Laplacian matrix is defined as $\mathbf{L} \triangleq \mathbf{D}^{\text{in}} - \mathbf{A}_{\mathbf{G}}$, whose eigenvalues determine the global dynamics of the entire system (i.e., the microgrid) [242]–[244]. The Laplacian matrix is balanced if the in-degree and out-degree matrices are equal; particularly, an undirected (bidirectional) data network satisfies this requirement. A direct path from Node i to Node j is a sequence of edges that connects the two nodes. A digraph is said to have a spanning tree if it contains a root node, from which, there exists at least a direct path to every other node. Here, a graph is called to carry the *minimum redundancy* if it contains enough redundant links that, in the case of any single link failure, it remains connected and presents a balanced Laplacian matrix.

6.1.2. Controller Functionality

Figure 6-3 explains functionality of the controller. Prior to activating the controller, all loading ratios are equal and $r_i = 1$. The controllers use a sparse communication network, with Adjacency matrix $\mathbf{A}_{\mathbf{G}}$, to exchange data. It should be noted that the communication graph must carry at least a spanning tree and present a balanced Laplacian matrix. Once the controller is activated, each controller, e.g., the one at Node i, compares its local incremental cost with its neighbors and, accordingly, updates its local loading ratio, r_i. The controller measures its local current, i_i, and then calculates the local incremental cost associated to this supplied current, λ_i. The controller then calculates the neighborhood mismatch, δ_i,

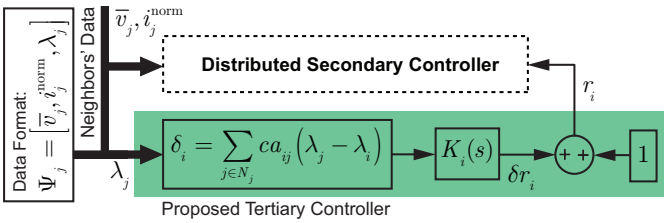

Figure 6-3 Functionality of the proposed tertiary controller.

$$\delta_i = \sum_{j \in N_i} ca_{ij}\left(\lambda_j - \lambda_i\right) \tag{6.1}$$

This mismatch term is fed to a PI controller, $K_i(s)$, to generate the ratio correction term, δr_i, that helps adjust the loading ratio and mitigate the neighborhood mismatch, δ_i. The coefficient c is a design parameter that adjusts the convergence speed. a_{ij} represents the communication weight from Node j to Node i. For appropriate choice of controller gains and communication weights the controllers would collectively synchronize the incremental costs and, thus, satisfy the optimal economic dispatch.

6.1.3. Dynamic Analysis

As shown in Fig. 6-1, a DC microgrid with the secondary/primary controller presented in [240]–[241] is a physical system that shares the load among sources in proportion to the loading ratios, i.e.,

$$\mathbf{i} = n\mathrm{T}\left(\mathbf{r}\right)\underline{\mathbf{1}} \tag{6.2}$$

where $\mathbf{i} = [i_1, i_2, \cdots, i_N]^{\mathsf{T}}$, n is a positive scalar, $\mathbf{r} = [r_1, r_2, \cdots, r_N]^{\mathsf{T}}$, and $\underline{\mathbf{1}}$ is a vector whose elements are one. $\mathrm{T}(\cdot)$:$\mathbb{R}^{N\times 1} \rightarrow \mathbb{R}^{N\times N}$ is a transformation that maps a vector to a diagonal matrix,

$$\mathrm{T}\left(\left[x_1, x_2, \cdots, x_N\right]^{\mathsf{T}}\right) \triangleq \mathrm{diag}\left\{x_1, x_2, \cdots, x_N\right\}. \tag{6.3}$$

N is the number of dispatchable sources.

The generation cost profiles are commonly represented with 2nd-order polynomials, that is

$$C_i(i_i) = \alpha_i + \beta_i i_i + \gamma_i i_i^2. \tag{6.4}$$

As oppose to AC systems, in the DC systems the supplied current, i_i, linearly represents the generated active power, p_i, and, thus, the cost function in (6.4) is formulated based on the supplied current, i_i. The incremental cost for Source i is

$$\lambda_i \triangleq \frac{\mathrm{d}C_i}{\mathrm{d}i}(i_i) = \beta_i + 2\gamma_i i_i \tag{6.5}$$

or, in the matrix format,

$$\boldsymbol{\lambda} = \boldsymbol{\beta} + 2\boldsymbol{\gamma}\mathbf{i} \tag{6.6}$$

where $\boldsymbol{\lambda} = \left[\lambda_1, \lambda_2, \cdots, \lambda_N\right]^{\mathsf{T}}$, $\boldsymbol{\beta} = \left[\beta_1, \beta_2, \cdots, \beta_N\right]^{\mathsf{T}}$, $\mathbf{i} = \left[i_1, i_2, \cdots, i_N\right]^{\mathsf{T}}$, and $\boldsymbol{\gamma} = \mathrm{diag}\{\gamma_1, \gamma_2, \cdots, \gamma_N\}$. Accordingly, one can represent the neighborhood mismatch term in (6.1) in the matrix format as

$$\boldsymbol{\delta} = -c\mathbf{L}\boldsymbol{\lambda} \tag{6.7}$$

where $\boldsymbol{\delta} = \left[\delta_1, \delta_2, \cdots, \delta_N\right]^{\mathsf{T}}$. Plugging (6.6) into (6.7) yields

$$\boldsymbol{\delta} = -c\mathbf{L}\left(\boldsymbol{\beta} + 2\boldsymbol{\gamma}\mathbf{i}\right) \tag{6.8}$$

or, in the frequency domain,

$$\boldsymbol{\Delta} = -c\mathbf{L}\left(\boldsymbol{\beta} + 2\boldsymbol{\gamma}\mathbf{I}\right) \tag{6.9}$$

where $\boldsymbol{\Delta}$ and $\mathbf{I}$ are the Laplace transforms of $\boldsymbol{\delta}$ and $\mathbf{i}$, respectively. The global dynamic behavior of the proposed controller in Fig. 6-3 can be modeled as

$$\mathbf{K}(s)\boldsymbol{\Delta} + \frac{\mathbf{1}}{s} = \mathbf{R} \tag{6.10}$$

where $\mathbf{K}(s) = \mathrm{diag}\left\{K_1(s), K_2(s), \cdots, K_N(s)\right\}$ is the controller matrix and $\mathbf{R}$ is the Laplace transform of the loading ratio vector $\mathbf{r} = \left[r_1, r_2, \cdots, r_N\right]^{\mathsf{T}}$. Plugging (6.9) in (6.10)

$$-c\mathbf{K}(s)\mathbf{L}\left(\boldsymbol{\beta} + 2\boldsymbol{\gamma}\mathbf{I}\right) + \frac{\underline{\underline{\mathbf{1}}}}{s} = \mathbf{R} \tag{6.11}$$

On the other hand, (6.2) can be presented as

$$\mathbf{I} = n\mathrm{T}\left(\mathbf{R}\right)\underline{\mathbf{1}} \tag{6.12}$$

in the frequency domain. Substituting the $\mathbf{R}$ from (6.11) in (6.12)

$$\mathbf{I} = n\mathrm{T}\left(-c\mathbf{K}(s)\mathbf{L}\left(\boldsymbol{\beta} + 2\boldsymbol{\gamma}\mathbf{I}\right) + \frac{\underline{\underline{\mathbf{1}}}}{s}\right)\underline{\mathbf{1}}. \tag{6.13}$$

One can investigate properties of the T transformation. For any diagonal matrix $\mathbf{X}$ and vectors $\mathbf{a}$ and $\mathbf{b}$,

$$\mathrm{T}\left(\mathbf{X}\mathbf{a} + \mathbf{b}\right) = \mathbf{X}\mathrm{T}\left(\mathbf{a}\right) + \mathrm{T}\left(\mathbf{b}\right) \tag{6.14}$$

and

$$\mathrm{T}\left(\mathbf{a}\right)\underline{\mathbf{1}} = \mathbf{a}. \tag{6.15}$$

Given the properties in (6.14)-(6.15), one can simplify (6.13),

$$\mathbf{I} = -n\left(c\mathbf{K}(s)\mathbf{L}\left(\boldsymbol{\beta} + 2\boldsymbol{\gamma}\mathbf{I}\right) - \frac{\underline{\underline{\mathbf{1}}}}{s}\right) \tag{6.16}$$

or, equivalently,

$$\left(\mathbf{I}_N + 2cn\mathbf{K}(s)\mathbf{L}\boldsymbol{\gamma}\right)\mathbf{I} = -n\left(c\mathbf{K}(s)\mathbf{L}\boldsymbol{\beta} - \frac{\underline{\underline{\mathbf{1}}}}{s}\right) \tag{6.17}$$

where $\mathbf{I}_N$ is the identity matrix. This equation represents the dynamic response of the entire microgrid with the proposed tertiary controller and helps to tune the coefficient c and the controllers $K_i(s)$ to achieve a stable system with satisfactory convergence speed.

6.2. Case Study

A $48\ \mathrm{V}$ DC distribution network, with the schematic shown in Fig. 6-2, is considered to study the performance of the proposed controller. Four sources in this system collectively supply one remote and four local loads through a resistive-inductive distribution system. Each source is a rectified voltage source driven by a buck converter that features two-tier control structure. The lower tier, the secondary/primary controller, uses the cooperative control approach introduced in [240]–[241] to tune the bus voltages and acquire desired load sharing. The inputs to these controllers are the loading ratios, r_i s, to which proportion the controllers share the load among sources. The upper tier, the proposed tertiary controller, assigns appropriate loading ratios, r_is, to synchronize the incremental costs of the sources (generation units) and, thus, satisfy the optimal economic dispatch. Physical and control parameters of the underlying system is provided in the Appendix H.

The communication network, described in Fig. 6-2, uses a ring structure with bidirectional links. This network carries spanning trees and features a balanced Laplacian matrix and, thus, is a suitable choice for this study. Adjacency matrix of the communication graph is provided in the Appendix H.

Four different generation cost curves (see Fig. 6-4) are chosen for the sources. Second-order polynomials are used to generate the curves. These polynomials are provided in the Appendix H.

Figure 6-5 demonstrates the simulation results of the system. The tertiary controller was disabled for $t < 1.5\ \mathrm{s}$ and, thus, all the loading ratios were one. Therefore the secondary/primary controllers have managed to equally share the total power demand among sources.

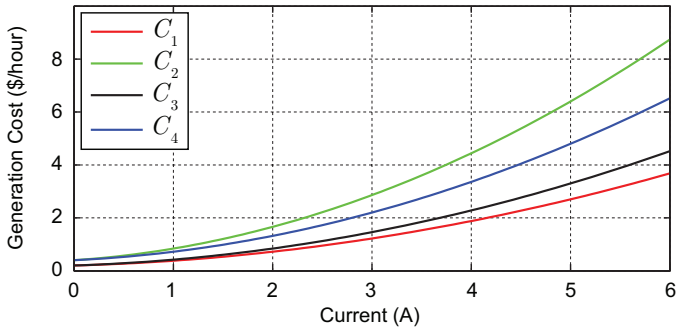

Figure 6-4 Generation cost curves for sources of the underlying DC microgrid.

One can see in Fig. 6-5 (c) that the supplied currents match for $t < 1.5$ s. However, as can be seen in Fig. 6-5(b), the sources are operating at different incremental cost values, i.e., different λ_i s, and therefore the microgrid is working under a non-optimal condition. The proposed controller has been activated at $t = 1.5$ s. It can be seen in Fig. 6-5(c) that the controller has effectively rerouted the power flow from costly sources to the cheaper sources to reduce the total generation cost. Figure 6-5(b) shows that the controller has successfully synchronized the incremental costs and, accordingly, minimized the total generation cost, as exhibited in Fig. 6-5(d). Performance of the controller in response to step load change is studied when the remote load is changed at $t = 4$ s from $12\ \Omega$ to $20\ \Omega$. It is shown in Fig. 6-5(c) that the controller has preserved synchrony of the incremental cost of the sources to secure optimal dispatch.

6.3. Summary

Distributed Economic dispatch for DC distribution systems is studied. The proposed controller measures the local incremental cost and compares it with its neighbors' to adjust its local loading ratio. Collectively, the controllers synchronize the incremental costs of the generation units across the microgrid and, thus, provide an optimal dispatch. Simulation results verify the performance of the proposed controller.

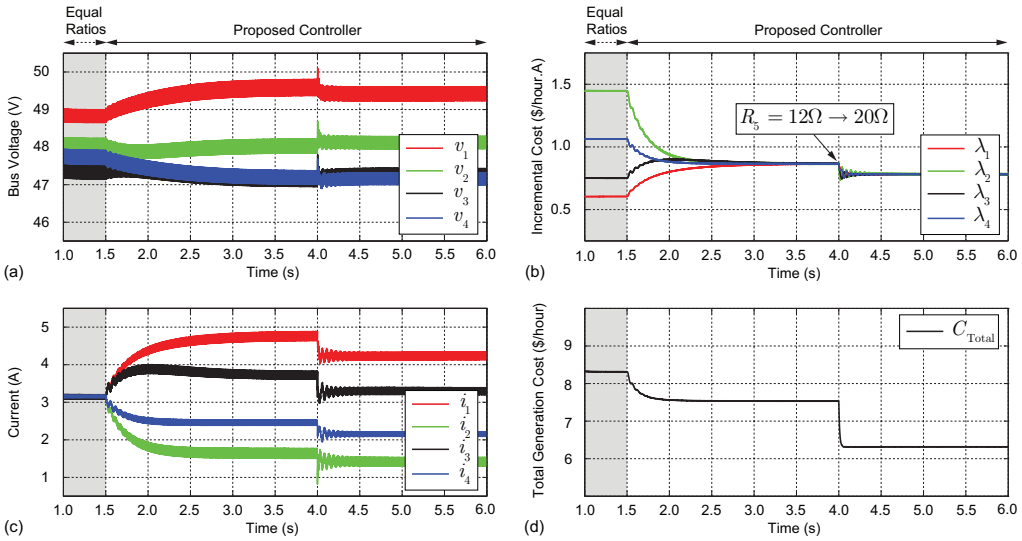

Figure 6-5 Simulation results of the underlying DC microgrid: a) bus voltages across the system, b) lincremental costs for individual sources, c) supplied currents, d) total generation cost.

Future extensions of this work will consider experimental verifications and improvement of the control policy to handle non-convex cost functions.

Chapter 7

Conclusion and Future Works

This work offered alternative distributed control structures to improve microgrid reliability and help to the scalability of the power system. The research outcomes are outlined below:

- A cooperative distributed control policy is proposed that handles global voltage regulation and proportional load sharing in DC microgrids. A distributed adaptive droop control is offered as an alternative solution for distributed primary/secondary control for DC microgrids.

- A droop-free distributed control methodology is developed that secures primary/secondary control requirements of AC microgrids . It features a novel approach that handles frequency regulation without using any frequency measurement and, thus, provides a faster frequency regulation.

- A Distributed load demand management is explored for DC microgrids. It enhances loads into active loads by adding power buffers. A distributed controller is used to manage transient energy profile of the buffers and, accordingly, shape the transient power demanded from the distribution network.

- Distributed tertiary controller for managing economic dispatch is studied. A distributed protocol is proposed that regulates the incremental costs for all sources across the microgrid and, thus, provides the economic distapch.

Future works may focus on developing distributed protocols for securing economic dispatch in AC systems. Further research may direct toward exploring

distributed optimization protocols for non-convex cost functions in both DC and AC microgrids.

Appendix A

Dynamic Consensus

Following lemmas need to be studied before studying the dynamic consensus:

Lemma A.1 [54]: Assume that the digraph $\mathbf{G}$ has a spanning tree. Then, the Laplacian matrix $\mathbf{L}$ has a simple eigen-value at the origin, i.e., $\lambda_1 = 0$, and other eigen-values lie in the Open Right Hand Plane (ORHP). In addition,

$$\lim_{t\to\infty} e^{-\mathbf{L}t} = w_r w_l^{\mathrm{T}}, \tag{A.1}$$

where $w_r \in \mathbb{R}^{N\times 1}$ and $w_l^{\mathrm{T}} \in \mathbb{R}^{N\times 1}$ are the right and left eigen-vectors of $\mathbf{L}$ associated with $\lambda_1 = 0$, respectively. It should be noted that w_l^{T} should be normalized with respect to w_r, i.e., $w_l^{\mathrm{T}} w_r = 1$.

Lemma A.2: Assume that the digraph $\mathbf{G}$ has a spanning tree and the Laplacian matrix, $\mathbf{L}$, is balanced. Then,

$$\lim_{s\to 0} s(s\mathbf{I}_N + \mathbf{L})^{-1} = \mathbf{Q}. \tag{A.2}$$

$$\lim_{s\to 0} \mathbf{L}(s\mathbf{I}_N + \mathbf{L})^{-1} = \lim_{s\to 0} (s\mathbf{I}_N + \mathbf{L})^{-1}\mathbf{L} = \mathbf{I}_N - \mathbf{Q}. \tag{A.3}$$

where $\mathbf{Q}$ is the averaging matrix defined in Subsection 2.3.1.

Proof of Lemma A.2: Assume a linear system of $\dot{\mathbf{x}} = -\mathbf{L}\mathbf{x}$ with $\mathbf{x}(0) \neq 0$ and $\mathbf{x} \in \mathbb{R}^{N\times 1}$. One can write,

$$\mathbf{x}(t) = e^{-\mathbf{L}t}\mathbf{x}(0). \tag{A.4}$$

Or, equivalently, in the frequency domain,

$$\mathbf{X} = (s\mathbf{I}_N + \mathbf{L})^{-1}\mathbf{x}(0). \tag{A.5}$$

Lemma A.1 ensures that $\mathbf{X}$ is a type 1 vector, i.e., it has a single pole at the origin and all other poles lie in the OLHP. Thus, using the final value theorem,

$$\lim_{t\to\infty} \mathbf{x}(t) = \lim_{s\to 0} s\mathbf{X} = \left(\lim_{s\to 0} s(s\mathbf{I}_N + \mathbf{L})^{-1}\right)\mathbf{x}(0). \tag{A.6}$$

On the other hand, by using Lemma A.1, (A.4) yields to,

$$\lim_{t\to\infty} \mathbf{x}(t) = \left(\lim_{t\to\infty} e^{-\mathbf{L}t}\right)\mathbf{x}(0) = w_r w_l^{\mathrm{T}}\mathbf{x}(0). \tag{A.7}$$

For any Laplacian matrix $\mathbf{L}$ all row sums are equal to zero. Thus, $w_r = \underline{\mathbf{1}}$. In addition, for any balanced $\mathbf{L}$, all column sums are also equal to zero. Thus, $w_l = (1/N)\underline{\mathbf{1}}$. Accordingly, (A.7) implies that,

$$\lim_{t\to\infty} \mathbf{x}(t) = \mathbf{Q}\mathbf{x}(0). \tag{A.8}$$

Comparing (A.6) to (A.8),

$$\left(\lim_{s\to 0} s(s\mathbf{I}_N + \mathbf{L})^{-1}\right)\mathbf{x}(0) = \mathbf{Q}\mathbf{x}(0). \tag{A.9}$$

Since (A.9) holds for all $\mathbf{x}(0) \neq 0$, one may conclude (A.2). In addition,

$$\mathbf{I}_N = \lim_{s\to 0}(s\mathbf{I}_N + \mathbf{L})(s\mathbf{I}_N + \mathbf{L})^{-1} = \lim_{s\to 0} s(s\mathbf{I}_N + \mathbf{L})^{-1} + \lim_{s\to 0} \mathbf{L}(s\mathbf{I}_N + \mathbf{L})^{-1}. \tag{A.10}$$

Comparing (A.2) with (A.10) concludes (A.3).

Theorem A.1: Assume that the communication graph $\mathbf{G}$, used in a cooperative control system, has a spanning tree and the associated Laplacian matrix, $\mathbf{L}$, is balanced. Then, using the observer in (2.7), all the estimated averages in $\overline{\mathbf{v}}$ converge to the true global average voltage.

Proof of Theorem A.1: Equation (2.34) shows the global dynamic of the microgrid, when the proposed controller is effective. It is assumed that the system parameters are, accordingly, designed to stabilize the microgrid. Thus, the resulting voltage vector, $\mathbf{V}$, is a type 1 vector. Based on Lemma A.1, all poles of the term $s(s\mathbf{I}_N + \mathbf{L})^{-1}$ lie in the OLHP. It should be noted that if λ_i is an eigen-value of $\mathbf{L}$ then, $s = -\lambda_i$ is a pole of $s(s\mathbf{I}_N + \mathbf{L})^{-1}$. The term s in $s(s\mathbf{I}_N + \mathbf{L})^{-1}$ cancels the pole of $(s\mathbf{I}_N + \mathbf{L})^{-1}$ at the origin. Thus, (2.7) implies that $\overline{\mathbf{v}}$ is also a type 1 vector. Since both $\mathbf{V}$ and $\overline{\mathbf{v}}$ are type 1, one may use the final value theorem,

$$\lim_{t\to\infty} \overline{\mathbf{v}}(t) = \lim_{s\to 0} s\overline{\mathbf{V}} = \lim_{s\to 0} s(s\mathbf{I}_N + \mathbf{L})^{-1}(s\mathbf{V}). \tag{A.11}$$

Using Lemma A.2,

$$\lim_{t\to\infty}\overline{\mathbf{v}}(t)=\lim_{s\to 0}s(s\mathbf{I}_{N}+\mathbf{L})^{-1}\times\lim_{s\to 0}(s\mathbf{V})=\mathbf{Q}\times\lim_{t\to\infty}\mathbf{v}=\mathbf{Q}\,\mathbf{v}^{ss}=\left\langle\mathbf{v}^{ss}\right\rangle\underline{\mathbf{1}}. \tag{A.12}$$

Equation (A.12) implies that all estimations converge to the true global average voltage. In other words,

$$\forall i:0\le i\le N,\quad \lim_{t\to\infty}\overline{v}_{i}(t)=\frac{1}{N}\sum_{i=1}^{N}v_{i}(t). \tag{A.13}$$

Appendix B

Analysis of the Noise Cancellation Module

Following lemmas need to be studied before analyzing the noise cancellation module:

Lemma B.1: For a given matrix $\mathbf{A} \in \mathbb{R}^{N\times N}$, if $\mathbf{I}_N + \mathbf{A}$ is invertible then,

$$(\mathbf{I}_N + \mathbf{A})^{-1} = \mathbf{I}_N - \mathbf{A}(\mathbf{I}_N + \mathbf{A})^{-1} = \mathbf{I}_N - (\mathbf{I}_N + \mathbf{A})^{-1}\mathbf{A}. \tag{B.1}$$

Proof of Lemma B.1: For a given matrix $\mathbf{A} \in \mathbb{R}^{N\times N}$,

$$(\mathbf{I}_N + \mathbf{A})^{-1} = (\mathbf{I}_N + \mathbf{A})^{-1}(\mathbf{I}_N + \mathbf{A}) - (\mathbf{I}_N + \mathbf{A})^{-1}\mathbf{A} = \mathbf{I}_N - (\mathbf{I}_N + \mathbf{A})^{-1}\mathbf{A}. \tag{B.2}$$

Lemma B.2: For a given invertible matrix $\mathbf{A} \in \mathbb{R}^{N\times N}$ if $\mathbf{I}_N + \mathbf{A}$ is invertible then,

$$(\mathbf{I}_N + \mathbf{A}^{-1})^{-1} = \mathbf{A}(\mathbf{I}_N + \mathbf{A})^{-1} = (\mathbf{I}_N + \mathbf{A})^{-1}\mathbf{A}. \tag{B.3}$$

Proof of Lemma B.2: For a given invertible matrix $\mathbf{A}$,

$$(\mathbf{I}_N + \mathbf{A}^{-1})^{-1} = (\mathbf{A}\mathbf{A}^{-1} + \mathbf{A}^{-1})^{-1} = \left((\mathbf{I}_N + \mathbf{A})\mathbf{A}^{-1}\right)^{-1} = \mathbf{A}(\mathbf{I}_N + \mathbf{A})^{-1}. \tag{B.4}$$

Lemma B.3: If $\mathbf{L}$ is a balanced Laplacian matrix, $b>0$, and $\mathbf{K} = \mathrm{diag}\{k_i\}$ has positive diagonal elements then, $\mathbf{L}' = b\mathbf{L}\mathbf{K}^{-1}\mathbf{L}$ is a balanced Laplacian matrix.

Proof of Lemma B.3: The matrix $\mathbf{L}$ is said to be a Laplacian matrix if a communication graph exists with the associated Laplacian matrix $\mathbf{L}$. Equivalently, a matrix is a Laplacian matrix if and only if $\mathbf{L}\underline{1} = \mathbf{0}$. A Laplacian matrix is balanced if it has all column-sums of zero, i.e., $\underline{1}^{\mathrm{T}}\mathbf{L} = \mathbf{0}$. Let $\mathbf{L}$ be a balanced Laplacian matrix and $\mathbf{L}' = b\mathbf{L}\mathbf{K}^{-1}\mathbf{L}$ then,

$$\mathbf{L}'\underline{1} = b\mathbf{L}\mathbf{K}^{-1}\left(\mathbf{L}\underline{1}\right) = \mathbf{0}, \tag{B.5}$$

which implies that $\mathbf{L}'$ is a Laplacian matrix. On the other hand,

$$\underline{1}^{\mathrm{T}}\mathbf{L}' = b\left(\underline{1}^{\mathrm{T}}\mathbf{L}\right)\mathbf{K}^{-1}\mathbf{L} = \mathbf{0}, \tag{B.6}$$

which shows that $\mathbf{L}'$ is also balanced.

Lemma B.4: If $\mathbf{L}$ is a balanced Laplacian matrix, $b>0$, and $\mathbf{K} = \mathrm{diag}\{k_i\}$ has positive diagonal elements then,

$$\lim_{s\to 0} s\left(s\mathbf{I}_N + (s\mathbf{I}_N + b\mathbf{L})\mathbf{K}^{-1}(s\mathbf{I}_N + \mathbf{L})\right)^{-1} = \mathbf{Q}. \tag{B.7}$$

$$\lim_{s\to 0}\left(\mathbf{I}_N + s(s\mathbf{I}_N + \mathbf{L})^{-1}\mathbf{K}(s\mathbf{I}_N + b\mathbf{L})^{-1}\right)^{-1} = \mathbf{I}_N - \mathbf{Q}. \tag{B.8}$$

Proof of Lemma B.4: Let $\mathbf{L}$ be a balanced Laplacian matrix, $b>0$, and $\mathbf{K}=\mathrm{diag}\{k_i\}$ has positive diagonal elements. Then,

$$\lim_{s\to 0}\left((s\mathbf{I}_N + b\mathbf{L})\mathbf{K}^{-1}(s\mathbf{I}_N + \mathbf{L})\right) = b\mathbf{L}\mathbf{K}^{-1}\mathbf{L}. \tag{B.9}$$

Let's define $\mathbf{L}' = b\mathbf{L}\mathbf{K}^{-1}\mathbf{L}$. Then, using (B.9),

$$\lim_{s\to 0} s\left(s\mathbf{I}_N + (s\mathbf{I}_N + b\mathbf{L})\mathbf{K}^{-1}(s\mathbf{I}_N + \mathbf{L})\right)^{-1} = \lim_{s\to 0} s\left(s\mathbf{I}_N + \mathbf{L}'\right)^{-1}. \tag{B.10}$$

Lemma B.3 ensures that $\mathbf{L}'$ is a balanced Laplacian matrix. Therefore, by applying Lemma A.2 (Equation (A.2)), one can write $\lim_{s\to 0} s(s\mathbf{I}_N + \mathbf{L}')^{-1} = \mathbf{Q}$, which, together with (B.10), proves (B.7).

To study the second part of the Lemma, i.e., (B.8), one may note that for $s\neq 0$, $s\mathbf{I}_N + b\mathbf{L}$ is invertible [63]. $\mathbf{K}$ is also invertible and $\mathbf{K}^{-1}=\mathrm{diag}\{k_i^{-1}\}$. Let's define,

$$\Gamma \triangleq \left(\mathbf{I}_N + s(s\mathbf{I}_N + \mathbf{L})^{-1}\mathbf{K}(s\mathbf{I}_N + b\mathbf{L})^{-1}\right)^{-1}. \tag{B.11}$$

Using Lemma B.1,

$$\Gamma = \mathbf{I}_N - s(s\mathbf{I}_N + \mathbf{L})^{-1}\mathbf{K}(s\mathbf{I}_N + b\mathbf{L})^{-1}\left(\mathbf{I}_N + s(s\mathbf{I}_N + \mathbf{L})^{-1}\mathbf{K}(s\mathbf{I}_N + b\mathbf{L})^{-1}\right)^{-1}. \tag{B.12}$$

Lemma B.2 offers to further expand (B.12),

$$\begin{aligned}\Gamma &= \mathbf{I}_N - s(s\mathbf{I}_N + \mathbf{L})^{-1}\mathbf{K}(s\mathbf{I}_N + b\mathbf{L})^{-1}\frac{1}{s}(s\mathbf{I}_N + b\mathbf{L})\mathbf{K}^{-1}(s\mathbf{I}_N + \mathbf{L})\times \\ &\qquad\qquad \left(\mathbf{I}_N + \frac{1}{s}(s\mathbf{I}_N + b\mathbf{L})\mathbf{K}^{-1}(s\mathbf{I}_N + \mathbf{L})\right)^{-1} \\ &= \mathbf{I}_N - s\left(s\mathbf{I}_N + (s\mathbf{I}_N + b\mathbf{L})\mathbf{K}^{-1}(s\mathbf{I}_N + \mathbf{L})\right)^{-1}.\end{aligned} \tag{B.13}$$

By applying Lemma B.4 (Equation (B.7)) to (B.13) one can conclude $\lim_{s\to 0}\Gamma = \mathbf{I}_N - \mathbf{Q}$.

Theorem B.1: Assume that the communication graph $\mathbf{G}$, used in a distributed control system, has a spanning tree, and the associated Laplacian matrix, $\mathbf{L}$, is balanced.

Then, using the total observer in (2.21)–(2.23), all the estimated averages in $\overline{\mathbf{v}}$ converge to the true global average voltage average.

Proof of Theorem B.1: For any $s \neq 0$, $\left(s\mathbf{I}_N + b\mathbf{L}\right)$ is invertible [63]. The integrator gain matrix, $\mathbf{K}$, is also invertible and $\mathbf{K}^{-1} = \mathrm{diag}\{k_i^{-1}\}$. Thus, one can safely reformulate the total observer transfer function as,

$$\begin{aligned}
\mathbf{H}_{\mathrm{obs}}^{\mathrm{F}} &= \left(\left(s\mathbf{I}_N + \mathbf{L}\right) + s\mathbf{K}\left(s\mathbf{I}_N + b\mathbf{L}\right)^{-1}\right)^{-1}\left(\left(s\mathbf{I}_N + \mathbf{L}\right) + s\mathbf{K}\left(s\mathbf{I}_N + b\mathbf{L}\right)^{-1} - \mathbf{L}\right) \\
&= \mathbf{I}_N - \left(\left(s\mathbf{I}_N + \mathbf{L}\right) + s\mathbf{K}\left(s\mathbf{I}_N + b\mathbf{L}\right)^{-1}\right)^{-1}\mathbf{L} \\
&= \mathbf{I}_N - \left(\left(s\mathbf{I}_N + \mathbf{L}\right)\left(\mathbf{I}_N + s\left(s\mathbf{I}_N + \mathbf{L}\right)^{-1}\mathbf{K}\left(s\mathbf{I}_N + b\mathbf{L}\right)^{-1}\right)\right)^{-1}\mathbf{L} \\
&= \mathbf{I}_N - \left(\mathbf{I}_N + s\left(s\mathbf{I}_N + \mathbf{L}\right)^{-1}\mathbf{K}\left(s\mathbf{I}_N + b\mathbf{L}\right)^{-1}\right)^{-1}\left(s\mathbf{I}_N + \mathbf{L}\right)^{-1}\mathbf{L}
\end{aligned} \tag{B.14}$$

Using Lemma A.2 (Equation (A.3)) and Lemma B.4 (Equation (B.8)), the total observer DC gain can be found,

$$\lim_{s\to 0}\mathbf{H}_{\mathrm{obs}}^{\mathrm{F}} = \mathbf{I}_N - (\mathbf{I}_N - \mathbf{Q})^2 = 2\mathbf{Q} - \mathbf{Q}^2 = \mathbf{Q}. \tag{B.15}$$

Therefore, for type 1 (DC and exponentially damping) disturbances, (2.21) yields to,

$$\begin{aligned}
\lim_{t\to\infty}\overline{\mathbf{v}}(t) &= \lim_{s\to 0}\mathbf{H}_{\mathrm{obs}}^{\mathrm{F}} \times \lim_{s\to 0}(s\overline{\mathbf{V}}) + \lim_{s\to 0}\mathbf{H}_{\mathrm{NC}} \times \lim_{s\to 0}(s\mathbf{D}) \\
&= \mathbf{Q} \times \lim_{t\to\infty}\mathbf{v} + \mathbf{0} = \mathbf{Q}\mathbf{v}^{\mathrm{ss}} = \left\langle \mathbf{v}^{\mathrm{ss}} \right\rangle \underline{\mathbf{1}},
\end{aligned} \tag{B.16}$$

which proves the Theorem B.1.

Appendix C

Microgrid Parameters for Studies in Chapter 2

Each of the underlying buck converters has $L = 2.64\ \mathrm{mH}$ and $C = 2.2\ \mathrm{mF}$ and works with the switching frequency of $F_s = 60\ \mathrm{kHz}$. Transmission lines series impedances are $Z_{12} = Z_{34} = Z_b$ and $Z_{25} = Z_{35} = 2Z_b$, where the base impedance is $Z_b = 0.5 + (50\ \mu\mathrm{H})s$. The circuit model of the line includes $22\ \mathrm{nF}$ of capacitance on either end. Impedances of the local loads are $R_1 = 30\,\Omega$ and $R_2 = R_3 = R_4 = 20\,\Omega$. Voltages of the (rectified) input DC sources are $V_{s1} = V_{s4} = 80\ \mathrm{V}$ and $V_{s2} = V_{s3} = 100\ \mathrm{V}$. The control parameters are as follow:

$$\mathbf{I}_{\mathrm{rated}} = \begin{bmatrix} 6 & 0 & 0 & 0 \\ 0 & 3 & 0 & 0 \\ 0 & 0 & 3 & 0 \\ 0 & 0 & 0 & 6 \end{bmatrix}, \tag{C.1}$$

$$\mathbf{A}_{\mathrm{G}} = \begin{bmatrix} 0 & 90 & 0 & 110 \\ 90 & 0 & 100 & 0 \\ 0 & 100 & 0 & 120 \\ 110 & 0 & 120 & 0 \end{bmatrix}, \quad \mathbf{r} = \begin{bmatrix} 0.5 & 0 & 0 & 0 \\ 0 & 1.0 & 0 & 0 \\ 0 & 0 & 1.0 & 0 \\ 0 & 0 & 0 & 0.5 \end{bmatrix}, \tag{C.2}$$

$$b = 1, \quad c = 0.075, \tag{C.3}$$

$$\mathbf{H}_{\mathrm{P}} = \begin{bmatrix} 0.1 & 0 & 0 & 0 \\ 0 & 0.09 & 0 & 0 \\ 0 & 0 & 0.08 & 0 \\ 0 & 0 & 0 & 0.11 \end{bmatrix}, \quad \mathbf{H}_{\mathrm{I}} = \begin{bmatrix} 6 & 0 & 0 & 0 \\ 0 & 5 & 0 & 0 \\ 0 & 0 & 5.4 & 0 \\ 0 & 0 & 0 & 5.6 \end{bmatrix}, \tag{C.4}$$

$$\mathbf{G}_{\mathrm{P}} = \begin{bmatrix} 1.1 & 0 & 0 & 0 \\ 0 & 1 & 0 & 0 \\ 0 & 0 & 1.2 & 0 \\ 0 & 0 & 0 & 1.1 \end{bmatrix}, \quad \mathbf{G}_{\mathrm{I}} = \begin{bmatrix} 7 & 0 & 0 & 0 \\ 0 & 7.4 & 0 & 0 \\ 0 & 0 & 6.6 & 0 \\ 0 & 0 & 0 & 7 \end{bmatrix}, \tag{C.5}$$

$$\mathbf{K} = \begin{bmatrix} 1 & 0 & 0 & 0 \\ 0 & 2 & 0 & 0 \\ 0 & 0 & 3 & 0 \\ 0 & 0 & 0 & 4 \end{bmatrix}. \tag{C.6}$$

Appendix D

Solution to the Quadratic Equation

Theorem D.1: Assume $\mathbf{L}$ is the Laplacian matrix of a communication graph with at least one spanning tree. If $\mathbf{L}$ is balanced then, the only solution to the quadratic equation $\mathbf{x}^{\mathrm{T}}\mathbf{L}\mathbf{x}=0$ is $\mathbf{x}=k\underline{\mathbf{1}}$, where k is a real number.

Proof of Theorem D.1: The quadratic form, $\mathbf{x}^{\mathrm{T}}\mathbf{L}\mathbf{x}$, is a real number. Thus,

$$\mathbf{x}^{\mathrm{T}}\mathbf{L}\mathbf{x}=\left(\mathbf{x}^{\mathrm{T}}\mathbf{L}\mathbf{x}\right)^{\mathrm{T}}=\mathbf{x}^{\mathrm{T}}\mathbf{L}^{\mathrm{T}}\mathbf{x}=\mathbf{x}^{\mathrm{T}}\left(\frac{\mathbf{L}+\mathbf{L}^{\mathrm{T}}}{2}\right)\mathbf{x}. \tag{D.1}$$

Let's define the co-Laplacian matrix as $\mathbf{L}_{\mathrm{c}}\triangleq\left(\mathbf{L}+\mathbf{L}^{\mathrm{T}}\right)\big/2$, which is a symmetric matrix. Assume $\mathbf{L}=[l_{ij}]\in\mathbb{R}^{N\times N}$ and $\mathbf{L}_{\mathrm{c}}=[l_{ij}^{\mathrm{c}}]\in\mathbb{R}^{N\times N}$. Then,

$$\begin{cases} l_{ii}^{\mathrm{c}}=2l_{ii}\geq 0, \\ l_{ij}^{\mathrm{c}}=l_{ij}+l_{ji}=l_{ji}^{\mathrm{c}}\leq 0, \qquad i\neq j \end{cases} \tag{D.2}$$

Since the Laplacian matrix, $\mathbf{L}$, is balanced,

$$l_{ii}=-\sum_{j\in N_i}l_{ij}=-\sum_{j=1(j\neq i)}^{N}l_{ij}=-\sum_{j=1(j\neq i)}^{N}l_{ji}. \tag{D.3}$$

Accordingly, one can formulate diagonal elements of the co-Laplacian matrix, $\mathbf{L}_{\mathrm{c}}$,

$$l_{ii}^{\mathrm{c}}=-\sum_{j=1(j\neq i)}^{N}\left(l_{ij}+l_{ji}\right)=-\sum_{j=1(j\neq i)}^{N}l_{ij}^{\mathrm{c}}=-\sum_{j=1(j\neq i)}^{N}l_{ji}^{\mathrm{c}}. \tag{D.4}$$

The quadratic equation can be expanded using (D.4)

$$\begin{aligned} \mathbf{x}^{\mathrm{T}}\mathbf{L}\mathbf{x}&=\frac{1}{2}\mathbf{x}^{\mathrm{T}}\mathbf{L}_{\mathrm{c}}\mathbf{x}=\frac{1}{2}\sum_{1\leq i,j\leq N}x_i l_{ij}^{\mathrm{c}}x_j \\ &=\frac{1}{2}\sum_{i=1}^{N}x_i^2 l_{ii}^{\mathrm{c}}+\frac{1}{2}\sum_{i\neq j}x_i l_{ij}^{\mathrm{c}}x_j \\ &=-\frac{1}{2}\sum_{i=1}^{N}\left(\sum_{j=1(j\neq i)}^{N}l_{ij}^{\mathrm{c}}\right)x_i^2+\frac{1}{2}\sum_{i\neq j}x_i l_{ij}^{\mathrm{c}}x_j \\ &=\frac{1}{2}\sum_{i<j}\left(x_i l_{ij}^{\mathrm{c}}x_j-x_i^2 l_{ij}^{\mathrm{c}}-x_j^2 l_{ji}^{\mathrm{c}}+x_j l_{ji}^{\mathrm{c}}x_i\right) \\ &=-\frac{1}{2}\sum_{i<j}l_{ij}^{\mathrm{c}}\left(x_i-x_j\right)^2=0 \end{aligned} \tag{D.5}$$

where $\mathbf{x}=[x_1,x_2,\cdots,x_N]^{\mathrm{T}}$. All off-diagonal entries of the co-Laplacian matrix, $\mathbf{L}_{\mathrm{c}}$, are non-positive. Thus, (D.5) holds if and only if for every two connected nodes, i.e., $a_{ij}>0$, $x_i=x_j$.

The communication graph has a spanning tree and, thus, has a root node, from which there exists a path to every other node. Assume that v_i^g is the root node then, for any other node, v_j^g, one can find a sequence of nodes connecting v_i^g to v_j^g,

$$v_i^g \rightarrow v_k^g \rightarrow \cdots \rightarrow v_l^g \rightarrow v_j^g. \tag{D.6}$$

Given that for every two connected nodes associated entries of the vector $\mathbf{x}$ are equal, one can conclude

$$x_i = x_k = \cdots = x_l = x_j. \tag{D.7}$$

Thus, the vector $\mathbf{x}$ has equal entries, i.e., $\mathbf{x} = k\underline{\mathbf{1}}$, where k is a real number.

Appendix E

Microgrid Parameters for Studies in Chapter 3

Each of the underlying buck converters has $L = 2640\ \mu\mathrm{H}$ and $C = 2.2\ \mathrm{mF}$ and operates with $F_s = 60\ \mathrm{kHz}$ switching frequency. Impedances of the transmission lines are $Z_{12} = Z_{34} = Z_b$ and $Z_{25} = Z_{35} = 2Z_b$, where the base impedance is $Z_b = 0.5 + (50\ \mu\mathrm{H})s$. Impedances of the local loads are $R_1 = 30\,\Omega$ and $R_2 = R_3 = R_4 = 20\,\Omega$. Voltages of the (rectified) input sources are $V_{s1} = V_{s4} = 100\,\mathrm{V}$ and $V_{s2} = V_{s3} = 80\,\mathrm{V}$. The control parameters are as follow,

$$\mathbf{I}_{\mathrm{rated}} = \begin{bmatrix} 6 & 0 & 0 & 0 \\ 0 & 3 & 0 & 0 \\ 0 & 0 & 3 & 0 \\ 0 & 0 & 0 & 6 \end{bmatrix}, \tag{E.1}$$

$$b = 0.5, \tag{E.2}$$

$$\mathbf{H}_{\mathrm{P}} = \begin{bmatrix} 0.1 & 0 & 0 & 0 \\ 0 & 0.1 & 0 & 0 \\ 0 & 0 & 0.1 & 0 \\ 0 & 0 & 0 & 0.1 \end{bmatrix}, \quad \mathbf{H}_{\mathrm{I}} = \begin{bmatrix} 2.5 & 0 & 0 & 0 \\ 0 & 2.5 & 0 & 0 \\ 0 & 0 & 2.5 & 0 \\ 0 & 0 & 0 & 2.5 \end{bmatrix}, \tag{E.3}$$

$$\mathbf{G}_{\mathrm{P}} = \begin{bmatrix} 0.3 & 0 & 0 & 0 \\ 0 & 0.3 & 0 & 0 \\ 0 & 0 & 0.3 & 0 \\ 0 & 0 & 0 & 0.3 \end{bmatrix}, \quad \mathbf{G}_{\mathrm{I}} = \begin{bmatrix} 5 & 0 & 0 & 0 \\ 0 & 5 & 0 & 0 \\ 0 & 0 & 5 & 0 \\ 0 & 0 & 0 & 5 \end{bmatrix}, \tag{E.4}$$

$$\mathbf{A}_{\mathbf{G}} = \begin{bmatrix} 0 & 10 & 0 & 10 \\ 10 & 0 & 10 & 0 \\ 0 & 10 & 0 & 10 \\ 10 & 0 & 10 & 0 \end{bmatrix}, \quad \mathbf{r}_0 = \begin{bmatrix} 0.5 & 0 & 0 & 0 \\ 0 & 1 & 0 & 0 \\ 0 & 0 & 1 & 0 \\ 0 & 0 & 0 & 0.5 \end{bmatrix}. \tag{E.5}$$

Appendix F

Microgrid Parameters for Studies in Chapter 4

DC bus voltages that supply the inverter modules are all $V_{\mathrm{dc}} = 650\ \mathrm{V}$. The filter inductors are identical and $L_{\mathrm{F1}} = L_{\mathrm{F2}} = 1.8\ \mathrm{mH}$, and the intermediate capacitor is $C_{\mathrm{F}} = 25\ \mu\mathrm{F}$. The line impedance connecting busses i and j can be expressed as $Z_{ij} = R_{ij} + sL_{ij}$ where,

$$\begin{cases} R_{12} = 0.8\ \Omega & L_{12} = 3.6\ \mathrm{mH} \\ R_{23} = 0.4\ \Omega & L_{23} = 1.8\ \mathrm{mH}. \\ R_{34} = 0.7\ \Omega & L_{34} = 1.5\ \mathrm{mH} \end{cases} \tag{F.1}$$

The control parameters are,

$$\begin{cases} \mathbf{p}_{\mathrm{rated}} = 1\ \mathrm{kW} \times \mathrm{diag}\{1.6, 1.6, 0.8, 0.8\} \\ \mathbf{q}_{\mathrm{rated}} = 1\ \mathrm{kVAr} \times \mathrm{diag}\{0.6, 0.6, 0.3, 0.3\} \end{cases}, \tag{F.2}$$

$$\mathbf{A}_{\mathbf{G}} = 1.5 \times \begin{bmatrix} 0 & 1 & 0 & 1 \\ 1 & 0 & 1 & 0 \\ 0 & 1 & 0 & 1 \\ 1 & 0 & 1 & 0 \end{bmatrix}, \tag{F.3}$$

$$b = 2, \quad c = 0.02, \tag{F.4}$$

$$\begin{cases} \mathbf{G}_{\mathrm{P}} = 0.01 \times \mathbf{I}_4, & \mathbf{G}_{\mathrm{I}} = 3 \times \mathbf{I}_4 \\ \mathbf{H}_{\mathrm{P}} = 0.005 \times \mathbf{I}_4, & \mathbf{H}_{\mathrm{I}} = 2 \times \mathbf{I}_4 \end{cases}. \tag{F.5}$$

Appendix G

Microgrid Parameters for Studies in Chapter 5

A. Power System Parameter

The underlying microgrid has three DC sources. Each source is modeled as a series connection of a voltage source and an internal resistance,

$$V_{s1} = V_{s2} = V_{s3} = 50 \text{ V}, \tag{G.1}$$

$$r_{s1} = r_{s2} = r_{s3} = 0.1 \ \Omega. \tag{G.2}$$

Sources also carry LC filters with $L = 500 \ \mu\text{H}$ and $C = 2.2 \text{ mF}$. Transmission line impedances are

$$r_{48} = 0.2 \ \Omega, \tag{G.3}$$

$$r_{58} = r_{59} = r_{69} = 0.3 \ \Omega, \tag{G.4}$$

$$r_{18} = 0.35 \ \Omega, \tag{G.5}$$

$$r_{47} = r_{27} = r_{39} = 0.5 \ \Omega, \tag{G.6}$$

$$r_{67} = 0.6 \ \Omega. \tag{G.7}$$

Identical converters are used for the three active loads; they share identical power buffer designs and also identical buck converters. The converter components and parasitic elements are listed in Tables G.1 and G.2.

B. Control Parameter

Power buffers share identical controller

$$G_i(s) = \frac{0.15s^2 + 7.5s}{s^2 + 5s + 5}. \tag{G.8}$$

The control matrices $\mathbf{k}_p$ and $\mathbf{k}_v$ are

$$\mathbf{k}_p = \begin{bmatrix} 0.11 & 0 & 0.05 \\ 0 & 0.11 & 0.05 \\ 0.07 & 0.07 & 0.1 \end{bmatrix}, \quad \mathbf{k}_v = -\begin{bmatrix} 0.1 & 0 & 0.1 \\ 0 & 0.1 & 0.1 \\ 0.07 & 0.07 & 0.1 \end{bmatrix}. \tag{G.9}$$

Table G-1 Boost Converter (Power Buffer) Component Values

Component Description	Symbol	Quantity	Unit
Converter input inductor	L	4.00	mH
Converter output capacitor	C	4.4	mF
Parasitic Element	**Symbol**	**Quantity**	**Unit**
Converter input inductor ESR	r_L	520	mΩ
Converter output capacitor ESR	r_C	25	mΩ
Control Parameter	**Symbol**	**Quantity**	**Unit**
Switching frequency	F_{sw}	50	kHz
Proportional gain (voltage controller)	k_p	0.005	---
Integral gain (voltage controller)	k_i	0.5	---
Rated output voltage	V_b^{rated}	100	V

Table G-2 Buck Converter and LC Filter Component Values

Component Description	Symbol	Quantity	Unit
LC filter inductor	L_{filter}	300	µH
LC filter capacitor	C_{filter}	2.2	mF
Converter output inductor	L	2.65	mH
Converter output capacitor	C	2.2	mF
Parasitic Element	**Symbol**	**Quantity**	**Unit**
LC filter inductor ESR	$r_{L\ filter}$	100	mΩ
LC filter capacitor ESR	$r_{C\ filter}$	50	mΩ
Converter output inductor ESR	r_L	520	mΩ
Converter output capacitor ESR	r_C	50	mΩ
Control Parameter	**Symbol**	**Quantity**	**Unit**
Switching frequency	F_{sw}	50	kHz
Proportional gain	k_p	0.007	---
Integral gain	k_i	0.7	---
Output voltage set point	v_{oi}^*	48	V

Appendix H

Microgrid Parameters for Studies in Chapter 6

A. Power System Parameter

Each of the underlying buck converters has $L = 2.64\ \mathrm{mH}$ and $C = 2.2\ \mathrm{mF}$ and works with the switching frequency of $F_s = 60\ \mathrm{kHz}$. Transmission lines series impedances are $Z_{12} = Z_{34} = Z_b$ and $Z_{25} = Z_{35} = 2Z_b$, where the base impedance is $Z_b = 0.5 + (50\ \mu\mathrm{H})s$. Impedances of the local loads are $R_1 = 30\,\Omega$ and $R_2 = R_3 = R_4 = 20\,\Omega$. Generation cost function are formulated as

$$C_1(i_1) = 0.2 + 0.1i_1 + 0.08i_1^2 \tag{H.1}$$

$$C_2(i_2) = 0.4 + 0.25i_2 + 0.19i_2^2 \tag{H.2}$$

$$C_3(i_3) = 0.2 + 0.12i_3 + 0.1i_3^2 \tag{H.3}$$

$$C_4(i_4) = 0.4 + 0.18i_4 + 0.14i_4^2 \tag{H.4}$$

B. Control Parameter

The adjacency matrix of the communication graph is

$$\mathbf{A_G} = \begin{bmatrix} 0.0 & 9.0 & 0.0 & 11 \\ 9.0 & 0.0 & 10 & 0.0 \\ 0.0 & 10 & 0.0 & 12 \\ 11 & 0.0 & 12 & 0.0 \end{bmatrix} \tag{H.5}$$

The coefficient that adjusts the convergence speed is $c = 0.02$. The controller matrix is

$$\mathbf{K}(s) = \begin{bmatrix} 0.1 + 7/s & 0.0 & 0.0 & 0.0 \\ 0.0 & 0.09 + 7.4/s & 0.0 & 0.0 \\ 0.0 & 0.0 & 0.08 + 6.6/s & 0.0 \\ 0.0 & 0.0 & 0.0 & 0.11 + 7/s \end{bmatrix} \tag{H.6}$$

References

[1] J. M. Guerrero, J. C. Vasquez, J. Matas, L. G. de Vincuña, and M. Castilla, “Hierarchical control of droop-controlled AC and DC microgrids – a general approach toward standardization,” *IEEE Trans. Ind. Electron.*, vol. 58, pp. 158–172, Jan. 2011.

[2] R. Majumder, B. Chaudhuri, A. Ghosh, R. Majumder, G. Ledwich, and F. Zare, “Improvement of stability and load sharing in an autonomous microgrid using supplementary droop control loop,” *IEEE Trans. Power Syst.*, vol. 25, no. 2, pp. 796–808, May 2010.

[3] H. Kakigano, Y. Miura, and T. Ise, “Distribution voltage control for DC microgrids using fuzzy control and gain-scheduling technique,” *IEEE Trans. Power Electron.*, vol. 28, no. 5, pp. 2246–2258, May 2013.

[4] H. Kakigano, Y. Miura, and T. Ise, “Low-voltage bipolar-type DC microgrid for super high quality distribution,” *IEEE Trans. Power Electron.*, vol. 25, no. 12, pp. 3066–3075, Dec. 2010.

[5] Y. K. Chen, Y. C. Wu, C. C. Song, and Y. S. Chen, “Design and implementation of energy management system with fuzzy control for DC microgrid systems,” *IEEE Trans. Power Electron.*, vol. 28, no. 4, pp. 1563–1570, Apr. 2013.

[6] D. Salomonsson, L. Söder, and A. Sannino, “An adaptive control system for a DC microgrid for data centers,” *IEEE Trans. Ind. Appl.*, vol. 44, no. 6, pp. 1910–1917, Nov./Dec. 2008.

[7] A. Kwasinski, “Quantitative evaluation of DC microgrids availability: effects of system architecture and converter topology design choices,” *IEEE Trans. Power Electron.*, vol. 26, no. 3, pp. 835–851, Mar. 2011.

[8] Y. C. Chang and C. M. Liaw, “Establishment of a switched-reluctance generator-based common DC microgrid system,” *IEEE Trans. Power Electron.*, vol. 26, no. 9, pp. 2512–2527, Sept. 2011.

[9] Y. Gu, X. Xiang, W. Li, and X. He, “Mode-adaptive decentralized control for renewable DC microgrid with enhanced reliability and flexibility,” to appear in *IEEE Trans. Power Electron.*, doi: 10.1109/TPEL.2013.2294204.

[10] P. C. Loh, D. Li; Y. K. Chai, and F. Blaabjerg, “Autonomous operation of hybrid microgrid with AC and DC subgrids,” *IEEE Trans. Power Electron.*, vol. 28, no. 5, pp. 2214–2223, May 2013.

[11] S. R. Huddy and J. D. Skufca, “Amplitude death solutions for stabilization of DC microgrids with instantaneous constant-power loads, *IEEE Trans. Power Electron.*, vol. 28, no. 1, pp. 247–253, Jan. 2013.

[12] N. Bottrell, M. Prodanovic, and T. C. Green, “Dynamic stability of a microgrid with an active load,” *IEEE Trans. Power Electron.*, vol. 28, no. 11, pp. 5107–5119, Nov. 2013.

[13] D. Chen and L. Xu, “Autonomous DC voltage control of a DC microgrid with multiple slack terminals,” *IEEE Trans. Power Syst.*, vol. 27, no. 4, pp. 1897–1905, Nov. 2012.

[14] M. Datta, T. Senjyu, A. Yona, T. Funabashi, and C. H. Kim, “A frequency-control approach by photovoltaic generator in a PV-diesel hybrid power system,” *IEEE Trans. Energy Convers.*, vol. 26, no. 2, pp. 559–571, Jun. 2011.

[15] S. Teleke, M. E. Baran, A. Q. Huang, S. Bhattacharya, and L. Anderson, “Control strategies for battery energy storage for wind farm dispatching,” *IEEE Trans. Energy Convers.*, vol. 24, no. 3, pp. 725–732, Sept. 2009.

[16] Z. Jiang and X. Yu, “Hybrid DC- and AC-linked microgrids: towards integration of distributed energy resources,” in *Proc. IEEE Conf. Global Sustain. Energy Infrastructure*, 2008, pp. 1–8.
[17] A. Kwasinski and C, N. Onwuchekwa, “Dynamic behavior and stabilization of DC microgrids with instantaneous constant-power loads,” *IEEE Trans. Power Electronics*, vol. 26, pp. 822-834, March 2011.
[18] H. Ikebe, “Power systems for telecommunications in the IT age,” in *Proc. of IEEE INTELEC*, 2003, pp. 1-8.
[19] R. S. Balog, W. Weaver, and P. T. Krein, “The load as an energy asset in a distributed DC smartgrid architecture,” *IEEE Trans. Smart Grid*, vol. 3, pp. 253-260, March 2012.
[20] L. Zhang, Y. Wang, H. Li, and P. Sun, “Hierarchical coordinated control of DC microgrid with wind turbines,” in *Proc. 38th Annu. Conf. IEEE Ind. Electron. Soc. (IECON)*, 2012, pp. 3547–3552.
[21] L. Xu and D. Chen, “Control and operation of a DC microgrid with variable generation and energy storage,” *IEEE Trans. Power Del.*, vol. 26, no. 4, pp. 2513–2522, Oct. 2011.
[22] C. Yuen, A. Oudalov, and A. Timbus, “The provision of frequency control reserves from multiple microgrids,” *IEEE Trans. Ind. Electron.*, vol. 58, no. 1, pp. 173–183, Jan. 2011.
[23] H. Kanchev, D. Lu, F. Colas, V. Lazarov, and B. Francois, “Energy management and operational planning of a microgrid with a PV-based active generator for smart grid applications,” *IEEE Trans. Ind. Electron*., vol. 58, no. 10, pp. 4583–4592, Oct. 2011.
[24] C. Chen, S. Duan, T. Cai, B. Liu, and G. Hu, “Optimal allocation and economic analysis of energy storage system in microgrids,” *IEEE Trans. Power Electron*., vol. 26, no. 10, pp. 2762–2773, Oct. 2011.
[25] T. Zhou and B. Francois, “Energy management and power control of a hybrid active wind generator for distributed power generation and grid integration,” *IEEE Trans. Ind. Electron.*, vol. 58, no. 1, pp. 95–104, Jan. 2011.
[26] S. Anand, B. G. Fernandes, and J. M. Guerrero, “Distributed control to ensure proportional load sharing and improve voltage regulation in low-voltage DC microgrids,” *IEEE Trans. Power Electron.*, vol. 28, no. 4, pp. 1900–1913, Apr. 2013.
[27] P. C. Loh, D. Li, Y. K. Chai, and F. Blaabjerg, “Autonomous control of interlinking converter with energy storage in hybrid AC–DC microgrid,” *IEEE Trans. Ind. Appl.*, vol. 49, no. 3, pp. 1374–1382, May/Jun. 2013.
[28] J. Schönberger, R. Duke, and S. D. Round, “DC-bus signaling: a distributed control strategy for a hybrid renewable Nanogrid,” *IEEE Trans. Ind. Electron.*, vol. 53, no. 5, pp. 1453–1460, Oct. 2006.
[29] K. Sun, L. Zhang, Y. Xing, and J. M. Guerrero, “A distributed control strategy based on DC bus signaling for modular photovoltaic generation systems with battery energy storage,” *IEEE Trans. Power Electron.*, vol. 26, no. 10, pp. 3032–3045, Oct. 2011.
[30] D. Chen, L. Xu, L. Yao, “DC voltage variation based autonomous control of DC microgrids,” *IEEE Trans. Power Del.*, vol. 28, no. 2, pp. 637–648, Apr. 2013.
[31] P. Karlsson and J. Svensson, “DC bus voltage control for a distributed power system,” *IEEE Trans. Power Electron.*, vol. 18, no. 6, pp. 1405–1412, Nov. 2003.

[32] Y. Ito, Y. Zhongqing, and H. Akagi, “DC microgrid based distribution power generation system,” in *Proc. 4th Int. Power Electron. Motion Control Conf. (IPEMC)*, 2004, pp. 1740–1745.
[33] W. Qiu and Z. Liang, “Practical design considerations of current sharing control for parallel VRM applications,” in *Proc. 20th Annu. Appl. Power Electron. Conf. Expo.*, 2005, pp. 281–286.
[34] J. M. Guerrero, L. Hang, and J. Uceda, “Control of distributed uninterruptible power supply systems,” *IEEE Trans. Ind. Electron.*, vol. 55, no. 8, pp. 2845–2859, Aug. 2008.
[35] X. Lu, K. Sun, J. M. Guerrero, J. C. Vasquez, and L. Huang, “State-of-charge balance using adaptive droop control for distributed energy storage systems in DC microgrid applications,” *IEEE Trans. Ind. Electron.*, vol. 61, no. 6, pp. 2804–2815, Jun. 2014.
[36] R. A. F. Ferreira, H. A. C. Braga, A. A. Ferreira, and P. G. Barbosa, “Analysis of voltage droop control method for DC microgrids with Simulink: modeling and simulation,” in *Proc. 10th IEEE/IAS Int. Conf. Ind. Appl. (INDUSCON)*, 2012, pp. 1–6.
[37] J. A. P. Lopes, C. L. Moreira, and A. G. Madureira, “Defining control strategies for microgrids islanded operation,” *IEEE Trans. Power Syst.*, vol. 21, no. 2, pp. 916–924, May 2006.
[38] A. Tuladhar, H. Jin, T. Unger, and K. Mauch, “Control of parallel inverters in distributed AC power systems with consideration of line impedance effect,” *IEEE Trans. Ind. Appl.*, vol. 36, no. 1, pp. 131–138, Jan./Feb. 2000.
[39] J. M. Guerrero, L. G. Vicuña, J. Matas, M. Castilla, and J. Miret, “Output impedance design of parallel-connected UPS inverters with wireless load sharing control,” *IEEE Trans. Ind. Electron.*, vol. 52, no. 4, pp. 1126–1135, Aug. 2005.
[40] M. N. Marwali, J. W. Jung, and A. Keyhani, “Control of distributed generation systems – Part II: Load sharing control,” *IEEE Trans. Power Electron.*, vol. 19, no. 6, pp. 1551–1561, Nov. 2004.
[41] K. De Brabandere, B. Bolsens, J. Van Den Keybus, A. Woyte, J. Driesen, and R. Belmans, “A voltage and frequency droop control method for parallel inverters,” *IEEE Trans. Power Electron.*, vol. 22, no. 4, pp. 1107–1115, Jul. 2007.
[42] Y. Mohamed and E. F. El-Saadany, “Adaptive decentralized droop controller to preserve power sharing stability of paralleled inverters in distributed generation microgrids,” *IEEE Trans. Power Electron.*, vol. 23, no. 6, pp. 2806–2816, Nov. 2008.
[43] X. Lu, J. M. Guerrero, K. Sun, and J. C. Vasquez, “An improved droop control method for DC microgrids based on low bandwidth communication with DC bus voltage restoration and enhanced current sharing accuracy,” *IEEE Trans. Power Electron.*, vol. 29, no. 4, pp. 1800–1812, Apr. 2014.
[44] S. Anand and B. G. Fernandes, “Steady state performance analysis for load sharing in DC distributed generation system,” in Proc. *10th Int. Conf. Environment Elect. Eng. (EEEIC)*, 2011, pp. 1–4.
[45] Y. W. Li and C. N. Kao, “An accurate power control strategy for power-electronics-interfaced distributed generation units operation in a low voltage multi-bus microgrid,” *IEEE Trans. Power Electron.*, vol. 24, no. 12, pp. 2977–2988, Dec. 2009.
[46] J. He and Y. W. Li, “Analysis, design and implementation of virtual impedance for power electronics interfaced distributed generation,” *IEEE Trans. Ind. Appl.*, vol. 47, no. 6, pp. 2525–2538, Nov./Dec. 2011.

[47] W. Qiu and Z. Liang, “Practical design considerations of current sharing control for parallel VRM applications,” in *Proc. 20th Annu. Appl. Power Electron. Conf. Expo.*, 2005, pp. 281–286.
[48] H. Laaksonen, P. Saari, and R. Komulainen, “Voltage and frequency control of inverter based weak LV network microgrid,” in *Proc. Int. Conf. Future Power Syst.*, 2005, pp. 1–6.
[49] T. L. Vandoorn, B. Meersman, L. Degroote, B. Renders, and L. Vandevelde, “A control strategy for islanded microgrids with DC-link voltage control,” *IEEE Trans. Power Del.*, vol. 26, no. 2, pp. 703–713, Apr. 2011.
[50] L. Meng, T. Dragicevic, J. M. Guerrero, and J. C. Vasquez, “Optimization with system damping restoration for droop controlled DC-DC converters,” in *Proc. IEEE Energy Convers. Cong. Expo. (ECCE)*, 2013, pp. 65–72.
[51] T. Dragicevic, J. M. Guerrero, J. C. Vasquez, and D. Skrlec, “Supervisory control of an adaptive-droop regulated DC microgrid with battery management capability,” *IEEE Trans. Power Electron.*, vol. 29, no. 2, pp. 695–706, Feb. 2014.
[52] Q. Shafiee, J. M. Guerrero, and J. C. Vasquez, “Distributed secondary control for islanded microgrids – A novel approach,” *IEEE Trans. Power Electron.*, vol. 29, no. 2, pp. 1018–1031, Feb. 2014.
[53] V. Nasirian, A. Davoudi, and F. L. Lewis, “Distributed adaptive droop control for DC microgrids,” in *Proc. 29th IEEE Appl. Power Electron. Conf. Expo. (APEC)*, 2014, pp. 1147–1152.
[54] R. Olfati-Saber and R. M. Murray, “Consensus problems in networks of agents with switching topology and time-delays,” *IEEE Trans. Autom. Control*, vol. 49, no. 9, pp. 1520–1533, Sept. 2004.
[55] D. P. Spanos, R. Olfati-Saber, and R. M. Murray, “Dynamic consensus for mobile networks,” in *Proc. 16th Int. Fed. Aut. Control (IFAC)*, 2005, pp. 1–6.
[56] M. Furukawa, J. Xu, Y. Shimizu, and Y. Kato, “Scratch-induced demagnetization of perpendicular magnetic disk,” *IEEE Trans. Magn.*, vol. 44, no. 11, pp. 3633–3636, Nov. 2008.
[57] V. Sridharan, H. Asadi, M. B. Tahoori, and D. Kaeli, “Reducing data cache susceptibility to soft errors,” *IEEE Trans. Dependable and Secure Computing*, vol. 3, no. 4, pp. 353–364, Oct./Dec. 2006.
[58] R. W. Erickson and D. Maksimovic, *Fundamental of Power Electronics*, 2nd Ed. Norwell, MA: Kluwer, 2001.
[59] V. Nasirian, Y. Karimi, A. Davoudi, M. R. Zolghadri, M. Ahmadian, and S. Moayedi, “Dynamic model development and variable switching-frequency control for DCVM Cúk converters in PFC applications,” *IEEE Trans. Ind. Appl.*, vol. 49, no. 6, pp. 2636–2650, Nov./Dec. 2013.
[60] D. Nilsson and A. Sannino, “Efficiency analysis of low- and medium voltage DC distribution systems,” in *Proc. IEEE Power Eng. Soc. Gen. Meeting*, 2004, pp. 2315–2321.
[61] S. Anand and B. G. Fernandes, “Optimal voltage level for DC microgrids,” in *Proc. 36th Annu. Conf. IEEE Ind. Electron. Soc. (IECON)*, 2010, pp. 3034–3039.
[62] T. Pavlovic, T. Bjazic, and Z. Ban, “Simplified averaged models of DC–DC power converters suitable for controller design and microgrid simulation,” *IEEE Trans. Power Electron.*, vol. 28, no. 7, pp. 3266–3275, Jul. 2013.
[63] Z. Qu*, Cooperative Control of Dynamical Systems: Applications to Autonomous Vehicles*, New York, NY, USA: Springer-Verlag, 2009.

[64] D. Chen and L. Xu, “Autonomous DC voltage control of a DC microgrid with multiple slack terminals,” *IEEE Trans. Power Syst.*, vol. 27, no. 4, pp. 1897–1905, Nov. 2012.
[64] M. Datta, T. Senjyu, A. Yona, T. Funabashi, and C. H. Kim, “A frequency-control approach by photovoltaic generator in a PV-diesel hybrid power system,” *IEEE Trans. Energy Convers.*, vol. 26, no. 2, pp. 559–571, Jun. 2011.
[65] S. Teleke, M. E. Baran, A. Q. Huang, S. Bhattacharya, and L. Anderson, “Control strategies for battery energy storage for wind farm dispatching,” *IEEE Trans. Energy Convers.*, vol. 24, no. 3, pp. 725–732, Sept. 2009.
[66] Y. K. Chen, Y. C. Wu, C. C. Song, and Y. S. Chen, “Design and implementation of energy management system with fuzzy control for DC microgrid systems,” *IEEE Trans. Power Electron.*, vol. 28, no. 4, pp. 1563–1570, Apr. 2013.
[67] A. Kwasinski and C, N. Onwuchekwa, “Dynamic behavior and stabilization of DC microgrids with instantaneous constant-power loads,” *IEEE Trans. Power Electronics*, vol. 26, pp. 822-834, March 2011.
[68] R. S. Balog, W. Weaver, and P. T. Krein, “The load as an energy asset in a distributed DC Smartgrid architecture,” *IEEE Trans. Smart Grid*, vol. 3, pp. 253-260, March 2012.
[69] J. M. Guerrero, J. C. Vasquez, J. Matas, L. G. de Vincuña, and M. Castilla, “Hierarchical control of droop-controlled AC and DC microgrids – a general approach toward standardization,” *IEEE Trans. Ind. Electron.*, vol. 58, pp. 158–172, Jan. 2011.
[70] M. Savaghebi, A. Jalilian, J. C. Vasquez, and J. M. Guerrero, “Secondary control scheme for voltage unbalance compensation in an islanded droop-controlled microgrid,” *IEEE Trans. Smart Grid*, vol. 3, no. 2, pp. 797–807, Jun. 2012.
[71] X. Lu, J. M. Guerrero, K. Sun, J. C. Vasquez, R. Teodorescu, and L. Huang, “Hierarchical control of parallel AC-DC converter interfaces for hybrid microgrids,” *IEEE Trans. Smart Grid*, vol. 5, pp. 683–692, Mar. 2014.
[72] C. Lin, P. Wang, J. Xiao, Y. Tang, and F. H. Choo, “Implementation of hierarchical control in DC microgrids,” *IEEE Trans. Ind. Electron.*, vol. 61, pp. 4032–4042, Aug. 2014.
[73] L. Xu and D. Chen, “Control and operation of a DC microgrid with variable generation and energy storage,” *IEEE Trans. Power Del.*, vol. 26, no. 4, pp. 2513–2522, Oct. 2011.
[74] H. Kanchev, D. Lu, F. Colas, V. Lazarov, and B. Francois, “Energy management and operational planning of a microgrid with a PV-based active generator for smart grid applications,” *IEEE Trans. Ind. Electron*., vol. 58, no. 10, pp. 4583–4592, Oct. 2011.
[75] C. Chen, S. Duan, T. Cai, B. Liu, and G. Hu, “Optimal allocation and economic analysis of energy storage system in microgrids,” *IEEE Trans. Power Electron*., vol. 26, no. 10, pp. 2762–2773, Oct. 2011.
[76] T. Zhou and B. Francois, “Energy management and power control of a hybrid active wind generator for distributed power generation and grid integration,” *IEEE Trans. Ind. Electron.*, vol. 58, no. 1, pp. 95–104, Jan. 2011.
[77] P. C. Loh, D. Li, Y. K. Chai, and F. Blaabjerg, “Autonomous control of interlinking converter with energy storage in hybrid AC–DC microgrid,” *IEEE Trans. Ind. Appl.*, vol. 49, no. 3, pp. 1374–1382, May/Jun. 2013.
[78] S. Anand, B. G. Fernandes, and J. M. Guerrero, “Distributed control to ensure proportional load sharing and improve voltage regulation in low-voltage DC

microgrids," *IEEE Trans. Power Electron.*, vol. 28, no. 4, pp. 1900–1913, Apr. 2013.
[79] J. Schönberger, R. Duke, and S. D. Round, "DC-bus signaling: a distributed control strategy for a hybrid renewable Nanogrid," *IEEE Trans. Ind. Electron.*, vol. 53, no. 5, pp. 1453–1460, Oct. 2006.
[80] D. Chen, L. Xu, L. Yao, "DC voltage variation based autonomous control of DC microgrids," *IEEE Trans. Power Del.*, vol. 28, no. 2, pp. 637–648, Apr. 2013.
[81] P. Karlsson and J. Svensson, "DC bus voltage control for a distributed power system," *IEEE Trans. Power Electron.*, vol. 18, no. 6, pp. 1405–1412, Nov. 2003.
[82] Y. Ito, Y. Zhongqing, and H. Akagi, "DC microgrid based distribution power generation system," in *Proc. 4th Int. Power Electron. Motion Control Conf. (IPEMC)*, 2004, pp. 1740–1745.
[83] X. Lu, K. Sun, J. M. Guerrero, J. C. Vasquez, and L. Huang, "State-of-charge balance using adaptive-droop control for distributed energy storage systems in DC microgrid applications," *IEEE Trans. Ind. Electron.*, vol. 61, no. 6, pp. 2804–2815, June 2014.
[84] R. A. F. Ferreira, H. A. C. Braga, A. A. Ferreira, and P. G. Barbosa, "Analysis of voltage droop control method for DC microgrids with Simulink: modeling and simulation," in *Proc. 10th IEEE/IAS Int. Conf. Ind. Appl. (INDUSCON)*, 2012, pp. 1–6.
[85] J. A. P. Lopes, C. L. Moreira, and A. G. Madureira, "Defining control strategies for microgrids islanded operation," *IEEE Trans. Power Syst.*, vol. 21, no. 2, pp. 916–924, May 2006.
[86] A. Tuladhar, H. Jin, T. Unger, and K. Mauch, "Control of parallel inverters in distributed AC power systems with consideration of line impedance effect," *IEEE Trans. Ind. Appl.*, vol. 36, no. 1, pp. 131–138, Jan./Feb. 2000.
[87] Y. Mohamed and E. F. El-Saadany, "Adaptive decentralized droop controller to preserve power sharing stability of paralleled inverters in distributed generation microgrids," *IEEE Trans. Power Electron.*, vol. 23, no. 6, pp. 2806–2816, Nov. 2008.
[88] J. Kim, J. M. Guerrero, P. Rodriguez, R. Teodorescu, and K. Nam, "Mode adaptive droop control with virtual output impedances for an inverter-based flexible AC microgrid, *IEEE Trans. Power Electron.*, vol. 26, no. 3, pp. 689–701, Mar. 2011.
[89] N. R. Chaudhuri and B. Chaudhuri, "Adaptive droop control for effective power sharing in multi-terminal DC (MTDC) grids," *IEEE Trans. Power Syst.*, vol. 28, no. 1, pp. 21–29, Feb. 2013.
[90] S. Y. Yang, C. W. Zhang, X. Zhang, R. X. Cao, and W. X. Shen, "Study on the control strategy for parallel operation of inverters based on adaptive droop method," in *Proc. IEEE Conf. Ind. Electron.ics Appl.*, 2009, pp.1–5.
[91] J. Yuan, F. Gao, H. Gao, H. Zhang, and J. Wu, "An adaptive control strategy for parallel operated photovoltaic inverters," in *Proc. 7th Int. Power Electron. Motion. Control Conf. (IPEMC)*, 2012, pp. 1522–1526.
[92] R. Majumder, A. Ghosh, G. Ledwich, F. Zare, "Power system stability and load sharing in distributed generation," in *Proc. IEEE Joint Int. Conf. Power Syst. Technol.*, 2008, pp.1–6.
[93] W. Yao, M. Chen, M. Gao, and Z. Qian, "A wireless load sharing controller to improve the performance of parallel-connected inverters," in *Proc. IEEE 23rd Annu Applied Power Electron. Conf. Expo. (APEC)*, 2008, pp. 1628–1631.
[94] W. Yao, M. Chen, M. Gao, and Z. Qian, "Development of communicationless hot-swap paralleling for single-phase UPS inverters based on adaptive droop method,"

in *Proc. IEEE 23rd Annu Applied Power Electron. Conf. Expo. (APEC*), 2009, pp. 1283–1287.

[95] J. C. Vasquez, J. M. Guerrero, E. Gregorio, P. Rodriguez, R. Teodorescu, F. Blaabjerg, “Adaptive-droop control applied to distributed generation inverters connected to the grid,” in *Proc. IEEE Int. Symp. Ind. Electron. (ISIE), 2008*, pp.2420–2425.

[96] J. C. Vasquez, J. M. Guerrero, A. Luna, P. Rodriguez, and R. Teodorescu, “Adaptive-droop control applied to voltage-source inverters operating in grid-connected and islanded modes,” *IEEE Trans. Ind. Electron.*, vol. 56, no. 10, pp. 4088–4096, Oct. 2009.

[97] A. D. Erdogan and M. T. Aydemir, “Application of adaptive-droop method to boost converters operating at the output of fuel cells,” in *Proc. Int. Elec. Electron. Eng. Conf. (ELECO)*, 2009, pp.I-321–I-325.

[98] T. Dragicevic, J. M. Guerrero, J. C. Vasquez, and D. Skrlec, “Supervisory control of an adaptive-droop regulated DC microgrid with battery management capability,” *IEEE Trans. Power Electron.*, vol. 29, no. 2, pp. 695–706, Feb. 2014.

[99] H. Liu, Z. Hu, Y. Song, and J. Lin, “Decentralized vehicle-to-grid control for primary frequency regulation considering charging demands,” *IEEE Trans. Power Syst.*, vol. 28, no. 3, pp. 3480–3489, Aug. 2013.

[100] S. Anand and B. G. Fernandes, “Steady state performance analysis for load sharing in DC distributed generation system,” in Proc. *10th Int. Conf. Environment Elect. Eng. (EEEIC)*, 2011, pp. 1–4.

[101] Y. W. Li and C. N. Kao, “An accurate power control strategy for power-electronics-interfaced distributed generation units operation in a low voltage multi-bus microgrid,” *IEEE Trans. Power Electron.*, vol. 24, no. 12, pp. 2977–2988, Dec. 2009.

[102] J. He and Y. W. Li, “Analysis, design and implementation of virtual impedance for power electronics interfaced distributed generation,” *IEEE Trans. Ind. Appl.*, vol. 47, no. 6, pp. 2525–2538, Nov./Dec. 2011.

[103] W. Qiu and Z. Liang, “Practical design considerations of current sharing control for parallel VRM applications,” in *Proc. 20th Annu. Appl. Power Electron. Conf. Expo.*, 2005, pp. 281–286.

[104] H. Laaksonen, P. Saari, and R. Komulainen, “Voltage and frequency control of inverter based weak LV network microgrid,” in *Proc. Int. Conf. Future Power Syst.*, 2005, pp. 1–6.

[105] T. L. Vandoorn, B. Meersman, L. Degroote, B. Renders, and L. Vandevelde, “A control strategy for islanded microgrids with dc-link voltage control,” *IEEE Trans. Power Del.*, vol. 26, no. 2, pp. 703–713, Apr. 2011.

[106] Q. Shafiee, J. M. Guerrero, and J. C. Vasquez, “Distributed secondary control for islanded microgrids – A novel approach,” *IEEE Trans. Power Electron.*, vol. 29, no. 2, pp. 1018–1031, Feb. 2014.

[107] X. Lu, J. M. Guerrero, K. Sun, and J. C. Vasquez, “An improved droop control method for DC microgrids based on low bandwidth communication with DC bus voltage restoration and enhanced current sharing accuracy,” *IEEE Trans. Power Electron.*, vol. 29, no. 4, pp. 1800–1812, Apr. 2014.

[108] V. Nasirian, S. Moayedi, A. Davoudi, and F. L. Lewis, “Distributed cooperative control of DC microgrids,” *IEEE Trans. Power Electron.*, to be published, DOI: 10.1109/TPEL.2014.2324579.

[109] R. Olfati-Saber and R. M. Murray, “Consensus problems in networks of agents with switching topology and time-delays,” *IEEE Trans. Autom. Control*, vol. 49, no. 9, pp. 1520–1533, Sept. 2004.
[110] D. P. Spanos, R. Olfati-Saber, and R. M. Murray, “Dynamic consensus for mobile networks,” in *Proc. 16th Int. Fed. Aut. Control (IFAC)*, 2005, pp. 1–6.
[111] R. W. Erickson and D. Maksimovic, *Fundamental of Power Electronics*, 2nd Ed. Norwell, MA: Kluwer, 2001.
[112] V. Nasirian, Y. Karimi, A. Davoudi, M. R. Zolghadri, M. Ahmadian, and S. Moayedi, “Dynamic model development and variable switching-frequency control for DCVM Cúk converters in PFC applications,” *IEEE Trans. Ind. Appl.*, vol. 49, no. 6, pp. 2636–2650, Nov./Dec. 2013.
[113] S. Moayedi, V. Nasirian, F. L. Lewis, and A. Davoudi, “Team-oriented load sharing in parallel DC-DC converters” *IEEE Trans. Ind. Electron.*, to be published, DOI: 10.1109/TIA.2014.2336982.
[114] J. M. Guerrero, M. Chandorkar, T. Lee, and P. C. Loh, “Advanced control architectures for intelligent microgrids—part I: decentralized and hierarchical control,” *IEEE Trans. Ind. Electron.*, vol. 60, no. 4, pp. 1254–1262, Apr. 2013.
[115] D. Nilsson and A. Sannino, “Efficiency analysis of low- and medium voltage DC distribution systems,” in *Proc. IEEE Power Eng. Soc. Gen. Meeting*, 2004, pp. 2315–2321.
[116] S. Anand and B. G. Fernandes, “Optimal voltage level for DC microgrids,” in *Proc. 36th Annu. Conf. IEEE Ind. Electron. Soc. (IECON)*, 2010, pp. 3034–3039.
[117] N. Amelina and A. Fradkov, “Consensus problem in stochastic network systems with switched topology, noise, and delay,” in *Proc. 12th Int. Conf. Network*, 2013, pp. 118–124.
[118] R. Olfati-Saber and R. M. Murray, “Consensus problems in networks of agents with switching topology and time-delays,” *IEEE Trans. Automat. Control*, vol. 49, no. 9, pp. 1520–1533, Sept. 2004.
[119] S. Kar and J. M. F. Moura, “Distributed consensus algorithms in sensor networks with imperfect communication: link failures and channel noise,” *IEEE Trans. Signal Process.*, vol. 57, no. 1, pp. 355–369, Jan. 2009.
[120] J. M. Guerrero, J. C. Vasquez, J. Matas, L. G. de Vincuña, and M. Castilla, “Hierarchical control of droop-controlled AC and DC microgrids – A general approach toward standardization,” *IEEE Trans. Ind. Electron.*, vol. 58, pp. 158–172, Jan. 2011.
[121] R. Majumder, B. Chaudhuri, A. Ghosh, R. Majumder, G. Ledwich, and F. Zare, “Improvement of stability and load sharing in an autonomous microgrid using supplementary droop control loop,” *IEEE Trans. Power Syst.*, vol. 25, no. 2, pp. 796–808, May 2010.
[122] H. Kakigano, Y. Miura, and T. Ise, “Distribution voltage control for DC microgrids using fuzzy control and gain-scheduling technique,” *IEEE Trans. Power Electron.*, vol. 28, no. 5, pp. 2246–2258, May 2013.
[123] I. U. Nutkani, P. C. Loh, P. Wang, and F. Blaabjerg, “Cost-prioritized droop schemes for autonomous AC microgrids,” *IEEE Trans. Power Electron.*, vol. 30, no. 2, pp. 1109–1119, Feb. 2015.
[124] P. C. Loh, D. Li; Y. K. Chai, and F. Blaabjerg, “Autonomous operation of hybrid microgrid with AC and DC subgrids,” *IEEE Trans. Power Electron.*, vol. 28, no. 5, pp. 2214–2223, May 2013.

[125] M. Datta, T. Senjyu, A. Yona, T. Funabashi, and C. H. Kim, “A frequency-control approach by photovoltaic generator in a PV-diesel hybrid power system,” *IEEE Trans. Energy Convers.*, vol. 26, no. 2, pp. 559–571, Jun. 2011.
[126] C. K. Sao and W. Lehn, “Control and power management of converter-fed microgrids,” *IEEE Trans. Power Syst.,* vol. 23, pp. 1088–1098, Aug. 2008.
[127] E. Serban and H. Serban, “A control strategy for a distributed power generation microgrid application with voltage- and current-controlled source converter,” *IEEE Trans. Power Electron.*, vol. 15, pp. 2981–2992, Dec. 2010.
[128] A. Bidram and A. Davoudi, “Hierarchical structure of microgrids control system,” *IEEE Trans. Smart Grid*, vol. 3, pp. 1963–1976, Dec 2012.
[129] J. C. Vasquez, J. M. Guerrero, J. Miret, M. Castilla, and L.G. de Vicuña, “Hierarchical control of intelligent microgrids,” *IEEE Ind. Electron. Mag.*, vol. 4, pp. 23–29, Dec. 2010.
[130] J. A. P. Lopes, C. L. Moreira, and A. G. Madureira, “Defining control strategies for microgrids islanded operation,” *IEEE Trans. Power Syst.,* vol. 21, pp. 916–924, May 2006.
[131] F. Katiraei, M. R. Iravani, and P. W. Lehn, “Microgrid autonomous operation during and subsequent to islanding process,” *IEEE Trans. Power Del.,* vol. 20, pp. 248–257, Jan. 2005.
[132] M. Savaghebi, A. Jalilian, J. Vasquez, and J. Guerrero, “Secondary control for voltage quality enhancement in microgrids,” *IEEE Trans. Smart Grid,* vol. 3, pp. 1893–1902, Dec. 2012.
[133] H. Kanchev, D. Lu, F. Colas, V. Lazarov, and B. Francois, “Energy management and operational planning of a microgrid with a PV-based active generator for smart grid applications,” *IEEE Trans. Ind. Electron*., vol. 58, no. 10, pp. 4583–4592, Oct. 2011.
[134] C. Chen, S. Duan, T. Cai, B. Liu, and G. Hu, “Optimal allocation and economic analysis of energy storage system in microgrids,” *IEEE Trans. Power Electron*., vol. 26, no. 10, pp. 2762–2773, Oct. 2011.
[135] N. Ainsworth and S. Grijalva, “A structure-preserving model and sufficient condition of frequency synchronization of lossless droop inverter-based AC network,” *IEEE Trans. Power Syst.*, vol. 28, pp. 4310–4319, Nov. 2013.
[136] D. Wu, F. Tang, J. M. Guerrero, and J. C. Vasquez, “Autonomous control of distributed generation and storage to coordinate P/Q sharing in islanded microgrids – An approach beyond droop control,” in *Proc. IEEE Int. Energy Conf.*, 2014, pp. 983–988.
[137] J. Y. Kim, J. H. Jeon, S. K. Kim, C. Cho, J. H. Park, H. M. Kim, and K. Y. Nam, “Cooperative control strategy of energy storage system and micro sources for stabilizing the microgrid during islanded operation,” *IEEE Trans. Power Electron.*, vol. 25, pp. 3037–3048, Dec. 2010.
[138] S. M. Ashabani and Y. A. R. I. Mohamed, “General interface for power management of micro-grids using nonlinear cooperative droop control,” *IEEE Trans. Power Syst.*, vol. 28, pp. 2929–2941, Aug. 2013.
[139] J. Hu, J. Zhu, D. G. Dorrell, and J. M. Guerrero, “Virtual flux droop method – A new control strategy of inverters in microgrids,” *IEEE Trans. Power Electron.*, vol. 29, pp. 4704–4711, Sept. 2014.
[140] Y. A. I. Mohamed and E. F. El-Saadany, “Adaptive decentralized droop controller to preserve power sharing stability of paralleled inveretrs in distributed generation microgrids,” *IEEE Trans. Power Electronics*, vol. 23, pp. 2806–2816, Nov. 2008.

[141] J. He and Y. W. Li, “Analysis, design, and implementation of virtual impedance for power electronics interfaced distributed generation,” *IEEE Trans. Ind. Appl.*, vol. 41, pp. 2525–2538, Nov./Dec. 2011.
[142] J. W. Simpson-Porco, F. Dorfler, and F. Bullo, “Voltage stabilization in microgrids via quadratic droop control,” *IEEE 52nd Annu. Conf. Decision and Control*, 2013, pp. 7582–7589.
[143] H. Mahmood, D. Michaelson, and J. Jiang, “Accurate reactive power sharing in an islanded microgrid using adaptive virtual impedances,” *IEEE Trans. Power Electron.*, vol. 30, no. 3, pp. 1605–1617, Mar. 2015.
[144] H. Han, Y. Liu, Y. Sun, M. Su, and J. M. Guerrero, “An improved droop control strategy for reactive power sharing in islanded microgrid,” *IEEE Trans. Power Electron.*, vol. 30, no. 6, pp. 3133–3141, Jun. 2015.
[145] J. Rocabert, A. Luna, F. Blaabjerg, and P. Rodriguez, “Control of power converters in AC microgrids,” *IEEE Trans. Power Electron.*, vol. 27, pp. 4734–4749, Nov. 2012.
[146] C. T. Lee, C. C. Chu, and P. T. Cheng, “A new droop control method for the autonomous operation for distribute energy resource interface converters,” *IEEE Trans. Power Electron.*, vol. 28, pp. 1980–1993, Apr. 2013.
[147] S. V. Dhople. B. B. Johnson, and A. O. Hamadeh, “Virtual oscillator control for voltage source inverters,” in *Proc. 51st Annu. Allerton Conf.*, 2013, pp. 1359–1363.
[148] B. B. Johnson, S. V. Dhople. A. O. Hamadeh, and P. T. Krein, “Synchronization of nonlinear oscillators in an LTI electrical power network,” *IEEE Trans. Circuits Syst. I: Reg. Papers*, vol. 61, pp. 834–844, Mar. 2014.
[149] B. B. Johnson, S. V. Dhople. A. O. Hamadeh, and P. T. Krein, “Synchronization of parallel single-phase inverters with virtual oscillator control,” *IEEE Trans. Power Electron.*, vol. 29, no. 11, pp. 6124–6138, Nov. 2014.
[150] B. B. Johnson, S. V. Dhople, J. L. Cale, A. O. Hamadeh, and P. T. Krein, “Oscillator-based inverter control for islanded three-phase microgrids,” IEEE J. *Photovoltaics*, vol. 4, no. 1, pp. 387–395, Jan. 2014.
[151] T. L. Vandon, B. Meersman, J. D. M. De Koonig, and L. Vandevelde, “Analogy between conventional grid control and islanded microgrid control based on a global dc-link voltage droop,” *IEEE Trans. Power Del.*, vol. 27, pp. 1405–1414, July 2012.
[152] A. H. Etemadi, E. J. Davison, R. Iravani, “A decentralized robust strategy for multi-DER microgrids – Part I: Fundamental concepts,” *IEEE Trans. Power Del.*, vol. 27, pp. 1843–1853, Oct. 2012.
[153] Q. Shafiee, V. Nasirian, J. M. Guerrero, F. L. Lewis, and A. Davoudi, “Team-oriented adaptive droop control for autonomous AC microgrids,” in *Proc. 40th Ind. Electron. Conf. (IECON)*, 2014, pp. 1861–1867.
[154] A. Micallef, M. Apap, C. Spiteri-Staines, J. M. Guerrero, and J. C. Vasquez, “Reactive power sharing and voltage harmonic distortion compensation of droop controlled single phase islanded microgrids,” *IEEE Trans. Smart Grid*, vol. 5, pp. 1149–1158, May 2014.
[155] A. Mehrizi-Sani and R. Iravani, “Potential-function based control of a microgrid in islanded and grid-connected modes,” *IEEE Trans. Power Syst.,* vol. 25, pp. 1883–1891, Nov. 2010.
[156] A. Mehrizi-sani and R. Iravani, “Constrained potential function-based control of microgrids for improved dynamic performance,” *IEEE Trans. Smart Grid*, vol. 3, pp. 1885–1892, Dec. 2012.

[157] A. H. Etemadi, E. J. Davison, R. Iravani, “A decentralized robust strategy for multi-DER microgrids – Part II: Performance evaluation,” *IEEE Trans. Power Del.*, vol. 27, pp. 1854–1861, Oct. 2012.
[158] A. H. Etemadi, E. J. Davison, R. Iravani, “A generalized decentralized robust control of islanded microgrids,” *IEEE Trans. Power Syst.*, vol. 29, no. 6, pp. 3102–3113, Nov. 2014.
[159] A. Kahrobaeian and Y. A. R. I. Mohamed, “Networked-based hybrid distributed power sharing and control of islanded micro-grid systems,” *IEEE Trans. Power Electron.*, vol. 30, no. 2, pp. 603–617, Feb. 2015.
[160] Q. Hui and W. Haddad, “Distributed nonlinear control algorithms for network consensus,” *Automatica*, vol. 42, pp. 2375–2381, Sept. 2008.
[161] J. Fax and R. Murray, “Information flow and cooperative control of vehicle formations,” *IEEE Trans. Automat. Control*, vol. 49, pp. 1465–1476, Sept. 2004.
[162] Z. Qu, *Cooperative control of dynamical systems: Applications to autonomous vehicles*. New York: Springer-Verlag, 2009.
[163] Q. Shafiee, J. M. Guerrero, and J. C. Vasquez, “Distributed secondary control for islanded microgrids – A novel approach,” *IEEE Trans. Power Electron.*, vol. 29, pp. 1018–1031, Feb. 2014.
[164] Q. Shafiee, C. Stefanovic, T. Dragicevic, P. Popovski, J. C. Vasquez, and J. M. Guerrero, “Robust networked control scheme for distributed secondary control of islanded microgrids,” *IEEE Trans. Ind. Electron.*, vol. 61, pp. 5363–5374, Oct. 2014.
[165] Y. Zhang and H. Ma, “Theoretical and experimental investigation of networked control for parallel operation of inverters,” *IEEE Trans. Ind. Electron.*, vol. 59, pp. 1961–1970, Apr. 2012.
[166] M. N. Marwali and A. Keyhani, “Control of distributed generation systems – Part I: Voltages and currents control,” *IEEE Trans. Power Electron.*, vol. 19, pp. 1541–1550, Nov. 2004.
[167] M. N. Marwali, J. W. Jung, and A. Keyhani, “Stability analysis of load sharing control for distributed generation systems,” *IEEE Trans. Energy Convers.*, vol. 22, pp. 737–745, Sept. 2004.
[168] S. D. J. McArthur, E. M. Davidson, V. M. Catterson, A. L. Dimeas, N. D. Hatziargyriou, F. Ponci, and T. Funabashi, “Multi-agent systems for power engineering applications – part I: Concepts, approaches, and technical challenges,” *IEEE Trans. Power Syst.,* vol. 22, pp. 1743–1752, Nov. 2007.
[169] A. Bidram, A. Davoudi, and F. L. Lewis, “A multi-objective distributed control framework for islanded microgrids,” *IEEE Trans. Ind. Informatics*, vol. 10, no. 3, pp. 1785–1798, Aug. 2014.
[170] A. Bidram, A. Davoudi, F. L. Lewis, and Z. Qu, “Secondary control of microgrids based on distributed cooperative control of multi-agent systems,” *IET Generation, Transmission Dist.*, vol. 7, pp. 822–831, Aug. 2013.
[171] V. Nasirian, A. Davoudi, and F. L. Lewis, “Distributed adaptive droop control for DC microgrids,” in *Proc. 29th IEEE Appl. Power Electron. Conf. Expo. (APEC)*, 2014, pp. 1147–1152.
[172] V. Nasirian, S. Moayedi, A. Davoudi, and F. L. Lewis, “Distributed cooperative control of DC microgrids,” *IEEE Trans. Power Electron.*, vol. 30, pp. 2288–2303, Apr. 2015.
[173] V. Nasirian, A. Davoudi, F. L. Lewis, and J. M. Guerrero, “Distributed adaptive droop control for DC distribution systems,” *IEEE Trans. Energy Convers.*, vol. 29, pp. 944–956, Dec. 2014.

[174] S. Moayedi, V. Nasirian, F. L. Lewis, and A. Davoudi, “Team-oriented load sharing in parallel DC-DC converters,” *IEEE Trans. Ind. Appl.*, vol. 51, no. 1, pp. 479–490, Jan./Feb. 2015.
[175] B. A. Robbins, C. N. Hadjicostis, and A. D. Dominguez-Garcia, “A two-stage distributed architecture for voltage control in power distribution systems,” *IEEE Trans. Power Syst.*, vol. 28, pp. 1470–1482, May 2013.
[176] A. D. Dominguez-Garcia, C. N. Hadjicostis, and N. F. Vaidya, “Resilient networked control of distributed energy resources,” *IEEE J. Sel. Areas Commun.*, vol. 30, pp. 113–1148, Jul. 2012.
[177] S. T. Cady and A. D. Dominguez-Garcia, “Distributed generation control of small-footprint power systems,” in *Proc. North American Power Symp.*, 2012, pp. 1–6.
[178] F. Dorfler,J. W. Simpson-Porco, and F. Bullo, “Breaking the hierarchy: Distributed control and economic optimality in microgrids,” 2014, Available on arXiv:1401.1767v1.
[179] H. Bouattour, J. W. Simpson-Porco, F. Dorfler, and F. Bullo, “Further results on distribute secondary control in microgrids,” *IEEE Conf. on Decision and Control*, 2013, pp.1514–1519.
[180] J. W. Simpson-Porco, F. Dorfler, F. Bullo, Q. Shafiee, and J. M. Guerrero, “Stability, power sharing, and distributed secondary control in droop-controlled microgrids,” *IEEE Smart Grid Commun. Symp.*, 2013, pp. 672–677.
[181] J. W. Simpson-Porco, F. Dorfler, and F. Bullo, “Synchronization and power sharing for droop-controlled inverters in islanded microgrids,” *Automatica*, vol. 49, pp. 2603–2611, Jun. 2013.
[182] R. Olfati-saber, J. A. Fax, and R. M. Murray, “Consensus and cooperation in networked multi-agent systems,” *Proc. IEEE*, vol. 95, no. 1, pp. 215–233, Jan. 2007.
[183] R. Olfati-Saber and R. M. Murray, “Consensus problems in networks of agents with switching topology and time-delays,” *IEEE Trans. Automat. Control*, vol. 49, no. 9, pp. 1520–1533, Sept. 2004.
[184] R. W. Erickson and D. Maksimovic, *Fundamental of Power Electronics*, 2nd Ed. Norwell, MA: Kluwer, 2001.
[185] D. P. Spanos, R. Olfati-Saber, and R. M. Murray, “Dynamic consensus for mobile networks,” in *Proc. 16th Int’l. Fed. Automat. Control (IFAC)*, 2005, pp. 1–6.
[186] L. Chen, C. Hu, Q. Zhang, K. Zhang, and I. Batarseh, “Modeling and triple-loop control of ZVS grid-connected DC/AC converters for three-phase balanced micro-inverter application,” *IEEE Trans. Power Electron*, vol. 30, No. 4, pp. 2010–2023, Apr. 2015.
[187] Y. Sozer and D. A. Torrey, “Modeling and control of utility interactive inverters,” *IEEE Trans. Power Electron.*, vol. 24, no. 11, pp. 2475–2483, Nov. 2009.
[188] N. Pogaku, M. Prodanovic, and T. C. Green, “Modeling, analysis and testing of autonomous operation of an inverter-based microgrid,” *IEEE Trans. Power Electron.*, vol. 22, no. 2, pp. 613–625, Mar. 2007.
[189] X. Guo, Z. Lu, B. Wang, X. Sun, L. Wang, and J. M. Guerrero, “Dynamic phasors-based modeling and stability analysis of droop-controlled inverters for microgrid applications,” *IEEE Trans. Smart Grid*, vol. 5, no. 6, pp. 2980–2987, Nov. 2014.
[190] H. Zhang, F. L. Lewis, and Z. Qu, “Lyapunov, adaptive, and optimal design techniques for cooperative systems on directed communication graphs,” *IEEE Trans. Ind. Electron.*, vol. 59, no. 7, pp. 3026–3041, Jul. 2012.

[191] F. Xiao and L. Wang, “Asynchronous consensus in continuous-time multi-agent systems with switching topology and time-varying delays,” *IEEE Trans. Automat. Control*, vol. 53, no. 8, pp. 1804–1816, Sept. 2008.
[192] S. Ci, J. Qian, D. Wu, and A. Keyhani, “Impact of wireless communication delay on load sharing among distributed generation systems through smart microgrids,” *IEEE Wireless Communications*, vol. 19, no. 3, pp. 24–29, Jun. 2012.
[193] S. Liu, X. Wang, and P. X. Liu, “Impact of communication delays on secondary frequency control in an islanded microgrid,” *IEEE Trans. Ind. Electron.*, to be published, DOI: 10.1109/TIE.2014.2367456.
[194] H. Behjati, A. Davoudi, and F. L. Lewis, “Modular DC-DC converters on graphs: cooperative control,” *IEEE Trans. Power Electron.*, vol. 29, no. 12, pp. 6725–6741, Dec. 2014.
[195] H. Kakigano, Y. Miura, and T. Ise, “Low-voltage bipolar-type DC microgrid for super high quality distribution,” *IEEE Trans. Power Electron.*, vol. 25, no. 12, pp. 3066–3075, Dec. 2010.
[196] A. Kwasinski, “Quantitative evaluation of DC microgrids availability: effects of system architecture and converter topology design choices,” *IEEE Trans. Power Electron.*, vol. 26, no. 3, pp. 835–851, Mar. 2011.
[197] Y. Gu, X. Xiang, W. Li, and X. He, “Mode-adaptive decentralized control for renewable DC microgrid with enhanced reliability and flexibility,” *IEEE Trans. Power Electron.*, vol. 29, pp. 5072–5080, Sept. 2014.
[198] N. Bottrell, M. Prodanovic, and T. C. Green, “Dynamic stability of a microgrid with an active load,” *IEEE Trans. Power Electron.*, vol. 28, no. 11, pp. 5107–5119, Nov. 2013.
[199] A. Khorsandi, M. Ashourloo, and H. Mokhtari, “A decentralized control method for a low-voltage DC microgrid,” *IEEE Trans. Energy Convers.*, vol. 29, pp. 792–801, Dec. 2014.
[200] M. B. Shadman, R. S. Balog, and H. Abu-Rub, “Model predictive control of PV sources in a smart DC distribution system: Maximum power point tracking and droop control,” *IEEE Trans. Energy Convers.*, vol. 29, pp. 913–921, Dec. 2014.
[201] V. Nasirian, A. Davoudi, F. L. Lewis, and J. M. Guerrero, “Distributed adaptive droop control for DC distribution systems,” *IEEE Trans. Energy Convers.*, vol. 29, pp. 944–956, Dec. 2014.
[202] S. Sanchez and M. Molinas, “Degree of influence of system state transition on the stability of a DC microgrid,” *IEEE Trans. Smart Grid*, vol. 30, pp. 2535–2542, Sept. 2014.
[203] M. Farhadi and O. Mohammed, “Adaptive energy management in redundant hybrid DC microgrid for pulse load mitigation,” *IEEE Trans. Smart Grid*, vol. 6, pp. 54–62, Jan. 2015.
[204] M. Patterson, N. F. Macia, and A. M. Kannan, “Hybrid microgrid model based on solar photovoltaic battery fuel cell system for intermittent load applications,” *IEEE Trans. Energy Convers.*, vol. 30, pp. 359–366, Mar. 2015.
[205] F. A. Inthamoussou, J. P. Queralt, and F. D. Bianchi, “Control of a supercapacitor energy storage system for microgrid applications,” *IEEE Trans. Energy Convers.*, vol. 28, pp. 690–697, Sept. 2013.
[206] G. Xu, L. Xu, D. J. Morrow, and D. Chen, “Coordinated DC voltage control of wind turbine with embedded energy storage system,” *IEEE Trans. Energy Convers.*, vol. 27, pp. 1036–1045, Dec. 2012.

[207] N. R. Tummuru, M. K. Mishra, and S. Srinivas, “Dynamic energy management of hybrid energy storage system with high-gain PV converter,” *IEEE Trans. Energy Convers.*, vol. 30, pp. 150–160, Mar. 2015.
[208] S. Sanchez and M. Molinas, “Large signal stability analysis at the common coupling point of a DC microgrid: A grid impedance estimation approach based on a recursive method,” *IEEE Trans. Energy Convers.*, vol. 30, pp. 122–131, Mar. 2015.
[209] R. Ahmadi and M. Ferdowsi, “Improving the performance of a line regulating converter in a converter-dominated DC microgrid system,” *IEEE Trans. Smart Grid*, vol. 5, pp. 2553–2563, Sept. 2014.
[210] M. Kim and A. Kwasinski, “Decentralized hierarchical control of active power distribution nodes,” *IEEE Trans. Energy Convers.*, vol. 29, pp. 934–943, Dec. 2014.
[211] S. Kazemlou and S. Mehraeen, “Novel decentralized control of power systems with penetration of renewable energy sources in small-scale power systems,” *IEEE Trans. Energy Convers.*, vol. 29, pp. 851–861, Dec. 2014.
[212] A. Kwasinski and C. N. Onwuchekwa, “Dynamic behavior and stabilization of DC microgrids with instantaneous constant-power loads,” *IEEE Trans. Power Electron.*, vol. 26, pp. 822–834, Mar. 2011.
[213] P. Magne, B. Nahid-Mobarakeh, and S. Pierfederici, “General active global stabilization of multi-loads DC power networks,” *IEEE Trans. Power Electron.*, vol. 27, pp. 1788–1798, Apr. 2012.
[214] P. Magne, B. Nahid-Mobarakeh, and S. Pierfederici, “Active stabilization of DC microgrids without remote sensors for more electric aircraft,” *IEEE Trans. Ind. Appl.*, vol. 49, pp. 2352–2360, Sept./Oct. 2013.
[215] D. Logue and P. T. Krein, “The power buffer concept for utility load decoupling,” in *Proc. IEEE Power Electron. Specialist Conf.*, 2000, pp. 973–978.
[216] D. L. Logue and P. T. Krein, “Preventing instability in DC distribution systems by using power buffering,” in *Proc. Power Electron. Specialist Conf.*, 2001, pp. 33–37.
[217] W. W. Weaver and P. T. Krein, “Mitigation of power system collapse through active dynamic buffers,” *IEEE Power Electronics Specialist Conference,* 2004, pp. 1080-1084.
[218] Z. Shan, P. T. Krein, C. K. Tse, and S. C. Tan, “Pre-energize compact auxiliary circuit to buffer loads from fast transients with the goal of managing load-informed power,” in *Proc. IEEE Workshop on Control and Modeling for Power Electronics*, 2013, pp. 1–4.
[219] R. S. Balog, W. W. Weaver, and P. T. Krein, “The load as an energy asset in s distributed DC smartgrid architecture,” *IEEE Trans. Smart Grid*, vol. 3, pp. 253–260, Mar. 2012.
[220] W. W. Weaver and P. T. Krein, “Optimal geometric control of power buffers,” *IEEE Trans. Power Electron.*, vol. 24, pp. 1248–1258, May 2009.
[221] W. W. Weaver and P. T. Krein, “Game-theoretic control of small-scale power systems,” *IEEE Trans. Power Del.*, vol. 24, pp. 1560–1567, Jul. 2009.
[222] W. W. Weaver, “Dynamic energy resource control of power electronics in local area power networks,” *IEEE Trans. Power Electron.*, vol. 26, pp. 852–859, Mar. 2011.
[223] N. C. Ekneligoda and W. W. Weaver, “Game-theoretic cold-start transient optimization in DC microgrids,” *IEEE Trans. Ind. Electron.*, vol. 61, pp. 6681–6690, Dec. 2014.

[224] N. C. Ekneligoda and W. W. Weaver, “Game-theoretic communication structures in microgrids,” *IEEE Trans. Power Del.,* vol. 27, pp. 2334–2341, Oct. 2012.
[225] B. Banerjee and W. W. Weaver, “Generalized geometric control manifolds of power converters in a DC microgrid,” *IEEE Trans. Energy Convers.*, vol. 29, pp. 904–912, Dec. 2014.
[226] J. K. Vlachogiannis and K. Y. Lee, “Economic load dispatch—A comparative study on heuristic optimization techniques with an improved coordinated aggregation-based PSO,” *IEEE Trans. Power Syst.*, vol. 24, no. 2, pp. 991–1001, May 2009.
[227] F. Yao, Z. Y. Dong, K. Meng, Z. Xu, H. H.-C. Iu, and K. P. Wong, “Quantum-inspired particle swarm optimization for power system operations considering wind power uncertainty and carbon tax in Australia,” *IEEE Trans. Ind. Inf.*, vol. 8, no. 4, pp. 880–888, Nov. 2012.
[228] J. Zhao, F. Wen, Z. Y. Dong, Y. Xue, and K. P. Wong, “Optimal dispatch of electric vehicles and wind power using enhanced particle swarm optimization,” *IEEE Trans. Ind. Inf.*, vol. 8, no. 4, pp. 889–899, Nov. 2012.
[229] P. Siano, C. Cecati, H. Yu, and J. Kolbusz, “Real time operation of smart grids via FCN networks and optimal power flow,” *IEEE Trans. Ind. Inf.*, vol. 8, no. 4, pp. 944–952, Nov. 2012.
[230] C.-L. Chiang, “Improved genetic algorithm for power economic dispatch of units with valve-point effects and multiple fuels,” *IEEE Trans. Power Syst.*, vol. 20, no. 4, pp. 1690–1699, Nov. 2005.
[231] J. Zhou “Solving economic dispatch problem with piecewise quadratic cost functions using Lagrange multiplier theory,” in *Proc. 3rd ICCTD*, Chengdu, China, 2011, pp. 25–27.
[232] T. Tashiro, K. Tamura, and K. Yasuda, “Modeling and optimal operation of distributed energy systems via dynamic programming,” in *Proc. IEEE Int. Conf. SMC*, Anchorage, AK, USA, Oct. 2011, pp. 808–813.
[233] N. Sinha, R. Chakrabarti, and P. K. Chattopadhyay, “Evolutionary programming techniques for economic load dispatch,” *IEEE Trans. Evol. Comput.*, vol. 7, no. 1, pp. 83–94, Feb. 2003.
[234] V. Loia and A. Vaccaro, “Decentralized economic dispatch in smart grids by self-organizing dynamic agents,” *IEEE Trans. Syst. Man Cybernetics*, vol. 44, no. 4, pp. 397–408, Apr. 2014.
[235] G. Binetti, A. Davoudi, D. Naso, B. Turchiano, and F. L. Lewis, “A distributed auction-based algorithm for the non-convex economic dispatch problem,” *IEEE Trans. Ind. Inf.*, vol. 10, no. 2, pp. 1124–1132, May 2014.
[236] G. Binetti, A. Davoudi, F. L. Lewis, D. Naso, and B. Turchiano, “Distributed consensus-based economic dispatch with transmission losses,” *IEEE Trans. Power Syst.*, vol. 29, no. 4, pp. 1711–1720, Jul. 2014.
[237] E. Kellerer and F. Steinke, “Scalable economic dispatch for smart distribution networks”, *IEEE Trans. Power Syst.*, to be published, DOI: 10.1109/TPWRS.2014.2358375.
[238] L. Du, S. Grijalva, and R. G. Harley, “Game-theoretic formulation of power dispatch with guaranteed convergence and prioritized best response,” *IEEE Trans. Sust. Energy*, vol. 6, no. 1, pp. 51–59, Jan. 2015.
[239] V. Nasirian, S. Moayedi, A. Davoudi, and F. L. Lewis, “Distributed cooperative control for dc microgrids,” *IEEE Trans. Power Electron.*, vol. 30, no. 4, pp. 2288–2303, Apr. 2015.

[240] V. Nasirian, A. Davoudi, F. L. Lewis, and J. M. Guerrero, “Distributed adaptive droop control for dc distribution systems,” *IEEE Trans. Energy Convers.*, vol. 29, no. 4, pp. 944–956, Dec. 2014.
[241] S. Moayedi, V. Nasirian, F. L. Lewis, and A. Davoudi, “Team-oriented load sharing in parallel dc-dc converters,” *IEEE Trans. Ind. Appl.*, vol. 51, no. 1, pp. 479–490, Jan./Feb. 2015.
[242] S. Moayedi and A. Davoudi, “Distributed cooperative load sharing in parallel DC-DC converters” in *Proc. 29th IEEE Appl. Power Electron. Conf. Expo.*, 2014, pp. 2907–2912.
[243] Z. Qu, *Cooperative control of dynamical systems: Applications to autonomous vehicles*. New York: Springer-Verlag, 2009.

Biographical Information

Vahidreza Nasirian received the B.S. and M.S. degrees in electrical engineering from Sharif University of Technology, Tehran, Iran, in 2007 and 2010, respectively. He achieved the Ph.D. degree from the University of Texas at Arlington, Arlington, TX, USA in August 2015.

His research interests include the modeling and control of power electronics, control development for microgrids, transportation electrification, renewable/sustainable energy systems, and control of multi-agent dynamic systems.

He was the recipient of the gold medal at the 20th National Mathematics Olympiad in 2002 and the bronze medal at the 2nd Silk Road Mathematics Competition in 2003. He was also the recipient of the Iranian National Elites Foundation Fellowship for 2008–2010, the Carrizo Oil and Gas Inc Graduate Research Fellowship for 2011–2013, IEEE APEC Student Travel Support 2015, and the Office of Graduate Studies Dissertation Fellowship, UT Arlignton, Summer 2015.